On Phase Contrast Imaging of the Inner Retina

Eric Logean

Supervisor:
Prof. Chris Dainty

National University *of* Ireland, Galway
Ollscoil na hÉireann, Gaillimh

A thesis submitted in partial fulfilment of the requirements
for the degree of Doctor of Philosophy,

School of Physics, College of Science,
National University of Ireland, Galway

September 2009

Contents

海と七湖と光湖と理依子へ

To

Kai, Nanako, Mitsuko, and Rieko

Abstract

Adaptive optics correction of the ocular aberrations enables *in vivo* high resolution imaging of the retina in humans. The cone photoreceptor mosaic is routinely imaged. In front of the photoreceptors, the inner retina is a thick layer of transparent cells waiting to be imaged. The resolution is adequate, but the contrast needs to be enhanced. This thesis describes a series of experiments aimed at advancing phase imaging of the retina.

After a description of the retina and a review of retinal imaging, the possibilities of using a phase sensitive techniques is discussed. The current imaging techniques use the light directly reflected by the inner retina. In this work, the light back-scattered from the outer retina (photoreceptors and retinal pigment epithelium cells) and transmitted through the inner retina is used. By illuminating the outer retina with a point-like illumination, all the phase imaging techniques based on spatial filtering can be used to image the inner retina.

This illumination geometry is used with the phase contrast method of Zernike to obtain images of glass objects. Phase contrast images are obtained using light reflected from a diffuser in a geometry similar to the eye. Some contrast enhancement is obtained when imaging a rat retina, *ex vivo*.

A fundus camera with adaptive optics is built to image the human retina. The light distribution in the outer retina for a focal illumination is studied in detail. It is found that this distribution follows a Lorentzian function with a width (half width at half maximum) at least 3.7 times the expected width for a diffraction limited eye. This light distribution is not suitable for phase imaging using spatial filtering.

Preface

In vivo images of the human retina play a central role in the study of the retinal diseases and in their diagnosis. These images suffer from two main limitations. The first is a low resolution due to the ocular aberrations and the limited aperture of the eye. The second is a lack of contrast due to the transparent nature of a large part of the retina.

With the development of the adaptive optics technique for the eye, the resolution has been greatly increased. After correction of the ocular aberrations, it is possible to image the cone photoreceptor mosaic [1]. The resolution in these images is sufficient to resolve the majority of retinal cells. For the transparent cells, however, the second limitation remains. In this work, I study the possibility of using the phase of light as a mechanism to bring some contrast from the transparent cells of the retina. I am not the first to study this possibility. In 1997, Thall patented the use of the phase contrast method of Zernike to image the retina [2]. The illumination geometry he describes is not suitable for this task. I propose another illumination geometry [3].

Out of all the transparent cells of the retina, the greatest interest might be in imaging the ganglion cells. These cells are the ones affected in glaucoma [4], the second leading cause of blindness in the world [5]. At present, their loss is observed indirectly through the measure of visual function, the observation of the shape of the optic disc, and the thickness of the nerve fibre layer. Images of the ganglion cells could provide a direct mean to monitor the progression of this disease and its reaction to different medications.

In this thesis, I refer as much as I can to the original papers. In addition to these references, Actchison and Smith published an excellent compilation of information on the eye optics [6] and Porter *et al.*

published the first book on adaptive optics for vision science [7].

It is through the support and help from many people that this work was possible. I am very grateful to Professor Chris Dainty, my supervisor, for his excellent mentoring and for his financial support, which comes from two Science Foundation Ireland grants 01/PI.2/B039C and 07/IN.1/I906. I would like to thank Dr. Eugénie Dalimier for her help with the adaptive optics system and for her work during the experiments on volunteers, Dr. Anna Burwall and Dr. Alexander Goncharov for illuminating discussions, the volunteers for their time and patience, Dr. Dirk De Brouwere for handling the corneas, and the members and visitors of the Applied Optics Groups for their different contributions. I am indebted to Professor Peter Dockery for the carefully prepared retinal samples, to Professor Jari Turunen for the custom-made phase plates, to Silios Technologies, France, for the phase objects, to Dr. Sebastian Favre for measuring the profile of the phase object and with Fabien Bernard for the preparation of various masks. The image of the fundus of my right eye, shown in Fig. 1.4, was taken and developed by the personnel of the ophthalmic clinic of Créteil in Paris in 2001. To conclude, I would like to thank the members of what was the Optics Group of the Research Institute in Ophthalmology in Sion, Switzerland, particularly Professor Charles Riva, Martial Geiser, and Dr. Stéphane Chamot. The period I spent in your company was the best preparation I could have dreamt of before undertaking this work.

Eric Logean

Symbols and abbreviations

Roman symbols

A	amplitude
a	pupil radius
a_{nm}	expansion coefficient
b	radius of the phase-shifting area of the phase plate
C	constant
c	velocity of light in vacuum, $c = 3{\times}10^8$ m/s
d	physical distance
f	focal length, or a function
H	pupil function
h	point-spread function
I	intensity
i	complex number $\mathrm{i} = \sqrt{-1}$
J_n	Bessel function of the first kind, order n
j	polynomial ordering number
k	wave number, $2\pi/\lambda$
k_0	wave number in vacuum, k/n
$\mathcal{L}$	fractional power (laser safety)
l	optical path length
l_c	coherence length
M	transverse magnification
m	azimuthal frequency of the circle polynomials and modulation of a phase object, rad
n	refractive index and polynomial radial order

O	object
O'	image
P	point in space
Q	point in space
q	grating diffraction order
R_n^m	radial polynomials
r	radial coordinate
$r_{\min}$	radius of the first zero of the Airy pattern
$\mathbf{r}$	vector coordinate of a point in space (x, y, z)
T	time period
$\mathcal{T}$	transmittance
t	time
Δt	characteristic time
U	complex amplitude of a wave function
u	image spatial frequency, $1/x$, and normalised axial coordinate in optical unit, o.u.
V	wave function
$\mathcal{V}$	interference fringe visibility or contrast
v	velocity of light in a homogeneous medium, $v = c/n$, image spatial frequency, $1/y$, and normalised transverse coordinate in optical unit, o.u.
W	wavefront aberration
w	image spatial frequency (radial), $1/r$, and half width at half maximum of a point-spread function
x	Cartesian coordinate in the object/image plane
y	Cartesian coordinate in the object/image plane
Z_n^m	circle polynomials of Zernike
z	Cartesian coordinate along the optical axis

Greek symbols

α	angular substance (laser safety), rad
$\alpha_{\min}$	minimum angular substance (laser safety), rad
Γ	mutual coherence function
γ	complex degree of coherence
δ	unit area impulse
δ_{ij}	Kronecker delta
η	Cartesian coordinate in the exit pupil and

	diffraction efficiency
λ	wavelength of light
μ_s	scattering coefficient, mm^{-1}
ν	temporal frequency
$\Delta\nu$	spectral width
θ	coordinate of the azimuthal angle
Φ	maximum permissible power (laser safety)
ϕ	phase
τ	time difference
τ_c	coherence time
ρ	radial coordinate in the exit pupil
σ	source
ξ	Cartesian coordinate in the exit pupil
ω	angular frequency, $\omega = 2\pi\nu$

Other symbols

$\tilde{\square}$	Fourier transform of $\square$
$\bar{\square}$	mean value of $\square$

Abbreviations

AO	adaptive optics
CCD	charge coupled device
DM	deformable mirror
FM	frequency modulation
HWHM	half width at half maximum
ILM	inner limiting membrane
MPE	maximum permissible exposure
MTF	modulation transfer function
NUIG	National University of Ireland, Galway
OCT	optical coherence tomography
OTF	optical transfer function
PP	phase plate
PSF	point-spread function
RMS	root mean square
RPE	retinal pigment epithelium
SLO	scanning laser ophthalmoscope

1

Imaging the retina

This chapter is about *imaging* and the *retina*. On imaging, the two important notions of resolution and contrast are introduced. Both resolution and contrast are needed for imaging. The object to be imaged is the retina. A description of its anatomy is followed by a review of its known optical properties. With this background information, the development of *retinal imaging* is reviewed starting from its first accidental step to its current rapid developments. The importance of resolution and contrast is highlighted.

1.1 Resolution and contrast

The complete process of image formation can be separated in three steps:

1. The generation of a light wave emanating from the object using an illumination system—except for self-luminous objects;

2. The conjugation of the object plane with the image plane using an optical system;

3. The detection of the light wave.

The image is the detected light intensity, which reveals spatial variations, i.e., features, related to the object. These features may be discussed in term of their intensity and their dimension.

The contrast is a measure of the difference in intensity between two image points, e.g., one on a feature and the other on the background. Here, the contrast is defined according to Michelson criterion for the

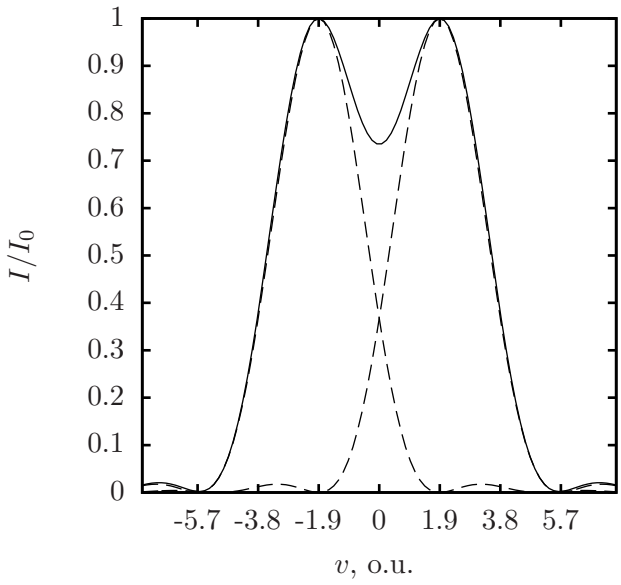

Fig. 1.1. Normalised intensity profile I/I_0 passing through the image of two point sources separated by the resolution criterion of Rayleigh for a circular aperture (3.833 o.u.). I_0 is the intensity at the centre of the diffraction pattern of a single point source and v is the normalised distance in the image plane.

visibility of interference fringes [8].

$$\mathcal{V} = \left| \frac{I_2 - I_1}{I_2 + I_1} \right|, \tag{1.1}$$

where I_1 and I_2 are the measured intensities.

The resolution limit of an imaging process is the minimum separation needed to detect the presence of two objects. This limit can be measured, but in general it is not. Instead, the resolution limit is calculated from a model of the optical system. As stressed by Ronchi [9], the calculated resolution limit is different from the measured resolution limit.

Lord Rayleigh was the first to introduce a criterion of resolution [8, 10]. He proposed that two point sources of equal brightness viewed through an aberration-free optical system should be considered resolved if the maximum of the diffraction pattern for one source falls on the first minimum of the diffraction pattern for the second source (see Fig. 1.1). Rayleigh assumed that the light from both sources does not interfere

and that the image is visually observed. The plot in Fig 1.1 shows the normalised intensity profile I/I_0 in the image of two point sources of equal intensity separated by Rayleigh's criterion for a circular aperture, 3.833 optical unit (o.u.)* I_0 is the intensity at the centre of the diffraction pattern of a point source. The central dip is $0.735\,I_0$. The contrast between a maximum and the central dip is 15 %. For a square aperture, the dip is $0.811\,I_0$ and the contrast is 10.5 %.

By its simplicity, the criterion of Rayleigh became the reference by which imaging processes—and other resolution criteria—are compared. In practice, it is an ideal rarely equalled, due to unfavourable viewing conditions or to the presence of aberrations [9]. On another hand, when Rayleigh's assumptions are not met, the measured resolution might surpasses this criterion. Today, in most imaging processes, the eye of the observer has been replaced by an electronic detector. The resolution limit has been studied for different super-resolution techniques and it was found to be limited by the noise level of the detected signal [11].

The minimum contrast necessary to detect an image features also depends on the noise level. Through modelling, it is possible to compute the expected contrast and determine the signal to noise ratio. Both resolution and contrast are needed for the visibility of fine details in an image and both are limited by the noise level of the detected intensity.

1.2 The retina

In this work, the retina is the object of interest. It is a tissue that covers the inner side of the eyeball. The optics of the eye forms an image on the retina, whose function is to detect, process, and transmit the visual information to higher visual centres of the brain. The retina is in contact with the vitreous humour and with the choroid. A cross-section of the retina is shown in Fig. 1.2. The width of this image corresponds to a visual angle of 35°. The arrows show the location of the optic nerve (left) and of a pit in the retina (right). This pit is called *fovea centralis* or fovea and it is the centre of detailed vision. This image was obtained using optical coherence tomography (OCT), a technique discussed in Section 1.6.

*optical unit, $v = 2\pi\frac{ax}{\lambda z}$, with a the radius of the aperture, x the physical distance in the image plane, λ the wavelength, and z the propagation distance [8]

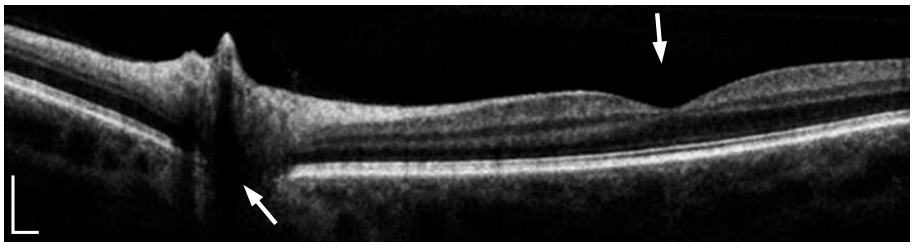

Fig. 1.2. Cross-section of the retina obtained by optical coherence tomography. The top black area is the vitreous humour. The retina extends from the vitreous humour to the retinal pigment epithelium layer, the brightest layer. The arrow on the left indicates the position of the optic nerve. The arrow on the right points at the *foveola* located at the centre of the foveal pit. The scale bars represent a length of 300 μm. Reprinted from Považay *et al.* [12].

Anatomy

A cross-section of a stained human retina imaged by light microscopy is shown in Fig. 1.3. The retina is limited internally by the inner limiting membrane (ILM) and externally by the Bruch's membrane. It is arranged in successive layers of cell bodies—also called somas or *perikarya*—and of cell processes (dendrites and axons). The legend of Fig. 1.3 names the different layers. The cellular composition of the retinal layers may be found in the literature [13–17]. Shortly, the somas of the ganglion cells are in the ganglion cell layer, the somas of the photoreceptors are in the outer nuclear layer, and the somas of the other types of neural cells, i.e., the bipolar cells, horizontal cells, amacrine cells, are in the inner nuclear layer. The retina has different types of glial cells. The somas of these cells are mostly located in the ganglion cell layer and the inner nuclear layer [13]. The Müller cells are glial cells omnipresent in the retina. Their feet form the inner limiting membrane (ILM) and their processes span the entire section of the retina. Behind the photoreceptor layer, there is a single layer of cells called retinal pigment epithelium (RPE).

At the centre of the fovea, the *foveola*, the thickness of the retina is about 130 μm [13]. From the *foveola*, the thickness increases with distance and reaches 400 μm at about 1.25 mm [17], a distance corresponding to an eccentricity of 4°. The thickness of the retina shown in Fig. 1.3 is about 400 μm. In OCT images, the thickness of the retina at the *foveola* appears to be thicker than 130 μm (see Fig. 1.2). The

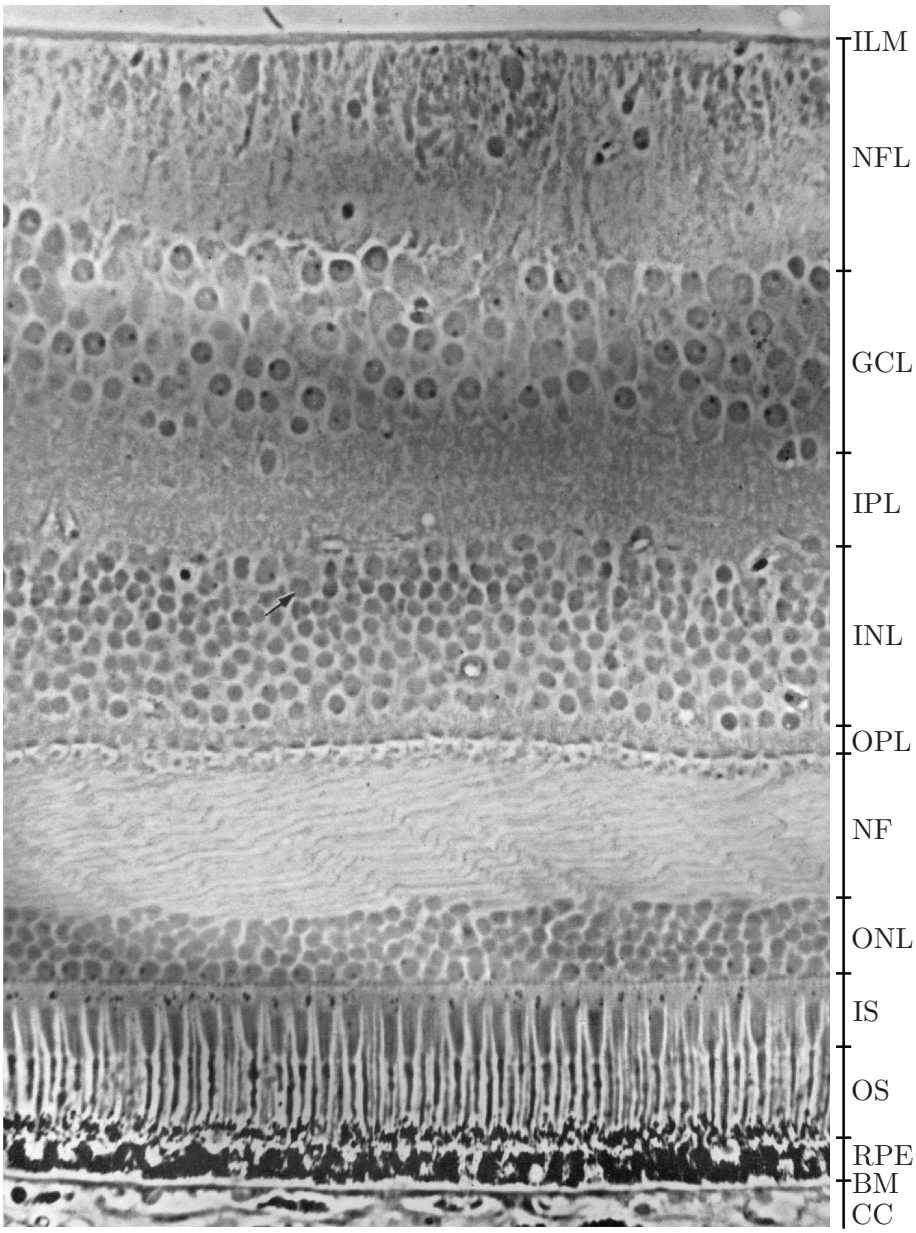

Fig. 1.3. Cross-section of a stained human retina imaged by light microscopy; ILM, inner limiting membrane; NFL, nerve fibre layer; GCL, ganglion cell layer; IPL, inner plexiform layer; INL, inner nuclear layer; OPL, outer plexiform layer; NF, fibre layer; ONL, outer nuclear layer; IS, photoreceptor inner segment; OS, photoreceptor outer segment; RPE, retinal pigment epithelium; BM, Bruch's membrane; CC, chorio-capillaries. From the outer edge of the RPE to the ILM, the retina is 400 μm thick. Reproduced from [17].

foveola is the area of maximum visual acuity. There, the ocular aberrations are minimum [18], the density of the cone photoreceptors is maximum [19], and the spatial summation of the neural process is minimum, i.e., the number of bipolar and ganglion cells per photoreceptor is the highest [15, 20]. The shape of the retina, the foveal pit and foveal rim, is due to the lateral displacement, away from the *foveola*, of the cells of the inner nuclear layer and the ganglion cells. At larger eccentricities, the cell density in the retina decreases, the somas of the ganglion cells form a single row, the inner nuclear layer is thinner than in Fig. 1.3, and the photoreceptor nerve fibre is absent (Henle's fibres).

Optical properties

It is said that the retina is transparent to light, turning hazy after death [13]. Of course this is a qualitative description of the visual appearance of the retina. To be more precise, there is a low amount of light absorption and of light scatter in the retinal tissue between the ILM and the outer nuclear layer. From now on, I will call this part of the retina the inner retina. In contrast, light is strongly absorbed and scattered by the outer retina, the photoreceptor segments and the retinal pigment epithelium (RPE) cells.

Absorption. Absorption is due to the presence of pigments. In the inner retina, there are at least three known pigments.

- The hæmoglobin contained in the red blood cells which are confined to the retinal vascular network.
- The macular pigments, which are found everywhere in the retina, but their concentration is high only within a radius of a few degrees around the *foveola*. In that area, a yellow spot called *macula lutea* or macula is visible [13, 16].
- The melanopsin, a pigment found in a class of ganglion cell responsible for the synchronisation of the circadian rhythm [21]. These ganglion cells are sparsely distributed in the ganglion cell layer, and therefore, this pigment plays no significant role in retinal imaging.

In contrast to the inner retina, the outer retina is very pigmented. Rhodopsin and photopsin, the visual pigments, are located in the photoreceptor outer segments. The cells of the RPE contain melanin and

lipofuscin pigments. The retina ends here, but part of the light is transmitted through the RPE and reaches the choroid, which contains hæmoglobin and a variable amount of melanin [22, 23].

Scattering. Scattering is due to rapid changes in refractive index. In cells, the refractive index mainly depends on the concentration of proteins ($n \approx 1.50$) [24, 25]. These proteins are found in high concentration in the different membranes of the cell and of its constituents. In the nuclear layers, there are only a few membranes per unit of volume and the scattering is low. In the layers of cell processes, the proportion of membrane by unit of volume is large and scattering is more important.

Vos and Bouman [26] determined subjectively the proportion of retinal scatter to the total *entoptic* scatter—the total amount of scatter observed by the subject within the subject's own eye. These authors found that retinal scatter accounts for 12 to 40 % of the total *entoptic* scatter. Zeimer *et al.* [27] measured the thickness of the retina from the lateral spacing between the light reflected by the inner limiting membrane (ILM) and by the photoreceptor layer measured in retinal images obtained with a large separation between the input (illumination) and output (observation) pupils. Between these two reflections, the retinal back scattering is visible. The retinal back scatter is measured by the optical coherence tomography (OCT) technique [28].

Compared to the inner retina, the outer retina, the choroid, and the sclera are more efficient scatterers. Hammer *et al.* [29] used the double-integrating-sphere technique to obtain the optical properties of bovine tissues. At a wavelength of 550 nm, the scattering coefficient μ_s—which is the inverse of the mean optical path length between two scattering events in an homogeneous tissue without absorption—is $30\,\mathrm{mm}^{-1}$ for the retina; $120\,\mathrm{mm}^{-1}$ for the RPE; $60\,\mathrm{mm}^{-1}$ for the choroid, and; $80\,\mathrm{mm}^{-1}$ for the sclera.

Guiding. Some structures of the retina act as light guide. The photoreceptor segments exhibit waveguide modes transmission [30]. These segments behave like optical fibres, which radiating pattern can explain both the psychophysical Stiles–Crawford effect [31] and the optical Stiles–Crawford effect (see for example [32, 33]). Recently, Franze *et al.* have shown that Müller cells guide the light [34]. Whether this property has a function for vision remains to be explored.

1.3 Observing the *fundus oculi*

The bottom of the eye, as seen through the pupil, is called the *fundus oculi*, or fundus. In 1704, Méry reported an accidental observation of the fundus of the eye of a living cat [35, 36]. In 1823, Purkyně observed the fundus of the eye of a human subject [37]. His work was apparently not known to Helmholtz, who developed the first instrument to visualise the fundus in 1850.

Helmholtz realised that in order to observe an illuminated region of the fundus, he had to place his eye on the axis defined by the subject's pupil and the light source [38]. By using a beam splitter, he was able to place his eye on that axis without obstructing the illumination light. He used a concave lens close to his eye to obtain a clear image of the fundus of the subject's eye on his retina. The ophthalmoscope was born.

This instrument was further developed to include, following Gullstrand's review [38, Volume 1, Appendix 1],

- an indirect mode of observation achieved using a convex lens that forms an intermediate image, which is observed through a second convex lens (indirect ophthalmoscope),
- a reflex-free illumination obtained by separating the light path of the illumination from the light path of the observation through the optics of the eye, and
- a mean of recording the image obtained using an electric lamp and a sensible photographic plate (fundus camera).

Gullstrand is credited with the invention of the slit lamp microscope [39, 40]. This instrument consists in a slit-shaped illumination and in a long working binocular microscope [41]. It was developed to image the anterior segment of the eye. A positive lens of about 90 dioptres can be held in front of the eye to achieve an optical arrangement similar to the indirect ophthalmoscope, but with a binocular observation [40]. This use of the slit lamp microscope provides a reflex-free stereoscopic view of the fundus.

1.4 The fundal image

The images of the fundus formed by the ophthalmoscope, the fundus camera, and the slit lamp microscope reveals—wavelength dependent—

Fig. 1.4. Red-free image of the fundus of the author's right eye showing part of a circular field of 45°. The dark area at the centre is the macula. The white disc at the right hand side is the optic nerve through which retinal vessels enter and exit the eye (dark lines). In the white circle, the vasculature of the choroid is partially visible. In the white square, the light scatter from the nerve fibre layer is visible (low contrast). Specular reflections from the inner limiting membrane are visible at the centre of retinal vessels, e.g., on the artery pointed by the black arrow.

spatial variations of intensity due to local differences in the absorption and the scattering properties of the tissue. As an example of fundal images that are acquired with these three instruments, I describe the main features visible in the red-free image shown in Fig. 1.4.

The white disc at the right hand side is the optic nerve. It has a low absorption and a strong scattering properties. The dark lines expanding from the optic nerve are called retinal vessels. In fact, the vessels are not visible. Only the column of red blood cells flowing through each vessel is visible because the light is strongly absorbed by the hæmoglobin. The dark spot at the centre is the macula. Compared to the rest of the fundus, the macula appears darker due to the absorption of the short waves by the macular pigments. In the white circle, the choroidal

vasculature is partially visible. In that area, the pigmentation level in the RPE is low. The white lines at the centre of some retinal vessels (black arrow) and the diffuse whitish lines running parallel to the retinal vessels (white square) are the only hints of the presence of the retina. The first are specular reflections of the inner limiting membrane [42] and the second are due to the weak scattering of light by the nerve fibre layer [42].

The appearance of the fundus is changed in most ocular pathologies or conditions affecting the retina. For example, in retinal detachments, the retina is easily observed, and in the occurrence of vessel occlusions, in diabetic retinopathy, in systemic hypertension, in age-related macular degeneration, and in some others pathologies, changes in the retinal vasculature are observed [43]. The image of the fundus is often the most important information available to the clinician. This may explain the large effort made to maximise the information extracted from these images.

The contrast of the different features in the fundal image can be enhanced by spectral filtering [42]. The image in Fig. 1.4 was obtained using a filter that transmits the short waves (blue and green) and blocks the long waves (red). The use of such filter enhances the contrast of the retinal vessels and of the nerve fibre layer. Different contrast mechanism are in use. The fluorescence from dyes delivered into the circulation is imaged in the fluorescein angiography technique [44]. The autofluorescence of the lipofuscin pigment located in the RPE cells has been imaged [45]. The polarisation properties of the fundus is used to visualise the brush pattern related to the Henle's fibres and to enhance the contrast of the nerve fibre layer [46, 47]. Using a coherent light source, a map of the blood perfusion can be obtained from the contrast of the speckle pattern [48].

Other parameters are studied using *several* images of the fundus. In spectroscopy, a set of fundal images is acquired using different wavelength bands. From the measured differences in reflection, the density of the macular pigments [49, 50] and the oxygen saturation in retinal veins [51–53] can be obtained. Recently, resonant Raman scattering has been used to map the density of macular pigments [54]. The time variation of the fundal reflectance is used to image changes in neural activity induced by visual stimulation [55–57].

The scope of these lines of research is very impressive, but none of

them provide a microscopic view of the retinal structures. For such a view, the magnification of the fundus camera must be increased.

1.5 High-resolution imaging of the retina

The use of a high transverse magnification generally does not reveal more details in the fundal image than the details visible in Fig. 1.4. Instead, the small features are blurred by the combined effect of light diffraction and of the ocular aberrations. For a pupil with a diameter smaller than 2 mm, the optical quality of most eyes is limited by diffraction [58]. For large apertures, the effect of aberrations is important and varies between individuals [59].

Using the theory of linear system and assuming shift invariance, the relative transmission of the object's spatial frequencies through an optical system is given by the modulation transfer function (MTF) [60]. A radial section of the MTF of three hypothetical eyes is plotted in Fig. 1.5, for an incoherent light with a centre wavelength of 633 nm.

1. The continuous line is the MTF of a diffraction limited eye with a pupil diameter of 3 mm.

2. The long-dashed line is the MTF of a diffraction limited eye with a pupil diameter of 6 mm.

3. The short-dashed line is the MTF of an aberrated eye with a pupil diameter of 6 mm. This eye has the same MTF than the average of the MTF measured in a population of 200 eyes [61].

The observation pupil of a commercial fundus camera has a diameter of approximately 3 mm. For most subject, the images obtained with these instruments is close to the diffraction limit (first hypothetical eye). To increase the magnification and avoid the so-called empty-magnification, the pupil diameter is increased. For a perfect eye with a diameter of 6 mm (second hypothetical eye), the cut-off frequency is doubled compared with the first eye. A real eye with a diameter of 6 mm suffers from aberrations that lower the MTF (third hypothetical eye). For this eye, the high spatial frequencies—the frequencies above 83 cycle/deg—are partly transmitted, and therefore, some contrast from these frequencies is expected in the image.

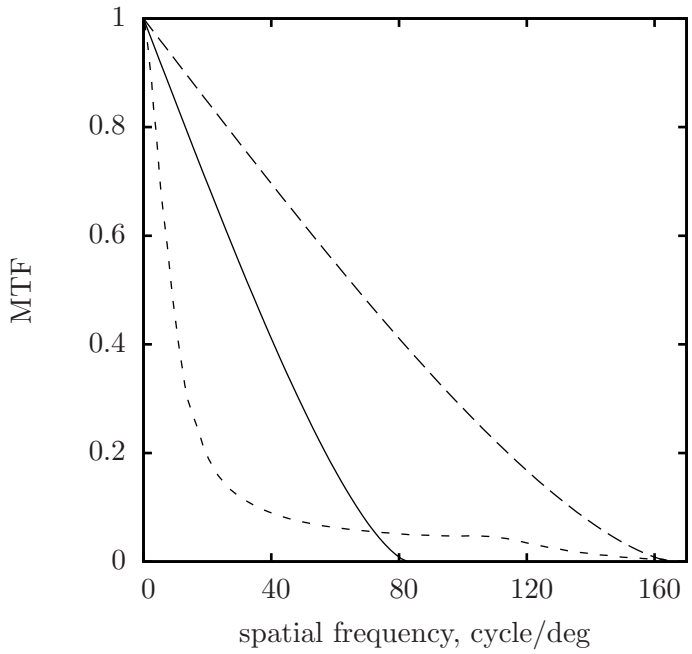

Fig. 1.5. Plot of the modulation transfer function (MTF) at a wavelength of 633 nm for three hypothetical eyes; continuous line, diffraction limited eye with a 3-mm diameter pupil; long-dashed line, diffraction limited eye with a 6-mm diameter pupil; short-dashed line, aberrated eye with a 6-mm diameter pupil obtained from the average of the MTF measured in a population of 200 eyes [61].

Miller *et al.* [62] imaged the ocular fundus using a large pupil diameter (5–6 mm) and with corrected defocus and astigmatism. These authors obtained images of the cone photoreceptor mosaic as close to the *foveola* as 0.5° of eccentricity, where the separation between the cones was found to be 3.5 μm. The mosaic was visible in the images of two subjects out of six. For all subjects except one, the quasi-periodic cone spacing was obtained from the radius of a ring structure—the Yellot's ring [63, 64]—in the average power spectrum of the image. The normalised power of this ring was 10^{-4}, which corresponds to a contrast of 2 % for the cone mosaic in the retinal images. In one subject, the cone spacing was measured directly from the image. This work showed that it is possible to image the cone photoreceptor mosaic with low contrast using a large pupil diameter. However, to obtain high contrast images of the retina in the whole population, the aberrations of the eye, beyond defocus and astigmatism, must be corrected.

Adaptive optics

The astronomers have always been confronted with the unpredictable aberrations caused by the random variations of density of air masses in the atmosphere. To minimise the effect of the atmosphere, large telescopes are built high in the mountains. Nevertheless, the astronomical images are still limited by the aberrations induced by the atmosphere. Babcock was the first to propose the use of an active system to measure and to correct the atmospheric aberrations [65]. His idea led to the adaptive optics (AO) technique, which is implemented in many large ground-based telescopes [66–68].

An adaptive optics system consists of three elements; a wavefront sensor, which measures the aberrations; a control system, which converts the aberration data into commands for the last element; a wavefront corrector, which locally retards or advances the wavefront to correct the aberrations. Arranged in a closed-loop configuration, the adaptive optics system continuously minimises the measured aberrations.

After the pioneering work of Dreher *et al.* [69], the first complete adaptive optics system developed to correct the ocular aberrations was realised by Liang *et al.* in 1997 [1]. These authors used a Hartmann–Shack wavefront sensor—described in Chapter 2—and a membrane deformable mirror (DM). The loop consisted in a wavefront measurement (mean of 6 frames with an acquisition time of 4 seconds) and in the application of 10 % of the needed correction (low gain). This loop was repeated 10 to 20 times until the root mean square (RMS) of the wavefront aberration was minimum and stable. Figure 1.6 shows the images of the cone photoreceptor mosaic obtained (a.) without and (b.) with adaptive optics. After adaptive optics correction of the ocular aberrations, the contrast of the cone photoreceptor mosaic is greatly enhanced. Using the same setup as Liang *et al.*, Roorda and Williams obtained the arrangement of the three classes of cone photoreceptors by selective bleaching of the photopigments [70].

With the development of fast wavefront sensor, the response time of the close-loop system was greatly reduced, enabling a partial correction of the time-varying aberrations [71–73]. The cone photoreceptor mosaic images obtained with these systems provided evidences that: for two types of colour blindness, the arrangement of cones in the mosaic is differently affected [74]; the reflectance of individual cones varies in a

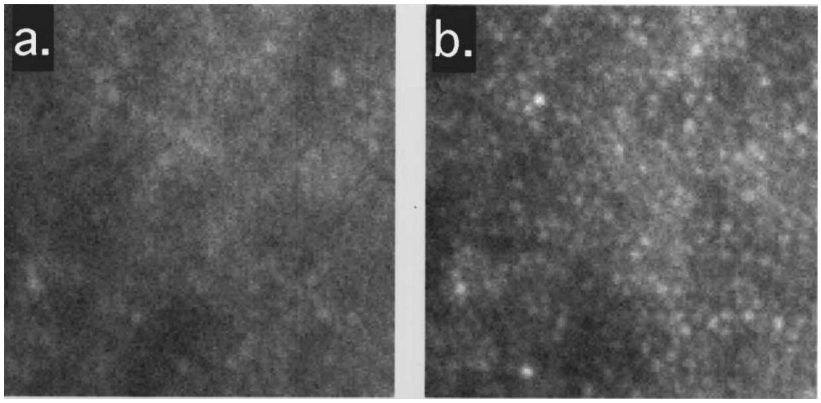

Fig. 1.6. Images of the cone photoreceptor mosaic obtained at an eccentricity of 0.8° from the *foveola* of a normal eye, (a.) without (b.) with adaptive optics. For (a.), the defocus and astigmatism were corrected. The images are square with a side of 20 arcmin. Reproduced from [1].

seemingly random fashion [75, 76]. These variations were found to depend on the coherence of the incident light and may be the result of an interference between the light reflected at different interfaces within the cone segments [77]. The amount of reflectance variations is increased after visual stimulation of the photoreceptors [77]. Recently, images of *rod* photoreceptors in the eye of two rod monochromat—absence of cone function—have been reported [78]. It should be mentioned, that besides imaging, the fast wavefront sensors are used to study the dynamic of the ocular aberrations [79–82].

Adaptive optics enables retinal imaging with unprecedented resolution and allows the visualisation of individual cells of the outer retina. In front of the photoreceptor cells in Fig. 1.6, however, the numerous cells of the inner retina are not visible. A technique having some depth resolution is needed to obtain an image of the inner part of the retina.

1.6 Depth-resolved imaging of the retina

By observing the fundus from two laterally displaced positions within the subject's pupil, our binocular vision is restored, and with it, the perception of depth. The binocular ophthalmoscope reveals the shape of the optic disc: an excavation in glaucoma; a protrusion in a *papillœdema* [83]. The depth information is recorded by taking two photographs of the fundus from two different positions within the pupil. These photographs

are viewed stereoscopically [41, 83].

The thickness of the retina was measured using a similar optical geometry by Zeimer *et al.* [27, 84]. The retina was illuminated by a scanning slit using a small pupil on one side of the dilated pupil of the subject. Images of the fundus are recorded using a small pupil on the other side of the subject's pupil. In the fundal image, the light reflected by the inner limiting membrane is laterally shifted compared to the light returning from the deeper layers. This lateral displacement is a measure of the thickness of the retina.

Scanning laser ophthalmoscope

The scanning laser ophthalmoscope (SLO) was introduced by Webb *et al.* [85]. This instrument builds an image sequentially using a spot of laser light scanned in a raster across the fundus. The light returning from the eye is detected by a point photodetector. The time-varying electric signal is recorded or is fed into a standard analog TV for display.

The contrast obtained from a scanning system is enhanced by using a pinhole conjugated with the point illumination [86]. The pinhole blocks the light contribution from out-of-focus planes and provides depth discrimination. Webb *et al.* described the first confocal SLO and the effect of different pinhole apertures on the fundal image [87].

Clinicians have access to several commercial confocal SLO instruments to obtain a wide-field fundal image (Optos, United Kingdom), to measure the topography of the optic nerve head and for fluorescein angiography (Heidelberg Engineering, Germany), and to measure the thickness of the nerve fibre layer (GDx, Carl Zeiss, Germany). This last system measures the retardation induced by the form birefringence of the nerve fibre layer from the state of polarisation of the light [88, 89]. Another image modality, which was available commercially, is the mapping of the blood circulation [90] measured using the Doppler effect [91].

The resolution limit, the contrast, and the sectioning capability of the confocal SLO are improved by correcting the ocular aberrations. Using an adaptive optics system, Roorda *et al.* obtained confocal SLO images of the nerve fibre layer, the blood capillary network, the cone photoreceptors [92, 93], the leukocytes [94], the lamina cribrosa [95], and the retinal pigment epithelial cells [96]. Chui *et al.* measured the density of cone photoreceptors from impressive photo montages covering a field of 10–12° [97] and Sung *et al.* presented images of cellular structures

within the nerve fibre layer [98]. These structures are believed to be the end-feet of astrocytes on small blood vessels.

Optical coherence tomography

In parallel to the development of the confocal SLO, optical coherence tomography (OCT) was developed [28]. OCT is based on optical low coherence reflectometry, a technique introduced in 1987 to measure back reflection from an optical fibre using a Michelson's interferometer and a broadband source [99]. The position of the defects and the strength of the associated reflections are measured from the optical path length of the reference arm of the interferometer and from the amplitude modulation of the signal.

The first OCT images of a living human retina were obtained in 1993 [100, 101]. Following these pioneering works, OCT was and is still rapidly developing. Using a source with a large spectrum, Drexler *et al.* obtained a depth resolution of $3\,\mu$m in the retina [102]. The acquisition time was reduced by analysing the OCT signal in the Fourier domain [103] using a diffraction grating—and avoiding the longitudinal scan of the reference mirror. The first Fourier domain OCT images of the fundus were acquired in 2002 [104]. To increase the lateral resolution, an adaptive optics system is used [105–108]. The OCT images obtained after adaptive optics correction of the aberrations have a higher signal to noise ratio than the images obtained without AO correction. These systems produce images of the cone photoreceptor mosaic and of the retinal microvasculature. The resolution volume of these systems is smaller than the dimension of the retinal cells. However, as shown in Fig. 1.7 and discussed by Zhang *et al.*, the speckle noise obstructs the details of the retinal cellular structures [106].

The latest development in adaptive optics OCT include the use of

- two correcting mirrors for better correction of the ocular aberrations [109, 110],
- an achromatising lens to correct the longitudinal chromatic aberration [110, 111], and
- faster detectors to enable multiple scan averaging [110].

With these systems, details of the segments of the cone photoreceptors are visible. In the inner retina, the nerve fibre bundles and structures

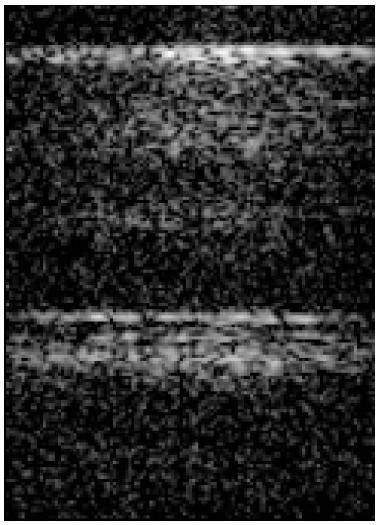

Fig. 1.7. 100-μm wide retinal cross-section imaged with an adaptive optics OCT system with a resolution of $3\times3\times5.7\,\mu\text{m}^3$. The focus is at the inner limiting membrane (ILM). RPE is the retinal pigment epithelium. Reproduced from [106].

in the ganglion cell layer are visible (see Fig. 1.8).

1.7 Contrast mechanisms

The high-resolution and the depth-resolved images discussed thus far are based on amplitude contrast. These images reveal spatial variations of absorption, scattering, and reflectance of the fundus. Another contrast mechanism currently in use is fluorescence.

The lipofuscin pigment located in the retinal pigment epithelium (RPE) cells naturally fluoresces. This autofluorescence signal is weak, but by adding 1000 to 1700 co-registered frames, the mosaic of the RPE cells was imaged in monkeys by Gray *et al.* [112] and in humans by Morgan *et al.* [113], using an adaptive optics confocal SLO. To my knowledge, *in vivo* measurements of the autofluorescence from other retinal cells have not been reported.

In animals, fluorescent markers are used to label specific cells. Images of the soma of different cell types have been obtained in mice [114], rats [115–117], and monkeys [112,117]. Using an adaptive optics confocal SLO, the soma and processes of microgial cells were imaged in mice [118] and the soma, the dendrites, and the axon of ganglion cells were imaged

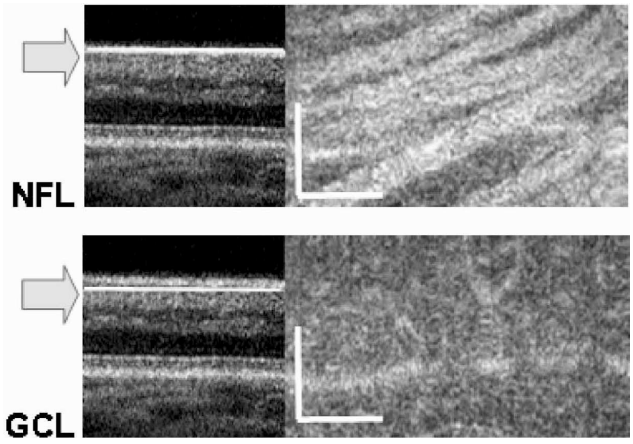

Fig. 1.8. Cross-section and en-face adaptive optics OCT images ($3\times3\times6\,\mu m^3$ resolution) of: Top, the nerve fibre layer (NFL); Bottom, the ganglion cell layer (GCL). The arrows mark the estimated focus position and the white line the depth position of the en-face view. The scale bar is $100\,\mu m$ at the retina. Reproduced from [109].

in two *macaca mulatta* monkeys [119]. An image of the ganglion cells of a monkey is shown in Fig. 1.9. This image confirms that the resolution of current adaptive optics based retinal imaging system is sufficient to resolve fine details of the structures of retinal cells. Fluorescence imaging has two interesting properties. It forms images with a contrast specific to the labelled objects and it is incoherent, i.e., it does not suffer from speckle noise. Fluorescence imaging has a great inconvenience. The fluorescence dyes used in animals are toxic and their use in humans is prohibited. The largest progress that can happens for *in situ* imaging of the human retina—and medical imaging in general—is the development of non-toxic fluorescent dyes. Indeed it is difficult to think of a technique with better properties than the ones fluorescence has.

In the mean time, it is necessary to explore the feasibility of using different contrast mechanisms. The phase contrast is routinely used in microscopy to image transparent objects. For the eye, the use of the differential interference contrast [120] and of the phase contrast method of Zernike [2] have been patented. So far, however, there is no published image of human retinas obtained *in vivo* and *in situ* using these techniques. In the seventies, holograms of cat eyes have been recorded [121]. The resolution available was too low for cellular imaging. OCT is an

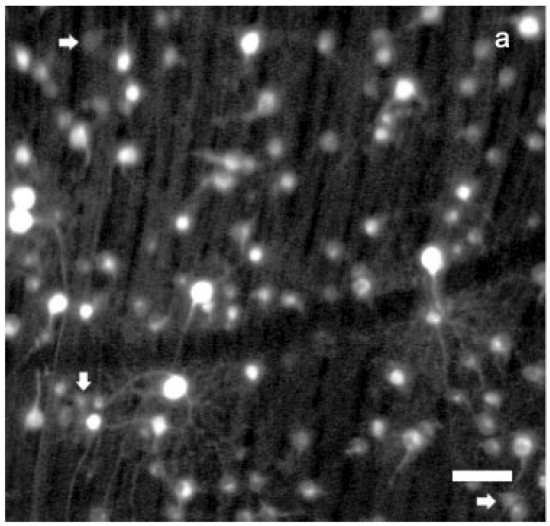

Fig. 1.9. Images of the labelled ganglion cells, their dendrites, and axons, obtained from the retina of a monkey. The scale bar represents 50 μm at the retina, about 10 arcmin. Reproduced from [119].

interferometric technique, but the phase of the interferometric signal has not been used in retinal imaging. Similarly, the OCT implementation of the differential phase contrast [122] has not been used for retinal imaging.

In this thesis, I study the possibility of using the phase information of light to image the retina. In Chapter 2, I describe the phase and the techniques used to measure it. In Chapter 3, discuss the application of these phase sensitive techniques to *in situ* retina imaging. To my knowledge, there is only one similar project, the work of Dubra on differential interference contrast*.

*Personal communication.

2

The phase

> Phase measurement permeates modern science
>
> Nugent *et al.* [123].

This quotation reveals the great importance of the phase in modern science. At the same time, though, it is rather ambiguous. What do we mean by the phase (of light)? Is there such a thing as phase measurement? Or what do we mean by phase sensitive techniques? In their very good review, these authors [123] discuss what is meant by the phase. Similarly, in this chapter I wish to explain precisely what I mean by the phase of a light wave and what we can really measure. I continue with a description of the existing phase sensitive techniques. This chapter ends with a detailed description of the phase contrast method of Zernike, which will be adapted for retinal imaging in Chapter 3.

2.1 Monochromatic light

To define the phase, I first have to introduce the time-harmonic wave, or as it is called in optics, the monochromatic wave. A time-harmonic wave is a perturbation with a constant maximum value A called the amplitude and a sinusoidal wave profile. A one-dimensional time-harmonic wave $V(z,t)$ propagating with speed v along the axis z can be represented by

$$V(z,t) = A\cos\left[\omega\left(t - \frac{z}{v}\right) + C\right]. \tag{2.1}$$

The argument of the cosine term $\omega\left(t - \frac{z}{v}\right) + C$ is the *phase* of the wave $V(z,t)$. The phase is a linear function of time t and of position z. It has

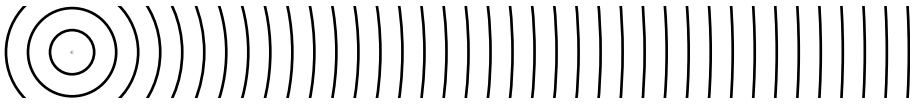

Fig. 2.1. Wavefront of a wave emitted from a point source. Redrawn from Hecht [124].

an angular frequency ω (rad/s) and it takes the value C at $t = 0$ and $z = 0$. At a fixed position $z =$ constant, the wave $V(z,t)$ oscillates with a temporal frequency ν with $\omega = 2\pi\nu$ (Hz). At a fixed time $t =$ constant, the wave $V(z,t)$ repeats itself at position z separated by a wavelength $\lambda = 2\pi/k$, with the propagation number $k = \omega/v$ (rad/m).

A scalar optical wave propagating through space has an amplitude and a phase that depends on position. Such a wave may be represented by

$$V(\mathbf{r},t) = A(\mathbf{r})\cos\left[\omega t - \phi(\mathbf{r})\right], \tag{2.2}$$

where $\mathbf{r}(x,y,z)$ is a vector position of a point P in space and $\phi(\mathbf{r})$ is a real function of position. The wave function $V(\mathbf{r},t)$ must obey the wave equation [60]. Therefore the function $\phi(\mathbf{r})$ cannot be arbitrarily defined through space. Now, the time dependence of $V(\mathbf{r},t)$ can be factored by writing the wave as the real part of a complex wave function

$$V(\mathbf{r},t) = \mathrm{Re}\left\{U(\mathbf{r})\exp(-\mathrm{i}\omega t)\right\}, \tag{2.3}$$

where

$$U(\mathbf{r}) = A(\mathbf{r})\exp\left[\mathrm{i}\phi(\mathbf{r})\right]. \tag{2.4}$$

$U(\mathbf{r})$ is called the *complex amplitude* of $V(\mathbf{r},t)$. The function $\phi(\mathbf{r})$ represents the spatial dependence of the phase of $V(\mathbf{r},t)$ and we can visualise it by tracing surfaces of constant phases called *wavefronts*. As an example, the wavefronts of a spherical wave, each separated by 2π, are shown in Fig. 2.1.

In the absence of diffraction, the wave propagates along a direction perpendicular to the wavefront. This is the basis of geometrical optics. In this case, $\phi(\mathbf{r})$ along the direction of propagation z is given by $\phi(z) = kz + C$, which is the basic equation that relates the phase of the complex amplitude to the physical distance z. This equation can be rewritten in a form where the effect of the medium is separated from the wave property k. As the wave velocity $v = c/n$ with c the velocity of light in

vacuum and n the refractive index of the medium, we can introduce the propagation number in vacuum $k_0 = \omega/c$. Now $\phi(z)$ is

$$\phi(z) = k_0 n z + C, \tag{2.5}$$

where the product nz is called the optical path length l.

2.2 Phase objects

We have seen how the phase of a light wave is related to the optical path length. Now we define a *phase object* as an object that affects primarily the phase of the light wave being transmitted through it or reflected from it. When the amplitude of the wave is unaffected, phase objects are transparent. These objects are frequently met in biology, e.g., single cells, and in optical metrology, e.g., surface figure, and in other subjects. Figure 2.2 illustrates the effect of refractive index and physical distance on the wavefronts, neglecting the effect of diffraction. In each case, the object is split in two parts $\mathcal{A}$ and $\mathcal{B}$ between which the optical path length is different. At the top of Fig. 2.2, the wave is transmitted through an object with two different refractive indexes n_1 and n_2. In the middle, the wave is transmitted through an object with difference of thickness. At the bottom left, the wave is incident on a surface with different heights, and at the bottom right, the corresponding reflected wavefront is shown.

For the transmitted wavefronts, the optical path length difference between part $\mathcal{A}$ and part $\mathcal{B}$ is

$$l_{\mathcal{A}} - l_{\mathcal{B}} = (n_1 - n_2)\, d, \tag{2.6}$$

where d is the physical length over which part $\mathcal{A}$ differs from part $\mathcal{B}$. For the reflected wavefront, the optical path length difference between part $\mathcal{A}$ and part $\mathcal{B}$ is

$$l_{\mathcal{A}} - l_{\mathcal{B}} = 2d, \tag{2.7}$$

for normal incidence. In both cases, the phase difference is given by

$$\phi_{\mathcal{A}} - \phi_{\mathcal{B}} = k_0 \left(l_{\mathcal{A}} - l_{\mathcal{B}}\right). \tag{2.8}$$

Note that the phase at the origin, the constant C in Equation 2.1, is lost by taking the difference in optical path length.

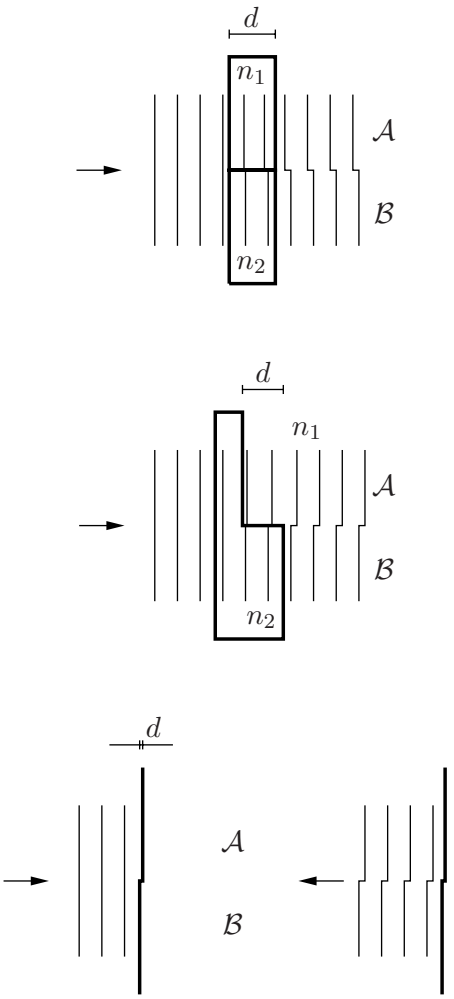

Fig. 2.2. Shape of the wavefront after interaction with a phase object, ignoring diffraction effects. Each object consists of two parts $\mathcal{A}$ and $\mathcal{B}$ with; top, different refractive indexes; middle, different thicknesses; bottom, different heights. The arrow indicates the direction of wave propagation and d indicates the physical distance over which the optical path length in part $\mathcal{A}$ is different from the optical path length in part $\mathcal{B}$.

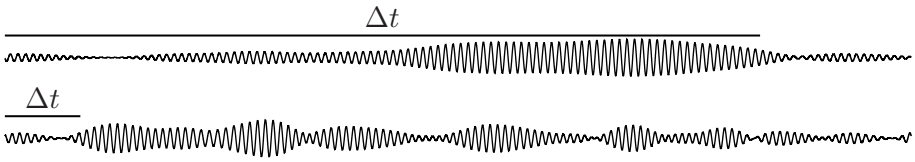

Fig. 2.3. Time-course of two quasi-monochromatic waves with Lorentzian power spectrum with $\Delta\nu/\bar{\nu}$ ratio of 0.01 (top) and 0.10 (bottom) taken at full width at half maximum.

2.3 The coherence of quasi-monochromatic light

The phase of a monochromatic wave is linearly related to the propagated distance. This relation is fully deterministic and the wave is said to be coherent. However, the nature of light is random [125]. The amplitude and the phase of light fluctuate in time. An example of two light waves with random fluctuation of amplitude and phase is shown in Fig. 2.3. In this section I will qualitatively describe how these fluctuations affect the outcome of experiments.

Representation of a randomly fluctuating wave

The temporal power spectrum of a fluctuating wave has a region over which its components are significant. The width of this region is called the spectral width $\Delta\nu$. When the spectral width is much smaller than the mean temporal frequency $\bar{\nu}$, $\Delta\nu/\bar{\nu} \ll 1$, the wave is called *quasi-monochromatic*. The time-varying wave may be written in a form similar to Equation 2.3 [8]

$$V(\mathbf{r},t) = \mathrm{Re}\left\{U(\mathbf{r},t)\exp(-\mathrm{i}\bar{\omega}t)\right\}, \tag{2.9}$$

where $\bar{\omega}$ is the mean angular frequency. The complex amplitude $U(\mathbf{r},t)$ is a *time-varying* random process, with a characteristic time $\Delta t \approx 1/\Delta\nu$. For time periods shorter than Δt, the probability that the complex amplitude remains essentially constant is high. Whereas, for time periods longer than Δt, this probability is low. A quasi-monochromatic wave has a complex amplitude $U(\mathbf{r},t)$ that varies slowly compared to the period of the wave $1/\bar{\nu}$. $U(\mathbf{r},t)$ can be interpreted as the envelope of the wave.

The waves in Fig. 2.3 have been generated from a sum of 20 monochromatic waves with amplitude and frequency following a Lorentzian

power spectrum* and with random phase. The wave on top has a $\Delta\nu/\bar{\nu}$ ratio of 0.01 and the wave at the bottom a ratio of 0.10 taken at full width at half maximum.

Statistical properties of the wave

The knowledge of two statistical properties of the wave is sufficient to explain the results of most experiments. These properties are the intensity and the complex degree of coherence.

The instantaneous intensity of a wave is the random process defined by $I(\mathbf{r},t) = |V(\mathbf{r},t)|^2$. Assuming stationarity, its expected value is the time average

$$I(\mathbf{r}) = \lim_{T\to\infty} \frac{1}{T} \int_{-\frac{T}{2}}^{\frac{T}{2}} U(\mathbf{r},t)U^*(\mathbf{r},t)\,\mathrm{d}t, \tag{2.10}$$

where the sign $*$ denotes the complex conjugate. The *average* intensity $I(\mathbf{r})$ is the quantity approximated by a light detector. The measured signal—the intensity—is the time average of $I(\mathbf{r},t)$ given by Equation 2.10, but taken over a finite time period T equals to the detector integration time. In general, this period is much longer than the characteristic time, $T \gg \Delta t$, and the measured intensity is a good approximation of $I(\mathbf{r})$.

The *complex degree of coherence* $\gamma(P_1,t_1,P_2,t_2)$ is a measure of the correlation between the variations of the wave at a point P_1 and time t_1 and the variations at a second point P_2 and time t_2. Assuming stationarity and using $\tau = t_2 - t_1$, the complex degree of coherence is defined by

$$\gamma(P_1,P_2,\tau) = \frac{\Gamma(P_1,P_2,\tau)}{\sqrt{\Gamma(P_1,P_1,0)}\sqrt{\Gamma(P_2,P_2,0)}}, \tag{2.11}$$

where $\Gamma(P_1,P_2,\tau)$ is the *mutual coherence function*

$$\Gamma(P_1,P_2,\tau) = \lim_{T\to\infty} \frac{1}{T} \int_{-\frac{T}{2}}^{\frac{T}{2}} U(P_1,t+\tau)U^*(P_2,t)\,\mathrm{d}t. \tag{2.12}$$

The absolute value of the complex degree of coherence is bounded to 1, $|\gamma(P_1,P_2,\tau)| \leq 1$ [125], and it represents the coefficient of correlation between $U(P_1,t_1)$ and $U(P_2,t_2)$. The argument of the complex

*A power spectrum with a Lorentzian shape follows $L(\nu) = C\frac{w}{w^2+(\nu-\nu_0)^2}$, where C is a constant, w is the half width at half maximum, and ν_0 is the central temporal frequency. For the example given, $\Delta\nu = 2w$.

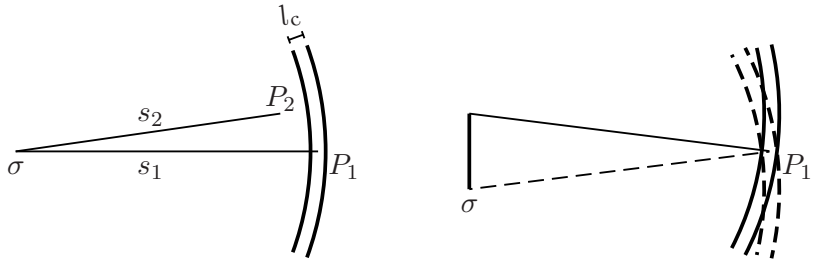

Fig. 2.4. Illustration of the spatial degree of coherence of a wave from a point source (left) and from an extended source (right). l_c is the coherence length.

degree of coherence is the average phase difference between $U(P_1, t_1)$ and $U(P_2, t_2)$.

The *temporal* degree of coherence of the wave is obtained from the complex degree of coherence $\gamma(P_1, P_1, \tau)$ by varying τ. When $\tau \ll \Delta t$, $|\gamma(P_1, P_1, \tau)|$ is large and the wave is said to have a large degree of coherence. When τ is sufficiently large, $|\gamma(P_1, P_1, \tau)|$ is small and the wave is said to have a low degree of coherence. The transition between these two extreme conditions depends on the shape of the average power spectrum of the wave. To be more specific, $\Gamma(P_1, P_1, \tau)$ and the average power spectrum of the wave form a Fourier transform pair [8]. By a suitable definition of the width of $\gamma(P_1, P_1, \tau)$, we obtain a coherence time τ_c and the corresponding coherence length $l_c = c\tau_c$.

The *spatial* degree of coherence of the wave surrounding a point P_1 is obtained from $\gamma(P_1, P_2, \tau)$ with a fixed τ, generally $\tau = 0$, and a variable P_2. For a point source, see Fig. 2.4 (left), the spatial degree of coherence is directly related to the temporal degree of coherence of the wave. When the difference between the optical path length s_1 from the source σ to the point P_1 and the optical path length s_2 from σ to the point P_2 is smaller than the coherence length l_c, $s_2 - s_1 \ll l_c$, the spatial degree of coherence is high. As seen in Fig. 2.4 (left), the spatial degree of coherence is constant over a spherical surface centred on the point source σ. For an *extended* source, the spatial degree of coherence depends on the temporal degree of coherence and on the angle subtended by the source at the object. Let the source be composed of a large number of uncorrelated point sources. In Fig. 2.4 (right), the zone of high spatial coherence surrounding the point P_1 for the wave of two point sources, one from the top edge of the extended source and the

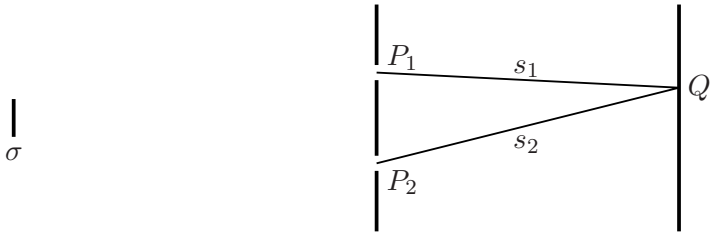

Fig. 2.5. Interference experiment with quasi-monochromatic light from an extended source σ. Redrawn from Born and Wolf [8].

other from the bottom edge, are drawn. These two zones overlap only for a small area surrounding P_1. In this area, all the waves from the different point sources have a large degree of coherence, and therefore, the resultant wave also has a large degree of coherence. At a point P_2 located at a greater distance from P_1, only a few individual waves have a large degree of coherence, and the resultant wave has a low degree of coherence.

The result of this qualitative discussion is that surrounding a point P, there is a volume of space within which the wave from an extended source is highly correlated. Over that volume, the wave may be modelled as a monochromatic wave and it is considered to be coherent.

Interference

When two, or more, components of a wave add, the resulting complex amplitude is the sum of the individual amplitudes. In the experimental setup shown in Fig. 2.5, the light from an extended source σ illuminates a first screen with two pinholes, one at P_1 and the other at P_2. The light transmitted by each pinhole propagates to the second screen where their complex amplitudes add. The average intensity of the wave at Q can be written as [8]

$$I(Q) = I_1(Q) + I_2(Q) + 2\sqrt{I_1(Q)}\sqrt{I_2(Q)}Re\left\{\gamma(P_1, P_2, \tau)\right\}, \quad (2.13)$$

where $I_1(Q)$ and $I_2(Q)$ are the intensity at Q from the light that passed through the pinhole at P_1 and at P_2, respectively. Where, the complex degree of coherence is taken between the point P_1 and P_2 with a time delay $\tau = (s_2 - s_1)/c$, a delay equals to the difference in time it takes to the wave to propagate from each pinhole to Q.

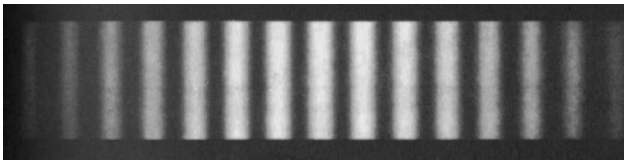

Fig. 2.6. Interference fringes from the experimental setup shown in Fig. 2.5. At the centre, the Equation 2.14 holds. At the edge, both the total intensity and the fringe visibility decrease. This is due to intensity variations from the light from both pinhole and a decrease in the complex degree of coherence for a large time delay τ. Vertical bands of high intensity are zones of constant phase differences. Reprinted from Hecht [124].

The spatial variations of the average intensity of the wave on the second screen can be found by varying the point Q. Provided that the pinhole apertures and their separation are sufficiently small compared to the distance between the two screens, the intensity distribution dues to each pinhole on the screen is approximately constant. The two terms $I_1(Q)$ and $I_2(Q)$ form a uniform background intensity. The third term depends on the complex degree of coherence, which is a function of τ. For a quasi-monochromatic wave, the absolute value of $\gamma(P_1, P_2, \tau)$ varies slowly with τ and may be considered constant [8]. The argument of $\gamma(P_1, P_2, \tau)$, however, varies linearly with τ. Therefore, the third term of the Equation 2.13 adds a sinusoidal intensity modulation on a constant background.

When $|\gamma(P_1, P_2, \tau)| > 0$, different zones of high intensity separated by zones of low intensity can be observed on the screen, see Fig. 2.6. These zones are called fringes and their visibility $\mathcal{V}$, as defined by Michelson, is

$$\mathcal{V} = \frac{I_{\max} - I_{\min}}{I_{\max} + I_{\min}} = \frac{2\sqrt{I_1(Q)}\sqrt{I_2(Q)}}{I_1(Q) + I_2(Q)} \left|\gamma(P_1, P_2, \tau)\right| . \tag{2.14}$$

The fringes represent the wrapped phase of the wave. There is an average phase shift of π between a point Q located on a maximum intensity and all the points located at the nearest minimum zone. The next maximum has an average phase difference of 2π. To conclude, the fringes obtained from the addition of two correlated wave components reveal the optical path length difference between the path of these components. When the two components are not correlated, the fringes are not visible and the phase information cannot be retrieved.

Dispersion

An additional comment should be made on the optical path length for a quasi-monochromatic light. As the refractive index of a medium is a function of the temporal frequency ν of the wave, the optical path length depends on the temporal frequency as $l(\nu) = n(\nu)d$. This dependence gives rise to the phenomenon of dispersion. Here we will assume that $\Delta\nu$ is small and that n is constant over the temporal spectrum of the source.

2.4 Phase sensitive techniques

To measure the *absolute* phase of a wave, the waveform has to be properly sampled. The measurement duration must be much shorter than the wave period $1/\nu$, about 10^{-15} s at visible frequencies. Although the wave property of light was first discussed about 300 years ago, it is only in the last 5 years that the electric field of a light wave has been directly measured. Goulielmakis *et al.* used bursts of electrons lasting for 1/10 of the period of the light wave to probe its electric field. The electrons are accelerated by the electric field and their momentum reveals the field strength [126]. We can answer one of the questions from the beginning of this chapter. Yes, phase measurement is possible, but up to now, it is the exception rather than the norm.

Instead, the energy of the light wave is commonly converted into heat or into electric charges using photo-sensitive detectors [127]. This transduction process is slow compared to the period of the wave and the absolute phase is lost. As discussed in Section 2.3, the detected signal, the intensity, is the time average of the complex amplitude of the wave. When the wave has a high degree of coherence, the intensity shows spatial variations linked to the average phase difference between the different wave component that add at the detector sensitive surface. The term *phase* in *phase*-sensitive techniques generally refers to these average phase differences, or through the Equation 2.13 to differences in optical path length.

All the phase-sensitive techniques used in practice are based on the coherent addition of wave components. As Nugent *et al.* [123] wrote, these techniques are numerous and they have found many applications in modern science. Assuming that the wave has a high degree of coherence, I now discuss different phase-sensitive techniques classified in

three categories: interferometry, propagation, and imaging.

Interferometry

In this category, I discuss the techniques that resolve interference fringes. These fringes result from the addition of two waves or from the addition of a multitude of waves. The fringe maximum intensity is obtained when the optical path length of all the waves are the same or separated by a multiple of the wavelength λ.

When a single frame is available, the phase of the wave is obtained from the position of centre lines corresponding to the maximum intensity of each fringe. The spatial sampling of the wave depends on the number of fringes present across the field of interest. When a series of frames is obtained, each frame with a different reference phase, the phase of the wave is retrieved at each sampling point from the modulation of intensity between the frames. This technique is called phase-shifting interferometry [128].

The mechanical vibration and the air turbulence can induce time varying changes of the interference pattern. The problem is reduced if the different beams follow approximately the same optical path, such as in common-path interferometers. However, the interpretation of the measured phase is less straight forward than with separated-path interferometers because all the beams interact with the object.

Interferometric techniques are well suited for stable setups, with low level of unwanted light, and for phase varying slowly with respect to the fringe width. These conditions are generally met in the field of optical shop testing [128].

Propagation

In this category, the mixing of the wave components is obtained by propagation. According to the Huygens–Fresnel principle [8], the wavefront after propagation is found by the coherent addition of many fictitious point sources located on the previously known wavefront, all with a phase shifted by $-\pi/2$. The resulting light distribution—the diffraction pattern— shows ringing features reminiscent of interference fringes, when the degree of coherence is high. The relation between the diffraction pattern and the optical path length variations is not straightforward due to the multiplicity of wave components and the continuous differ-

ence in optical path lengths. Here, a few methods to obtain the phase of a wave from its diffraction pattern are discussed.

Irradiance transport equation. Over a very short distance of propagation, Teague has shown that the gradient of the phase in a plane perpendicular to the direction of propagation is proportional to the intensity gradient along the direction of propagation, the so-called irradiance transport equation [129, 130]. By measuring the variations of intensity between two planes separated by a short distance, it is possible to reconstruct the phase. This method was used in x-ray imaging [131]. The curvature sensor introduced by Roddier was discussed in terms of the irradiance transport equation [132, 133].

Phase retrieval algorithms. Over a large propagating distance, there is no simple relationship between the measured intensity distribution and the phase of the wave. In most optical system a stop defines an aperture through which light is propagated; This is the exit pupil. Therefore, it is possible to limit the number of possible phase distributions in the image plane by requiring that the amplitude of the back-propagated wave is zero outside the exit pupil [134]. This inverse problem is not guaranteed to have a unique solution [135, 136].

Gerchberg and Saxton introduced an iterative algorithm to retrieve the phase using pupil constraints and image constraints [137]. This algorithm starts with a random phase and the square root of the measured intensity distribution in the image. The wave is propagated to the exit pupil. The amplitude outside the aperture is set to zero. The resulting wave is propagated to the image plane, where the amplitude is replaced with the square root of the measured intensity. This procedure is repeated iteratively until the algorithm converges to a stable solution. Many variations of this algorithm have been studied [136, 138].

Hartmann–Shack wavefront sensor [68, 139]. A simple relation between intensity measurement after a large propagating distance and the phase is obtained by spatial sampling of the wave. The Hartmann–Shack sensor samples a collimated wave using an array of lenses. Each lens forms an image of the source, a spot, on its back-focal plane. As illustrated in Fig. 2.7, a wavefront with a local slope l/a incident on a

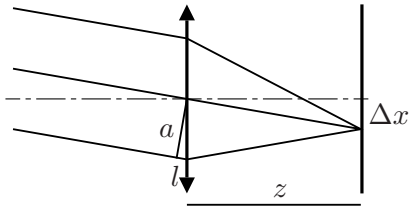

Fig. 2.7. Principle of the Hartmann–Shack wavefront sensor. A wavefront with a tilt angle given by l/a produces a light distribution displaced by Δx from the optical axis after a propagation distance z. The displacement Δx is linearly proportional to the wavefront tilt.

lens forms a spot at a distance Δx from the optical axis

$$\Delta x = \frac{l}{a}\, z, \tag{2.15}$$

where l is the optical path length difference between the centre and the edge of the lens, a is the radius of the limiting aperture, and z is the propagating distance, the focal length of the lens. The displacement Δx is obtained from the centroid of the spot. The phase of the wave is reconstructed from the slope measurements by integration or by direct least-square fit with a polynomial representation [140,141], e.g., the Zernike circle polynomials discussed in Appendix A. This sensor has three interesting properties.

- When the wavefront is not plane over the lens aperture, the centroid of the spot is proportional to the mean slope of the wavefront over the aperture, provided that the irradiance across the lens aperture is constant [142].

- Information from a non-dispersive and thin phase object can be retrieved using white light. The displacement Δx being related to the optical path length and not to the phase, the different wavefronts (different wavelengths) form superimposed spots.

- For a thin phase object, an extended source may be used. The centroid of the enlarged spot is proportional to the wavefront slope.

As the spatial sampling of the wavefront is usually coarse, this method is not well-suited to image phase objects with high spatial frequencies. This is the currently preferred wavefront sensor for ophthalmic appli-

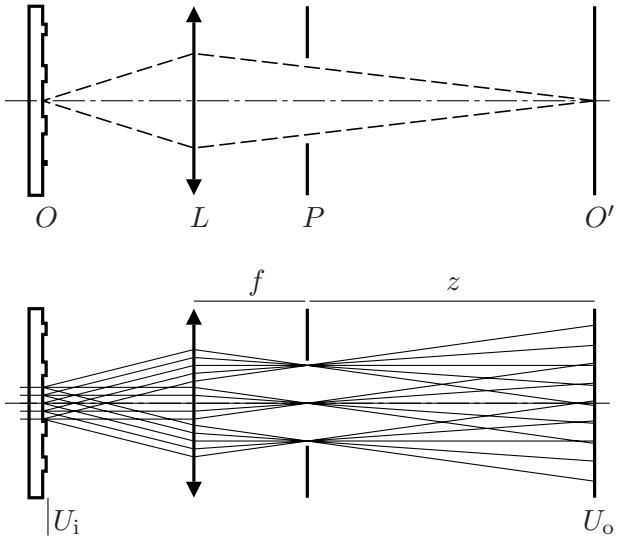

Fig. 2.8. Setup for imaging techniques. The top part shows the conjugation by the lens system L of the object O and the image O'. The bottom part shows a collimated light beam from a source located at infinity on the left. The light is diffracted by the object O. The lens system L collects the diffracted beams which are brought into focus at the back focal plane of L. Then, the light diverges and illuminates the image plane O'.

cations [1, 143] and it is used in the experimental setup described in Chapter 5.

Imaging

In this category, the different wave components are separated by diffraction by the object and they are recombined by an imaging system on a detecting plane, where they interfere. The drawings in Fig. 2.8 represent (top) the conjugation of the object O and the image plane O' by the lens system L, and (bottom) the decomposition of the incoming collimated wave by the object and the propagation of three wave components through the imaging system. An hypothetical *perfect* imaging system forms at the image plane O' a perfect replicate of the object wave—the wave immediately after transmission through the object O. For a phase object (constant amplitude), the resulting wave in the image plane has a constant amplitude and the detected image consists in a constant level of intensity. The phase information is lost. Luckily, an *imperfect* imaging system attenuates the diffracted wave components

and it shifts their phase. The interference of the filtered wave components no longer results in a constant amplitude. The harmony is broken and the detected image shows some phase structures.

In the framework of the theory of linear system, an imaging system is a complex spatial filter [60], whose properties are given by its impulse response, i.e., the image of a point source in the object. The lateral extent of the object wave is assumed infinite. Knowing the impulse response, it is possible to compute the output image for a given input object and to compare different imaging systems. Here it is assumed that the system is isoplanatic, i.e., its properties are the same for all the points in the image, and that the input wave has a high degree of coherence. For convenience, the input wave is scaled by the transverse magnification M of the system, where M is obtained from geometrical optics relation [144]. In particular, the transverse magnification M of an inverted image is negative. Then the output wave $U_{\mathrm{o}}(x, y)$ is the convolution of the input wave $U_{\mathrm{i}}(x_{\mathrm{i}}, y_{\mathrm{i}})$ with the impulse response of the system, the point-spread function $h(x, y)$,

$$U_{\mathrm{o}}(x, y) = \iint_{-\infty}^{\infty} U_{\mathrm{i}}(x_{\mathrm{i}}, y_{\mathrm{i}}) h(x - x_{\mathrm{i}}, y - y_{\mathrm{i}}) \, \mathrm{d}x_{\mathrm{i}} \, \mathrm{d}y_{\mathrm{i}}. \tag{2.16}$$

When the conditions for Fraunhofer diffraction are met*, the point-spread function is the Fraunhofer diffraction pattern of the complex amplitude distribution $H(\xi, \eta)$ in the exit pupil P of the system. $H(\xi, \eta)$ is called the pupil function and ξ, η are the spatial Cartesian coordinates in the exit pupil plane. The Fraunhofer diffraction is a Fourier transform relation evaluated at the coordinates $\xi = \lambda z u$, $\eta = \lambda z v$, with z the distance between the exit pupil and the image, and with $u = 1/x$, $v = 1/y$, the spatial frequencies of the output image. In the spatial frequency domain, the Equation 2.16 becomes a multiplication

$$\tilde{U_{\mathrm{o}}}(u, v) = \tilde{U_{\mathrm{i}}}(u, v) T(u, v), \tag{2.17}$$

*These conditions are given in reference [8]. A Fraunhofer pattern is formed in the image plane of a well corrected and centred optical system for field points located close to the optical axis. There is no criteria qualifying what is meant by a well corrected optical system. The dilated eye has notable aberrations and the use of Fraunhofer diffraction may be questioned. The major ocular aberrations are defocus and astigmatism. When the aberration consists only of a defocus term, then Fraunhofer diffraction is analogous to Fresnel diffraction.

where the symbol $\sim$ denotes the Fourier transform and where $T(u,v)$ is the coherent transfer function. As $T(u,v) = \tilde{h}(x,y)$ and $h(x,y) = \tilde{H}(\xi,\eta)$, the coherent transfer function $T(u,v) = H(-\lambda z u, -\lambda z v)$, i.e., the coherent transfer function at the spatial frequency u, v equals the pupil function at the coordinates $\xi = -\lambda z u$ and $\eta = -\lambda z v$. This important result shows how the system acts on the spatial frequency content of the image. In addition, this result suggests that the contrast in the image can be controlled by placing a spatial filter in the exit pupil. For phase imaging, the optimum filter will be one that linearly transforms the input phase into an intensity variation.

Now, the properties of different phase-sensitive techniques are discussed using their pupil functions. The quadratic phase factor of Fraunhofer diffraction is ignored, e.g., this factor would be zero in a $4f$-system. But first, the pupil function of the hypothetical *perfect* system is

$$H(\xi,\eta) = 1 \tag{2.18}$$

for all ξ and η. That is, the size of the exit pupil is infinite. The convolution kernel, the point-spread function, is the unit-area impulse $\delta(x,y)$ [145] and $U_\mathrm{o}(x,y) = U_\mathrm{i}(x_\mathrm{i}, y_\mathrm{i})$ everywhere.

Low-pass filter. The exit pupil, by itself, limits the spatial frequencies transmitted by a system. In optics, this is described by the diffraction phenomenon. The pupil function of an aberration-free system is

$$H(\xi,\eta) = \begin{cases} 1 & \text{in the aperture,} \\ 0 & \text{outside the aperture.} \end{cases} \tag{2.19}$$

The imaging system is a low-pass filter and the images are band-limited. The presence of a phase object can be detected when a significant amount of its spatial frequency content is blocked by the pupil. This condition is met when the object has discontinuities as the object shown in Fig. 2.8. These discontinuities are imaged as dark lines surrounded by diffraction features. To perceive more phase information, the system can be stopped down. This gain in phase visualisation is obtained by sacrificing resolution.

Phase distortion. The different spatial frequencies follow different optical paths through the system. When the length of these paths are

not all identical, the different beams at the image plane are out of phase. The image suffers from phase distortion and the system is said to be aberrated. The pupil function is

$$H(\xi, \eta) = \exp\left[\mathrm{i}kW(\xi, \eta)\right], \tag{2.20}$$

where $W(\xi, \eta)$ is the optical path difference across the exit pupil. As for the low-pass filtering method, the phase information is obtained at the expense of resolution, to some extent. The results obtained using the irradiance transport equation may be found by introducing an equivalent amount of defocus in the pupil function. The effect of a combination of different aberrations can be analysed. For example, spherical aberration and defocus can be balanced to optimise the transfer of the phase information, as in electron microscopy [146].

Knife-edge test. The harmony between all the diffracted components is broken by blocking one half of the exit pupil. This is the essence of the knife-edge test introduced by Foucault in 1858 [147, 148]. When the obstruction, the knife, is introduced along the ξ coordinate, the pupil function is

$$H(\xi, \eta) = \begin{cases} 0 & \text{for } \xi < 0, \\ 1 & \text{for } \xi \geq 0. \end{cases} \tag{2.21}$$

The corresponding point-spread function is $0.5[\delta(x, y) - \mathrm{i}/(\pi x)]$. The output wave is composed of a constant background and of the Hilbert transform of the input wave [145]. The resolution of the test is very good and its phase sensitivity is very high. This sensitivity can be lowered by reducing the blocked area. The phase information is viewed as an elevation profile illuminated at grazing incidence with light coming from the side opposite to the knife [128]. This method is also known as the Schlieren technique from the work of Toepler who used it to image glass streaks—Schlieren in German—and who applied it to the study of the movements of air masses [149]. By replacing the knife with a phase shift of π, Wolter obtained the phase-edge test [128]. Its pupil function is

$$H(\xi, \eta) = \begin{cases} -1 & \text{for } \xi < 0, \\ 1 & \text{for } \xi \geq 0, \end{cases} \tag{2.22}$$

and the output wave is the Hilbert transform of the input wave [150]. A closely related technique is the pyramid wavefront sensor [151], where the knife is replaced by a four-faced pyramid. Four images of the object are detected and the phase gradients along two directions are calculated. This wavefront sensor was recently used to measure the ocular aberrations in humans [152, 153].

Dark-field method. By removing the direct light, as first discussed by Lister in 1830 [154], the constant background is eliminated. Therefore, the visibility of intensity variations is improved. The direct light is the undiffracted component. To remove it, the needed pupil function is

$$H(\xi,\eta) = \begin{cases} 0 & \text{for } \xi = \eta = 0, \\ 1 & \text{for } \xi \neq 0 \text{ and } \eta \neq 0. \end{cases} \tag{2.23}$$

In microscopy, a similar effect is obtained without a special filter by illuminating the object from an annulus aperture forming an incident angle larger than the acceptance angle of the objective. This pupil function is a high-pass filter that enhances the edges of the object [155].

Phase contrast method of Zernike. If the central obscuration of the dark-field method is replaced by a phase plate that shifts the direct light by $\pm\pi/2$ with respect to the diffracted light [156], the pupil function becomes

$$H(\xi,\eta) = \begin{cases} \pm\mathrm{i} & \text{for } \xi = \eta = 0, \\ 1 & \text{for } \xi \neq 0 \text{ and } \eta \neq 0, \end{cases} \tag{2.24}$$

and the image consists in a constant background modulated by the phase information. For a small phase object, an object with small phase excursion, the obtained intensity modulation is linear with the input phase. This method is discussed in detail in Section 2.5. Recently, Yelleswarapu *et al.* presented a self-aligned phase contrast system [157]. In this system, the direct light heats a liquid crystal and induces the needed phase shift. Another recent modification is the use of a number a point sources and the corresponding phase-shifting area located randomly over the exit pupil [158].

Other imaging methods. Here I cite a few methods that can be added to this list. There is the grating filter used by Ronchi in his grating

interferometer [128, 159]. The three bands with different transmittance used by Hoffman and Gross in the modulation contrast [160, 161]. The spiral phase filter is used to enhance the edge of an object [162].

Unclassified techniques

The three above categories are too rigid to allow the classification of the two following techniques.

The differential interference contrast (DIC) of Nomarski [163] is a lateral shearing interferometer. Two cross-polarised and laterally displaced beams are generated by transmission through an uniaxial crystal, e.g., Wollaston prism, in the pupil plane of the system. After interaction with the object, the two beams are recombined by transmission through the same or another uniaxial crystal. The two beams interfere and an image of the phase gradient along the shear direction is obtained.

Holography [164] and its modern implementation, the digital holography [165], use the interference between a wave reflected by the object with a reference wave to record the amplitude and the phase of the object wave. The reference wave being a carrier wave modulated by the object wave. The hologram is recorded in the exit pupil. The image is obtained by reconstruction of the object wave either by illuminating the hologram by the reference wave or by digital reconstruction.

2.5 The phase contrast method of Zernike

As briefly introduced in Section 2.4, the phase contrast method of Zernike is an imaging phase-sensitive technique. The corresponding spatial filter is a phase plate that shifts the direct light by $\pi/2$. The image obtained is a mapping of the phase variations of a wave due to a phase object. Unlike all the other imaging methods described, the phase contrast method of Zernike produces an intensity image linearly related to the phase object when the phase variations are small and the effects of diffraction are limited.

It is by experimenting with diffraction gratings that Zernike fully realised the importance of the phase of the different components of the diffracted spectrum and that the phase of individual diffraction lines can be manipulated [166]. He published the phase contrast method in 1934 [156, 167] as an improved knife-edge test and in 1942 as a microscopic technique [168, 169].

The same technique was discovered independently by Lyot in 1946 for testing astronomical objectives [170] and by Armstrong in 1936 for signal transmission using radio waves [171]. Armstrong called his technique frequency modulation (FM).

Principle of the method

The filter introduced by Zernike transforms an optical system sensitive to the amplitude of the wave into an optical system sensitive to the phase. This transformation is best illustrated by considering two objects that carry the same information $f(x_\mathrm{i}, y_\mathrm{i})$ encoded once in amplitude (amplitude object) and once in phase (phase object). The images of these two objects formed by an optical system with and without the phase plate are then compared. The imaging system considered is the one shown in Fig. 2.8. The finite extent of the object and the exit pupil is neglected. A summary of this discussion is presented in Table 2.1.

For a plane-wave illumination with an unit-amplitude, the input wave $U_\mathrm{i}(x_\mathrm{i}, y_\mathrm{i})$ is equal to the complex transmittance of the object. As the complex transmittance of a passive amplitude object is real and takes values between 0 (no transmission) and 1 (100 % transmission), the information $f(x_\mathrm{i}, y_\mathrm{i})$ must be encoded as a modulation around the mean transmittance of the object. Therefore the input wave for the amplitude object takes the form $U_\mathrm{i}(x_\mathrm{i}, y_\mathrm{i}) = 1 + f(x_\mathrm{i}, y_\mathrm{i})$, where the constant term 1 is the normalised mean transmittance of the object. The complex transmittance of a phase object is the complex exponential $\exp[\mathrm{i}f(x_\mathrm{i}, y_\mathrm{i})]$. When the object has small phase excursions $|f(x_\mathrm{i}, y_\mathrm{i})| \ll 1$, the exponential can be approximated by the first two terms of its expansion in Taylor series*

$$\exp[\mathrm{i}f(x_\mathrm{i}, y_\mathrm{i})] \approx 1 + \mathrm{i}f(x_\mathrm{i}, y_\mathrm{i}). \tag{2.25}$$

The input wave for the phase object is $U_\mathrm{i}(x_\mathrm{i}, y_\mathrm{i}) \approx 1 + \mathrm{i}f(x_\mathrm{i}, y_\mathrm{i})$. The difference between the amplitude encoding and the phase encoding is a phase shift of $\pi/2$ of the spatially varying term.

Now, these two input waves are imaged by a *perfect* imaging system. The upper part of Table 2.1 shows the light distribution in the output pupil plane, which is proportional to the inverse Fourier transform of the scaled input wave $\tilde{U}_\mathrm{i}(-u, -v)$, the output wave $U_\mathrm{o}(x, y) = U_\mathrm{i}(x_\mathrm{i}, y_\mathrm{i})$, and the corresponding intensity $I_\mathrm{o}(x, y) = U_\mathrm{o}(x, y)U_\mathrm{o}^*(x, y)$. For the

*$\exp(x) = 1 + \frac{x}{1!} + \frac{x^2}{2!} + \frac{x^3}{3!} + \cdots + \frac{x^n}{n!} + \cdots \quad |x| < \infty$

Table 2.1. Image formation of an amplitude and of a phase object; Top, without the phase plate, bottom with the phase plate.

	amplitude object	weak phase object
$U_{\mathrm{i}}(x_{\mathrm{i}}, y_{\mathrm{i}})$	$1 + f(x_{\mathrm{i}}, y_{\mathrm{i}})$	$1 + \mathrm{i}f(x_{\mathrm{i}}, y_{\mathrm{i}})$
$\tilde{U}_{\mathrm{i}}(-u, -v)$	$\delta(u, v) + \tilde{f}(u, v)$	$\delta(u, v) + \mathrm{i}\tilde{f}(u, v)$
$U_{\mathrm{o}}(x, y)$	$1 + f(x, y)$	$1 + \mathrm{i}f(x, y)$
$I_{\mathrm{o}}(x, y)$	$1 + 2f(x, y)$	1
$H(u, v)\tilde{U}_{\mathrm{i}}(-u, -v)$	$\mathrm{i}\delta(u, v) + \tilde{f}(u, v)$	$\mathrm{i}\delta(u, v) + \mathrm{i}\tilde{f}(u, v)$
$U_{\mathrm{o}}(x, y)$	$\mathrm{i} + f(x, y)$	$\mathrm{i} + \mathrm{i}f(x, y)$
$I_{\mathrm{o}}(x, y)$	1	$1 + 2f(x, y)$

amplitude object, the intensity is $I_{\mathrm{o}}(x, y) \approx 1+2f(x, y)$ and for the phase object $I_{\mathrm{o}}(x, y) \approx 1$, where the terms in $f^2(x, y)$ have been discarded to be consistent with the approximation of Equation 2.25. The image of a small amplitude object is a linear mapping of the object. The image of a small phase object presents no contrast.

This description sets the stage for the phase contrast method of Zernike. A phase plate is placed in the exit pupil to shift the direct light by $\pi/2$ with respect to the diffracted light. The pupil function $H(u, v)$ is

$$H(u, v) = \begin{cases} \mathrm{i} & \text{for } u = v = 0, \\ 1 & \text{for } u \neq 0 \text{ and } v \neq 0. \end{cases} \tag{2.26}$$

The lower part of Table 2.1 shows the light distribution in the output pupil plane after spatial filtering, the output wave $U_{\mathrm{o}}(x, y)$, and the corresponding intensity $I_{\mathrm{o}}(x, y)$. With the phase plate, the image of a small phase object is $I_{\mathrm{o}}(x, y) \approx 1+2f(x, y)$. That is, the image of a small phase object is identical to the image of an amplitude object obtained without phase plate. By introducing a phase plate that shifts the direct light by $3\pi/2$, the image of a small phase object become $I_{\mathrm{op}}(x, y) = 1 - 2f(x, y)$. This image is sometimes called negative contrast. It is notable that the image of a small amplitude object presents no contrast, when terms in the square of f are neglected.

This duality between amplitude and phase was used by Mogensen and Glückstad to synthesize a wavefront with a desired phase from an amplitude distribution [172]. Noda and Kawata obtained both the am-

plitude and the phase from three images, one without phase plate, one with positive contrast, and one with negative contrast [173].

Zernike also discussed the effect of a phase plate with an absorbing phase-shifting area [168]. The pupil function is

$$H(u,v) = \begin{cases} \mathrm{i}\mathcal{T} & \text{for } u = v = 0, \\ 1 & \text{for } u \neq 0 \text{ and } v \neq 0, \end{cases} \tag{2.27}$$

where $\mathcal{T}$ is the transmittance of the phase-shifting area, a real number between 0 and 1. The image is then $I_\mathrm{o}(x,y) \approx \mathcal{T}^2 + 2\mathcal{T} f(x,y)$, and the contrast $\mathcal{V}$ is increased by a factor $1/\mathcal{T}$. The construction of many systems with different phase plates have been presented [174]. Using the polarisation of light and a polarising phase plate, Osterberg proposed a very versatile system that allows the phase and the amplitude of the phase plate to be varied [175].

Diffraction effects and practical issues

So far, it was assumed that all the direct light and none of the diffracted light passes through the phase-shifting area of the phase plate. In practice, however, this area has a finite dimension and the spatial frequency spectrum of the object is blurred due to the finite extent of the input wave. The effect of the phase plate and of the limited input beam diameter was addressed by Zernike in his first papers [156, 167].

In the absence of the object or for a constant object, the light distribution in the exit pupil P of the system is the Fraunhofer diffraction pattern of the incoming beam. Ignoring the phase factor associated with the converging wave at P, this pattern is given by the Hankel transform of zero order [145],

$$U_\mathrm{p}(w) = 2\pi \int_0^a J_0(2\pi r w) r \,\mathrm{d}r = \pi a^2 \frac{2\,J_1(2\pi a w)}{2\pi a w}, \tag{2.28}$$

where a is the beam radius, $r = \sqrt{x^2 + y^2}$ is the radial coordinate in the object plane, and $w = 1/r$ is the radial spatial frequency in the *object* plane. This is the well known result first derived by Airy.

The light distribution in the image plane O', for a magnification

$M = 1$, is the Fourier transform of $U_{\mathrm{p}}(w)$ multiplied by the phase plate,

$$\begin{aligned} U_{\mathrm{o}}(r) = \quad & 2\pi \int_0^{w_{\mathrm{b}}} \pi a^2 \frac{2\,J_1(2\pi a w)}{2\pi a w} \exp\left(\mathrm{i}\frac{\pi}{2}\right) J_0(2\pi r w) w \,\mathrm{d}w \\ & + 2\pi \int_{w_{\mathrm{b}}}^{\infty} \pi a^2 \frac{2\,J_1(2\pi a w)}{2\pi a w}\, J_0(2\pi r w) w \,\mathrm{d}w, \end{aligned} \tag{2.29}$$

where w_{b} is the radius of the phase-shifting area. Equation 2.29 can be written as

$$\begin{aligned} U_{\mathrm{o}}(r) = \quad & 2\pi \int_0^{\infty} \pi a^2 \frac{2\,J_1(2\pi a w)}{2\pi a w}\, J_0(2\pi r w) w \,\mathrm{d}w \\ & + 2\pi(\mathrm{i}-1) \int_0^{w_{\mathrm{b}}} \pi a^2 \frac{2\,J_1(2\pi a w)}{2\pi a w}\, J_0(2\pi r w) w \,\mathrm{d}w. \end{aligned} \tag{2.30}$$

The first term is the *perfect* image of the input beam, that is, 1 within the radius a and 0 outside. The second term is the deviation from the perfect image due to the presence of the phase plate. The solution of the definite integral of the second term $D(r')$ was derived by Zernike. He used the normalised radial coordinate $\rho = 2\pi a w$, the normalised radius $r' = r/a$, and the radius b of the phase-shifting area in optical unit. By change of variables,

$$D(r') = \int_0^b J_1(\rho)\, J_0(r'\rho)\,\mathrm{d}\rho. \tag{2.31}$$

Zernike obtained

$$\begin{aligned} D(r') = \quad & [1 - J_0(b)]\ 2\ \frac{J_1(br')}{br'} \\ & + [1 - J_0(b) - 2\,J_2(b)]\ 6\ \frac{J_3(br')}{br'} \\ & + [1 - J_0(b) - 2\,J_2(b) - 2\,J_4(b)]\ 10\ \frac{J_5(br')}{br'} + \ldots \end{aligned} \tag{2.32}$$

This result is derived in Appendix A, following Zernike's paper [167]. The image intensity [167] is

$$I(r') = \begin{cases} D^2(r') + [1 - D(r')]^2 & \text{for } r' \le 1, \\ 2D^2(r') & \text{for } r' > 1. \end{cases} \tag{2.33}$$

A plot of $I(r')$ is shown in Fig. 2.9, for phase-shifting areas with radii b equals to 2.0, 2.5, 3.8, and 5.5 o.u. When the diffraction effect of the phase plate is taken into account, the phase contrast method of Zernike

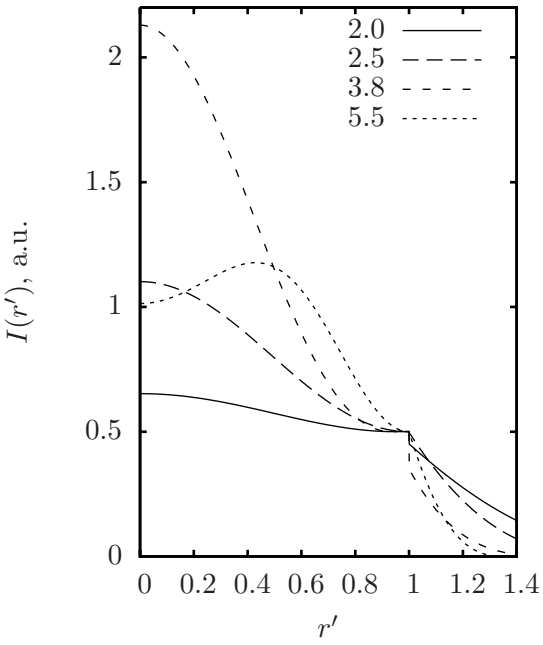

Fig. 2.9. Intensity variation in the image due to the presence of the phase plate with different radius of the phase-shifting area, given in optical unit.

is not linear. This non-linearity can be attenuated by slightly changing the plane of focus, as shown by Linfoot [176].

This non-linearity is due to the part of the direct light that passes outside of the phase-shifting area of the phase plate. Another effect is due to the diffracted light that passes inside this area. The importance of these effects depends on the task being accomplished. In optical shop testing, the task is to measure low order aberrations of generally small amplitude. For this task, the non-linearity of the method introduces a non-negligible error. Furthermore, the spatial frequency spectrum of such object is concentrated close to the phase-shifting area. Part of the diffracted light may passe through this area and its contribution to the contrast is lost. In addition, a small misalignment, i.e., the presence of a non zero mean tip or tilt, may have a large effect on the image. In microscopy, the task is generally to detect the presence of an object. For this task, the non-linearity of the method are not critical. The spectrum of small objects spread over a large region in the exit pupil. The radius of the phase-shifting area may be large and small misalignments are not critical. For these reasons, the method is well suited for microscopic

imaging.

In general the method works when the direct light, the reference wave, is strong relative to the diffracted light. It fails when the object diffracts all the light. It fails when a strong phase object covers most of the object field. When the strong phase variations are localised in a small area of the object field, however, a large portion of the direct light passes through the phase-shifting area, the reference wave is strong and the object is visible. The intensity is not linearly related to the phase, but for a detection task, the method works just fine.

The question of the optimum phase plate in term of absorption, phase shift, and radius for different object has been studied [177, 178]. In general, for a strong phase object $\phi \approx 2\pi$, the optimum phase shift is π [177]. In Section 3.1, the optical path length difference introduced by a single layer of ganglion cells is approximated. A value of $0.2\,\mu$m is found, which corresponds to a phase difference of $2\pi/3$ at a wavelength of 600 nm.

3

Imaging retinal phase structures

Having reviewed the progress accomplished in retinal imaging and having described the phase and techniques to access it, I now discuss the possibility of using a phase sensitive technique to obtain image of the retina. I start with a description of the retina as a phase object. I continue with a discussion of the applicability of the imaging techniques currently used in ophthalmology, mainly confocal scanning laser ophthalmoscope and optical coherence tomography, to image the retinal phase structures. Then I describe another approach to phase imaging of the retina, the study of which is the subject of Chapters 4 and 5.

3.1 The retina as a phase object

The retina lies on the inner-side of the posterior pole of the eye. It is observed through the optics of the eye, which acts as a microscope objective. The aperture of this objective is limited by the iris. After dilatation with cycloplegic drug, its diameter reaches 6 to 8 mm and its numerical aperture (NA) reaches 0.17 to 0.23, using 17 mm for the eye's equivalent focal length in air. The ocular media is mostly transparent in the wavelength range from 0.45 to 1.15 μm, enabling fundus observation [179,180]. Some peculiarities of the retina that stem from its nature and its location are now discussed.

Safe exposure to light

Exposure to light may be hazardous to living tissues by: energy transfer, thermal effects; the production of toxic chemical compounds, photochemical effects, and; direct ionisation, non-linear effects. The retina is located at the back focal plane of the optics of the eye. It is vulnerable to irradiation from a collimated beam of light incident on the cornea. For a collimated beam filling a 7 mm diameter pupil, the irradiance at the retina is in the order of 2×10^5 times the irradiance at the cornea [181]. Following the development of the laser, several agencies have published standards concerned with safety. These standards cite the maximum exposure considered to be safe under different viewing conditions [181–183]. The bottom line is, that for safety reasons, there is a maximum exposure that can be used for retinal imaging in human subjects. The safety issues concerning the exposure to light applicable to this work are discussed in Appendix B.

Acquisition time

A sharp image of the retina is obtained only if the retina remains stationary relative to the acquisition system and if the optical properties of the eye do not vary during the image acquisition period. The eye is in continuous motion and the optical properties of the eye vary with time. The retina follows the eye in its different motions:

- The eye moves with the head.
- The eye is rotated and shifted by the action of six extraocular muscles that aim the image at the fovea [15].
- The eye follows three movement patterns important for vision [184] that are not consciously controlled by the subject:
  - Slow drifts, with angular velocity smaller than 30 arcmin s^{-1};
  - Microsaccades, which occurs at a rate of 1 to 2 Hz with an amplitude ranging from 10 to 120 arcmin;
  - Tremor, which is an aperiodic motion with mean frequency at about 90 Hz and an amplitude smaller than 0.2 arcmin.
- The eye pulsates following the cardiac cycle. The eye globe expands by 3 to 6 μm [185] and the eye moves forward and backward by about 40 μm [186, 187].

The optics of the eye is continuously changing.

- The optical power—the accommodation—varies by up to a quarter of a dioptre at a frequency of about 2 Hz [188].
- The tear film covering the cornea slowly evaporates. It is re-established by blinks. In the pathological condition known as dry eye, the visual acuity is decreased [189, 190]. The role of the tear film in vision and the time evolution of the tear film are a new research area [191, 192].
- Ocular aberrations of all orders fluctuate in time with a temporal spectrum extending up to about 30 Hz [73, 79].

Different actions are taken to minimise the effect of the eye motions and the effect of the changes in the optical system. The use of a chin-and-head rest or of a dental impression (bite-bar) greatly reduces the movements of the head. By asking the subject to fixate at a target, the movements of the eye are decreased [193]. The fluctuations in accommodation may be temporarily blocked with drugs. The tear film is maintained by asking the subject to blink regularly, once every few seconds. Two approaches are taken to avoid the remaining variations.

The first approach is to 'freeze' the image by using a very short acquisition period. Riggs *et al.* published the typical excursion of retinal image during varying time periods [194]. These authors state that an exposure of 10 ms nearly always results in a 'stopped' retinal image. The same figure was obtained recently by Rha *et al.* [76]. When, for safety reasons, the signal from a single short exposure is too small, an image may be obtained from a series of co-registered frames (see for example [112]).

The second approach is to actively compensate for these fluctuations. This is the idea behind image stabilisation, tracking, and adaptive optics. Image stabilisation was introduced to study vision [195]. An automatic stabilisation is obtained using an optical path folded in such a way to be influenced twice by the eye motions in opposite direction [195] or using a system with an optical path insensitive to eye motions [196]. Tracking is obtained by an active control of the acquisition system to compensate for any measured displacements. In a confocal scanning laser ophthalmoscope, lateral displacements were corrected to within 3 arcmin [197]. In an optical coherence tomography system, longitudinal displacements

were corrected to within 25 μm [187]. In adaptive optics, the ocular aberrations are measured and corrected in real time [1]. After correction, the measured wavefront variance is close to the variance expected for a diffraction limited optical system.

To obtain a sharp image of the retina a short acquisition time may be used. The use of a long acquisition time and an active compensation of all the eye motions and optical variations, as for now, falls short of the accuracy required for high resolution imaging, about 0.2 arcmin laterally and a few micrometres longitudinally.

The pathways of light returning from the fundus

The light returning from the fundus has followed different paths through the tissue. Part of the light is reflected at the inner limiting membrane. This part did not enter the retina. Part of the light is diffused back from the choroid. This part passed twice through the full retina (see figures 1.3 and 1.4). The light interaction with the fundus has been studied *in vivo* by analysing the temporal spectrum [198–201], the directionality [32, 199–201], and the polarisation [32, 33] of the light returning from the fundus. Using prior knowledge from the anatomy (see Chapter 1) and the absorption spectrum of the major pigments present in the eye fundus (see Fig. 3.1, top), different models have been proposed [202]. The spectral data is now described.

A qualitative analysis of the measured reflectance spectra and a comparison with the absorption spectra of the different pigments gives some hints on the different contributions to the light returning from the fundus. The bottom part of Fig. 3.1 shows seven spectra obtained by Delori and Pflibsen for a 5°-area centred at the *foveola* of the eye of seven subjects with different choroidal melanin density. These subjects were described as: Caucasian blue eye (number 1 to 3); Caucasian brown eye (number 7 and 8); Afro-American (number 9 and 10) [198]. These spectra show three distinct parts.

Below 520 nm. This part of the spectrum is not directly described by Delori and Pflibsen. These authors, however, describe the presence of the macular pigment in relation to their model. It is plausible that the inter-individual variability of this part of the reflectance spectrum reveals the density of the macular pigment, which depends on the diet of the subject.

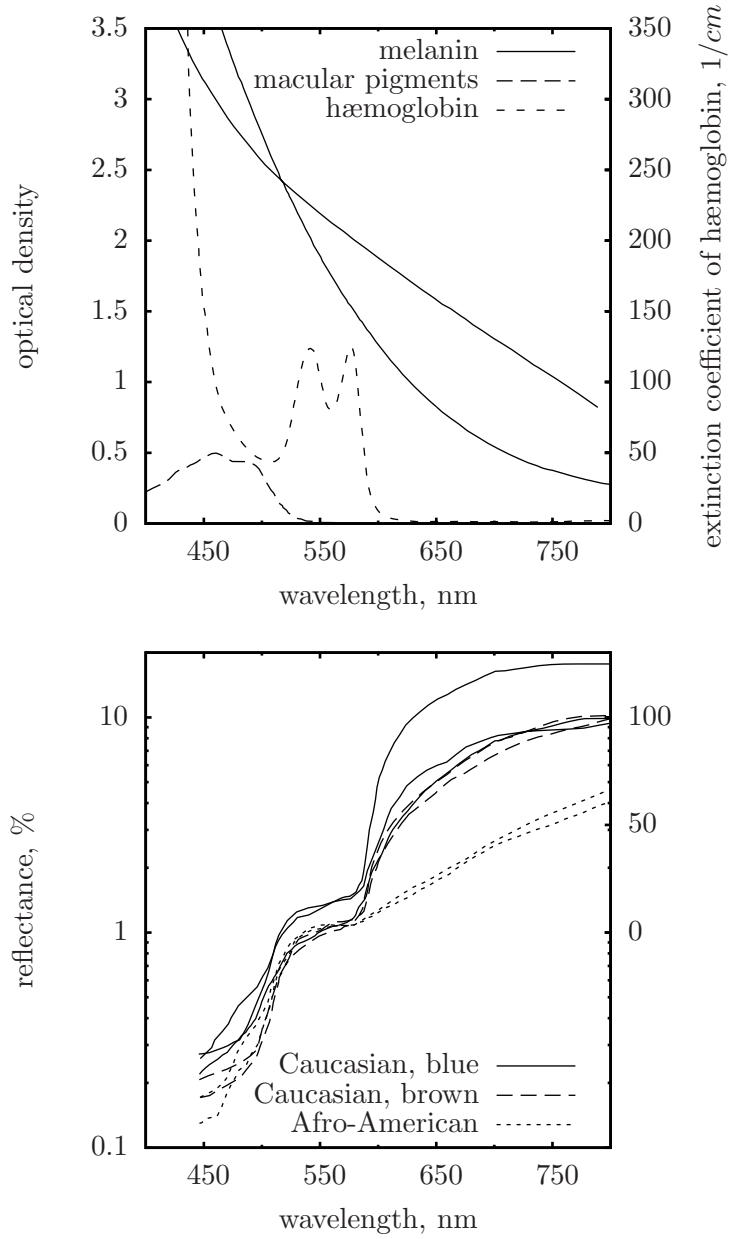

Fig. 3.1. (Top) absorption spectra of the melanin, the macular pigment, and the hæmoglobin. For the melanin, two curves that represent the extremes in the wavelength dependence are shown. The extinction coefficient of hæmoglobin at 95 % of oxygen saturation is shown on the right. This is the saturation level of blood in the choroid. (Bottom) Reflectance spectra obtained from the fovea of seven subjects with different amount of melanin concentration. The two graphs are adapted from Delori and Pflibsen [198].

Above 600 nm. Lightly pigmented eyes have a greater reflectance than darkly pigmented eyes in this part of the spectrum. Furthermore, for lightly pigmented eyes, there is a marked change in reflectance from 570 to 610 nm. This change reflects the rapid drop of absorption by the hæmoglobin pigment of the choroidal circulation for longer wavelengths. In this spectral range, a significant fraction of the light returning from the eye fundus has penetrated to the choroid.

From 520 to 600 nm. In this range, the absence of the double peak absorption signature from the hæmoglobin pigment and the absence of clear ordering of the spectra in function of choroidal melanin concentration indicates that the contribution from the choroid is small. The variability may be explained by different amount of melanin concentration within the cells of the retinal pigment epithelium (RPE). This concentration is independent of the choroidal melanin concentration [203].

The amount of light returning from the choroid in the middle spectral range appears to be much smaller than the contribution from the photoreceptor segment or RPE in the image taken with the retinal thickness analyser [84]. Direct measurement in donor's eyes, however, has shown that 5 to 10 % of the light at 550 nm is transmitted through both the RPE and the choroid [23].

In vivo measurements of the inner limiting membrane (ILM) reflectance and nerve fibre layer scattering have been obtained in the monkey eye [204]. The reflectance from the ILM is directional. Its magnitude is in the order of 0.3 % after correction for the ocular media absorption. This reflection is independent of the wavelength of the light, which is consistent with a Fresnel reflection. The scattering from the nerve fibre layer arcane—the thickest part of this layer—is about 1 % at 500 nm and about 0.8 % from 550 to 670 nm. Away from the arcane, this layer is thin and its reflectance is small. At the *foveola*, the nerve fibre layer is absent.

The light reflected by the photoreceptors is preferentially directed toward a point near the centre of the pupil. This directionality is called the optical Stiles–Crawford effect (see for example [32, 33]). The light distribution in the exit pupil of the eye is measured for different position of a small input beam in the input pupil. When the input beam is centred on the maximum of the Stiles–Crawford effect, the light distribution at the exit pupil has a Gaussian shape superposed on a con-

stant term. The Gaussian part is due to directional reflections by the photoreceptor segments. Its width and its magnitude depend on the eccentricity of the probed area of the retina or equivalently the size of the cone photoreceptors [205, 206], on the amount of visual pigment present (bleaching) [32, 33], on the wavelength [201, 207], and on the state of polarisation [33]. The constant part is thought to come from light scattered from the RPE, the choroid, and the sclera [200].

By measuring the reflectance spectrum of the eye for an incoming beam centred on the Stiles–Crawford effect or away from the centre of the Stiles–Crawford effect, van de Kraats *et al.* have shown that the reflected light from the photoreceptor segments is constant at about 1 % over the wavelength range from 550 to 750 nm [200, 201], while the total reflectance increases from 1 to 5 %. This is a strong evidence that the light returning from the layers located behind the photoreceptors is not guided towards the pupil.* Furthermore the light that fluoresces from the lipofuscin granules located within the RPE is not guided by the photoreceptors [208]. Accordingly, the contrast of the image of the cone photoreceptor mosaic obtained at different wavelengths using an adaptive optics system is expected to decrease with wavelength. However, it was found by Choi *et al.* that the contrast is fairly constant over wavelengths ranging from 550 to 750 nm [207].

The diffuse part of the light distribution at the pupil was shown to be non-polarised using a probing beam at a wavelength of 543 nm [33], which is consistent with light being multiply scattered within the tissue. However, this does not agree with the result of van Blokland and van Norren, who have shown that the light returning from the fundus preserves the polarisation of the input beam at more than 70 % over the whole pupil and at wavelength shorter than 568 nm [32].

Recently, a more direct measurement of the contribution of the different layers of the fundus to the reflectance spectra has been measured using an optical coherence tomography (OCT) system [209]. The signal of an OCT system represents only a part of the light returning to the

*The formulation used in the literature—coupled or not coupled; guided or not guided—is in my opinion rather misleading. We observe that part of the reflected light has a directional component when we illuminate the retina with a beam with a small distribution of angle centred on the Stiles–Crawford effect. When light is back scattered from deeper tissues, it reaches the photoreceptors with a very large distribution of angle, which hides the directional component. This is the same effect as in the forward direction when the illumination light fills the dilated pupil, the directional component is difficult to observe.

detector. The part that has a high degree of coherence with the reference beam and that has the same polarisation orientation (coherent detection). Figure 3.2 (top) shows an average of 510 scans obtained by Gao *et al.* [209]. From this data, the cumulative fraction of light returning to the pupil as a function of axial distance was computed (Fig. 3.2, bottom). About 15 % of the reflected light comes from the layers anterior to the photoreceptor inner segments. There is a significant part returning from the boundary between the photoreceptor inner segments and outer segments, from the photoreceptor outer segment, and from the RPE. The contribution from the choroid is small because OCT is insensitive to multiply scattered light. It is not possible to know the total amount of reflected light at each layer from OCT measurements because only the coherent part is recorded.

To summarise, the spectrum of the light returning from the fundus of the eye seems to be well understood, but the proportion of light returning from the different layers is uncertain. These proportions depend on the local level of pigmentation present. The largest uncertainty seems to be on the way light is transmitted through the photoreceptors and through the RPE.

Expected magnitude of the retinal phase structures

The magnitude of the phase variations of light transmitted through the retina is not known. However, the phase induced by a single cell was reported (not for retinal cells) or an approximation of this phase can be obtained from published values of cell size and refractive indexes.

Measurements. From interferometric measurements performed at a wavelength of 633 nm Beuthan *et al.* obtained a maximum phase shift of 1.4 μm relative to vacuum for an L 929 fibroblast cell from the liver [210]. The mean refractive index of these cells is about 1.38. Therefore, if the surrounding medium had had a refractive index of 1.33, the phase shift would have been $(1.38-1)/(1.38-1.33) = 7.4$ times smaller or 0.185 μm. These authors comment that the features visible in the phase image are the nucleus and the membranes. Using a phase-sensitive optical coherence tomography, Rylander *et al.* have shown images of human epithelial cheek cells [211]. From the scale of their figure, the single pass phase shift variation across a cell is about 0.2 μm.

Computation. The physical dimensions of many cells are available

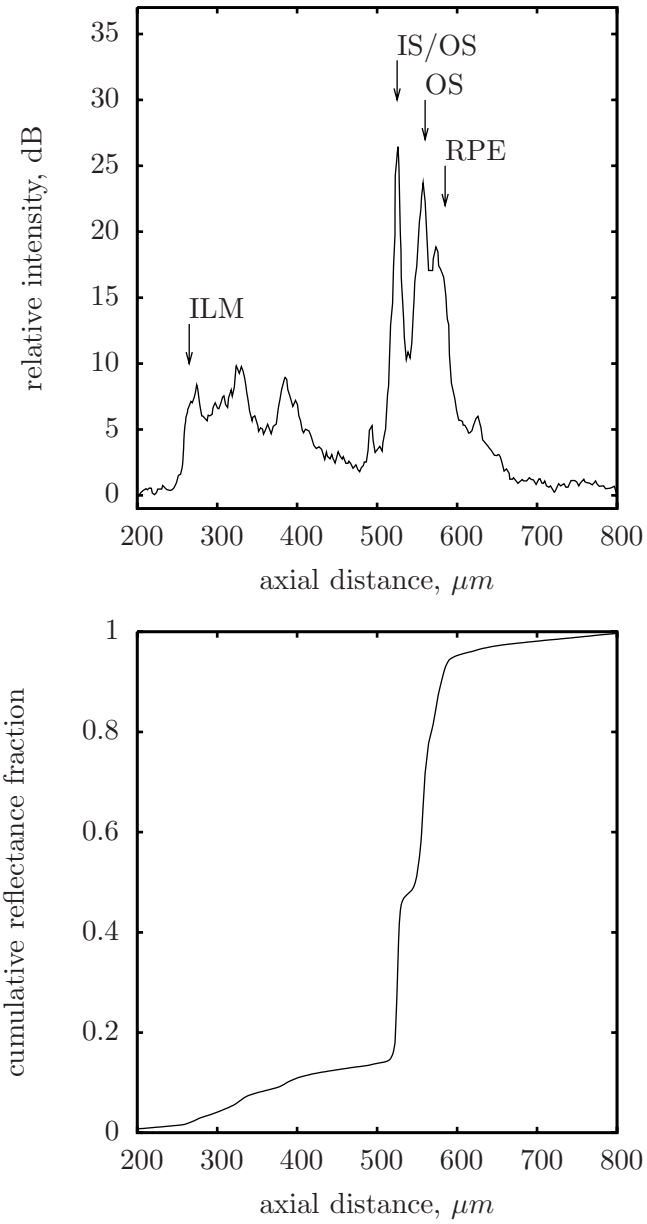

Fig. 3.2. (Top) Average of 510 optical coherence tomography scans redrawn from Gao *et al.* [209]. (Bottom) Cumulative reflectance fraction computed from the data on top assuming that the relative intensity is given by $10\log(I)$, where I is the measured intensity signal. This is the fraction of light returning from the fundus with the same polarisation as the probing beam and that is gated by the coherence length of the system.

in the literature [13]. The refractive index values, however, are difficult to find. The reason for this lack of data is two-fold. The living cell reacts to changes in its environment and the refractive index varies accordingly [24]. There is a large variation of the refractive indexes of the different cell components within a given population [212]. An approximation of the optical path difference induced by a cell can nevertheless be obtained. The neural cells of the retina are closely spaced (see Fig. 1.3) and therefore the principal phase structure is probably due to the difference between the refractive index of the nucleus and the refractive index of the cytoplasm—which is mainly the liquid of the cell body and small membrane components. From the Chinese hamster HeLa cells, the refractive index of the nucleus is about 1.39 and the refractive index of the cytoplasm is about 1.37 [212]. The ganglion cells have a nucleus with a diameter of 8 to 9 μm [13]. The optical path length difference induced by a single ganglion cell nucleus is, using Equation 2.6, $(1.39 - 1.37)9 = 0.18\,\mu$m.

The effect of a single layer array of ganglion cell on the image of photoreceptors or on visual perception at an eccentricity of a few degrees may be estimated using the diffraction efficiency η of a sinusoidal phase grating

$$\eta = J_q^2\left(\frac{m}{2}\right), \tag{3.1}$$

where J_q is the Bessel function of order q, q is the diffraction order, and m is the phase modulation in radians [60].

A row of ganglion cell nuclei will add an optical path difference following the absolute value of a sinusoidal function (see Fig. 3.3). Its strongest component has a magnitude equal to half the optical path length difference, about $0.2/2 = 0.1\,\mu$m [145], which corresponds to a phase of $\pi/3$ rad at a wavelength of $0.6\,\mu$m. The normalised magnitude (object absent) of the zero order of diffraction is 0.870 and that of the first order of diffraction is 0.064. Therefore, this approximation is consistent with the clear images of the photoreceptors obtained using adaptive optics. However, only a single layer of cells was considered. At a few degrees of eccentricity, there are 5 or 6 layers of ganglion cell bodies. To work out the effect of such a complicated phase object—inhomogeneous object—on photoreceptor imaging could be the subject of another thesis. If the phase modulation doubles then the normalised magnitudes become 0.55 and 0.21 for the zero and first orders, respectively. The

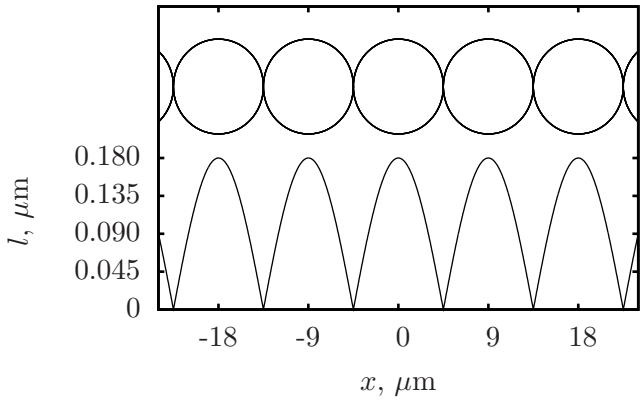

Fig. 3.3. (Top) single row of ganglion cell nuclei with a diameter of 9 μm and a difference of refractive index between the nucleus and the surrounding medium of 0.02, (bottom) the corresponding optical path difference, the absolute value of a cosine function.

diffracted light becomes important.

It is difficult to estimate the magnitude of the phase structures of the retina. All the figures given in this section are approximations using a very simple model of the neural tissue. The real refractive index distribution for a single cell or its components probably varies in an irregular manner as shown by Choi *et al.* for a HeLa cell [213]. For a single row of cells, however, the optical path variation is approximately 0.2 μm.

3.2 Different approaches to phase imaging of the retina

The description of the retina leaves rooms for different approaches to image its phase structures. These approaches can be classified according to the path followed by the light. The first uses the light reflected by the object of interest. The second uses the light reflected by the layers of the fundus located behind the inner retina. This light illuminates in transmission the object of interest.

Direct reflection

The amount of light reflected from the neural tissue of the inner retina is much less than the light returning from the deeper layers of the fundus. To discriminate between the light directly reflected from the neural tissue

and the light returning from the deep layers of the fundus, a technique with depth resolution is needed. In Chapter 1, three different depth resolved imaging techniques are described.

Zeimer's method. In this technique, the fundus of the eye is illuminated and observed through two different pupils forming the largest angle possible from the object [27]. As these pupils are within the pupil of the eye, their size and separation are limited. A direct consequence is that the high spatial resolution achieved with adaptive optics is not possible with this method.

Confocal scanning laser ophthalmoscope. Different phase sensitive techniques can be implemented using the confocal scanning laser ophthalmoscope (SLO) geometry. These include the phase contrast method of Zernike [214], optical differentiation [214,215], and differential interference contrast [216].

A confocal SLO with adaptive optics correction of the ocular aberrations approaches the theoretical resolution limit according to Rayleigh. The radius of the first zero of the Airy pattern is

$$r_{\min} = 0.61\lambda \, \frac{z}{a}, \tag{3.2}$$

where λ is the wavelength, z is the propagation distance, and a the radius of the aperture. For a pupil diameter of 6 mm, a wavelength of 550 nm, and a propagation distance of 17 mm, $r_{\min} = 1.9\,\mu$m. This resolution limit is adequate to image the nuclei of all the neural cells and the large phase structures of the retina.

Another important property is the rejection of the light contributions from out-of-focus planes, i.e., the light returning from the deep layer of the fundus. For contributions returning from a large distance—a distance larger than the defocus corresponding to Rayleigh's quarter-wave rule—the pinhole blocks most of the light. The fraction of light detected is the ratio between the area of the pinhole and the area, in the pinhole plane, illuminated by the out-of-focus contribution. Assuming a flat reflector at a distance d, the radius of the illuminated area is given by $2d\,a/z$, where a/z is the beam converging angle (see Fig. 3.4). The fraction of detected light for a pinhole radius equals to $r_{\min}$ is $0.305^2\lambda^2 z^4/(d^2a^4)$. For $d = 200\,\mu$m, this fraction is $7{\times}10^{-4}$. As

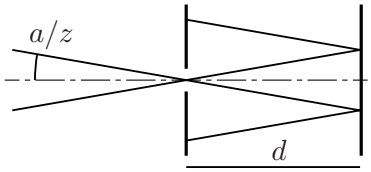

Fig. 3.4. Geometry for the calculation of the out-of-focus light rejection by the pinhole. a/z is the incident angle from the pupil radius a and pupil distance z, and d is the defocus distance of the reflected contribution.

the fraction of light directly reflected by the neural cells is unknown, it is difficult to predict whether this depth discrimination is sufficient.

From the graph shown in Fig. 3.2, the light returning from a 18 μm thick layer—the depth-of-field based on Rayleigh's quarter-wave rule—at the level of the ganglion cell nuclei corresponds to about 1 % of the total coherent and polarisation maintained light returning from the fundus. As discussed above, this is certainly a gross under estimation of the total light returning from the fundus. If, to simplify, the other 99 % returns from a reflector located at $d = 200\,\mu$m, then the signal to noise in the image could be about 10.

The reduction factor of $7{\times}10^{-4}$ was calculated for a pinhole with a radius equals to $r_{\min}$. Apparently, it is rather usual to use pinholes with larger radius. Romero-Borja *et al.* use pinholes with radius at least 2 times larger than $r_{\min}$ [93]. Burns *et al.* use pinhole with different radius depending on the object they want to image. Most of the images presented, however, were acquired with a pinhole radius equals to 2.6 times $r_{\min}$ [217]. Using a pinhole radius equals to 2 and 2.6 times $r_{\min}$ results in an increase in the detected fraction of light returning from the deep layers, and a corresponding decrease of the signal to noise ratio, by a factor of 4 and 6.8 compared with a pinhole radius equals to $r_{\min}$.

These approximations indicate that the signal level in retinal imaging using the light directly back reflected by the retina is small. The values given are only 'indicative' because they are based on uncertain approximations. Recently, confocal SLO images of cellular structures in the nerve fibre layer have been presented [98].

Optical coherence tomography. The phase of the optical coherence tomography (OCT) signal can be measured directly, enabling phase

sensitive imaging. However, as OCT is based on a separate-path interferometer, the measured signal is very sensitive to axial movements of the object. This difficulty slowed the development of phase sensitive OCT. It is through the development of techniques to measure the velocity of blood in retinal vessels that progress has been made.

At first, the reference arm was stopped and the interference signal was recorded [218]. A frequency analysis of this signal reveals the frequency shift—the Doppler effect—induced by the moving cells crossing the coherence volume. Doppler OCT imaging was obtained from vessels of the human retina by Yazdanfar *et al.* [219]. The spectral resolution is inversely proportional to the integration time. For a point measurement, the integration time may be increased, but for imaging this solution is impracticable. This difficulty is avoided by measuring the phase difference between two consecutive scans and by computing the velocity from the known inter scan period. This technique was first presented using a time domain OCT [220] and later using a Fourier domain OCT [221]. Maps of the blood velocity have been successfully obtained from human retinal vessels [222, 223]. The noise of the measured phase depends on the signal to noise ratio and on the spatial overlap of the consecutive scans [224]. Assuming a total overlap of consecutive scans and a signal to noise ratio of 20 dB, the standard deviation of the phase difference is 0.1 rad or 5.7°. By assuming a total overlap of the scans it is assured that the signal is reflected by the same group of scatterers, only slightly displaced—nanometre range compared to the micrometre of the detection volume. By laterally scanning the beam between consecutive scans, the scattering volume partially changes and an additional phase dues to speckle is added.

For non-ophthalmic applications, a common-path phase sensitive OCT technique was presented by Sticker *et al.* [225]. It is an adaptation of OCT to the differential interference contrast. These authors obtained the image of a phase object through a scattering medium. The phase object, however, was a step height difference of a specular surface, and therefore the object did not introduce additional speckle [226].

Trans-illumination

The light returning from the deep layers of the fundus trans-illuminates the inner retina. The light path in the eye can be separated in two parts: The first pass through the inner retina, when the light entering

the eye is transmitted to the deep layers of the fundus; The second pass through the inner retina by the light returning from the deep layers of the fundus.

If we assume that the light returning from the deep layers has lost the phase information it acquired during the first pass, then the imaging geometry is similar to the geometry of a transmission microscope. The light returning from the deep layers illuminates a phase object—the cells of the inner retina—and the optics of the eye is used as an objective. The main difference between retinal imaging and a transmission microscope is that in retinal imaging the illumination light cannot be fully controlled as in a transmission microscope. The properties of this illumination are not well known and they change from subject to subject.

The development of the depth sensitive techniques, discussed above, is supported by a large number of researchers in different groups. For the trans-illumination geometry, the author is not aware of a single work being pursued. Two approaches, however, have some merits.

Propagation. When light with a high degree of coherence is scattered by a rough surface, it produces speckles. This light may be used to retrieve phase information, such as in speckle interferometric techniques [128]. Therefore, the phase of the inner retina between two planes $\mathcal{A}$ and $\mathcal{B}$ may be computed from two intensity images obtained simultaneously, one conjugated with the plane $\mathcal{A}$ and the other with the plane $\mathcal{B}$. To obtain the phase, the propagation method of Teague may be used (see Section 2.4). Alternatively, the light from the fundus may be splitted and interference between the two beams can be obtained with one beam conjugated with the planes $\mathcal{A}$ and the other beam with $\mathcal{B}$.

Phase imaging. In Section 2.4, the phase sensitive techniques based on imaging were discussed for a plane wave illumination. Two departures from this ideal situation is met in practice.

- The source viewed from the object plane subtends a finite angle. The light from this source may be modelled as a group of waves, each coming from a different part of the source. That is, each wave has a different angle of incidence on the object.

- The waves may diverge or converge, which lead to a different axial position of the output pupil and a different transverse magnifi-

cation for the source image. This situation was discussed in a theoretical note by Hopkins [227].

The light distribution in the output pupil consists in the convolution of the spatial spectrum of the object with the image of the source. As long as the different components of the spectrum can be efficiently filtered, the phase sensitive techniques based on imaging should work.

In the eye, the light returning from the photoreceptors and the retinal pigment epithelium is scattered at large angle. To obtain a small image of the source, this diffusing layer is considered as a source—a secondary source—and the extent of this source is minimised. If a sufficiently small source is created on this layer, the phase sensitive techniques based on imaging can be used in the eye.

3.3 The aims of this work

The first aim of this work was to discuss the possibility of imaging the retina using a phase sensitive technique. This is done. The second part of this work aims at answering the following question:

> Is is possible to image the retina using a phase-sensitive imaging technique by using a point-source of light created at the surface of the diffusing layer of the eye fundus?

In particular, the adaptation of the phase contrast method of Zernike is studied. The other methods based on depth resolved techniques or on the propagation of light returning from the deep layers will not be discussed.

3.4 Secondary point source illumination

In this section, the differences between the conventional geometry for phase imaging described in Chapter 2 and the proposed geometry—using a small source at a finite distance—is highlighted. Then the application of this geometry to retinal imaging is discussed.

Phase imaging using a diverging point source

The geometry considered is shown in Fig. 3.5. A point source σ emits a spherical wave that illuminates the phase object O. The lens system

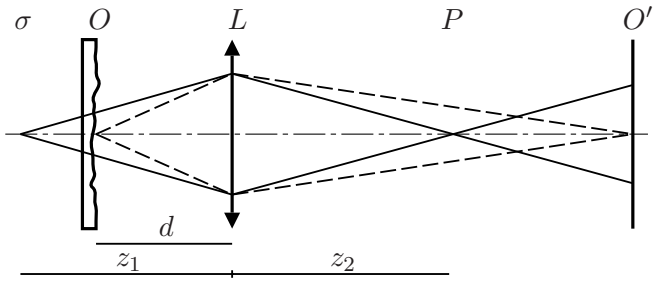

Fig. 3.5. Setup for imaging techniques. Light from a point source σ illuminates a phase object O and is brought into focus at the plane P. The light diffracted by the object is collected by the lens system L and focused on the image plane O'.

L conjugates the plane with the source σ to another plane marked P, the output pupil of the system. The lens system L also conjugates the object plane O to the image plane O'.

Ignoring the effect of the finite aperture of the lens system L, the wave in the output pupil plane P is obtained by following these four steps:

- Multiplication of the diverging wave from the source σ with the object transmittance—This is the input wave $U_{\mathrm{i}}(x)$;
- Free-space propagation from the object plane O to the lens system L—This is a Fresnel diffraction integral over a distance d;
- Phase transformation by the lens system L;
- Free-space propagation from the lens system L to the output pupil plane P, over a distance z_2.

Goodman [60] obtained a simple formula for the wave at the output pupil P (one-dimensional object). His result is sufficient for our discussion. The wave at P for a point source and a perfect optical system is described by

$$U_{\mathrm{G}}(\xi) = \frac{\exp\left[\mathrm{i}\frac{k}{2}\frac{(z_1+z_2)d-z_1z_2}{z_2^2(d-z_1)}\xi^2\right]}{\sqrt{\lambda\frac{z_2(z_1-d)}{z_1}}} \int_{-\infty}^{\infty} U_{\mathrm{i}}(x)\exp\left[-\mathrm{i}k\frac{z_1}{z_2(z_1-d)}\xi x\right]\mathrm{d}x, \tag{3.3}$$

which is the Fourier transform of the input wave $U_{\mathrm{i}}(x)$ evaluated at the spatial coordinate

$$\xi = \lambda\frac{z_2(z_1-d)}{z_1}u. \tag{3.4}$$

The quadratic phase factor reflects the fact that a wave coming from a point on the object O converges toward the plane O'. The absolute value of the second fraction of this term is equal to the distance from P to O',

$$\overline{PO'} = \left| \frac{z_2^2(d - z_1)}{(z_1 + z_2)d - z_1 z_2} \right|, \tag{3.5}$$

as it can be shown by applying the lens equation for z_1, z_2 and for $d, z_2 + \overline{PO'}$. The last term, the square root, has the proper form to conserve the energy.

By applying the thin lens equation, the fraction in Equation 3.4, which 'scales' the Fourier transform, can be written as

$$\frac{z_2(z_1 - d)}{z_1} = f\frac{z_1 - d}{z_1 - f}, \tag{3.6}$$

where f is the focal length of the system L, and where $z_1 > d > f$ (see Fig. 3.5). When $z_1 = \infty$, this fraction equals f. This result is consistent with plane wave illumination. When z_1 is finite, $\infty > z_1 > d$, this factor is smaller than f. Therefore, with a point source located at a finite distance, the extent of the Fourier transform is less than the extent of the Fourier transform obtained when the source is located at an infinite distance.

Both the optical system L and the source σ have an effect on the wave at the output pupil P. From linearity, the wave at P is the convolution of the 'perfect' wave $U_{\mathrm{G}}(\xi)$ with the image of the source σ' formed by the lens system L,

$$U_{\mathrm{P}}(\xi) = \int_{-\infty}^{\infty} U_{\mathrm{G}}(\xi_i)\sigma'(\xi - \xi_i)\,\mathrm{d}\xi_i. \tag{3.7}$$

The image of the source σ' is obtained from the convolution of the properly scaled source σ with the point-spread function of the system according to Equation 2.16. Equation 3.7 shows how the spatial spectrum of the object is blurred by the combined effect of the optical system L and of the extent of the source σ. When the convolution kernel σ' is large, the spectrum is blurred over a large area and spatial filtering is inefficient. When σ' is small, the spectrum is blurred over small area and spatial filtering is effective. The size of the source σ also affects the degree of coherence of the wave in the object plane. When the source σ is large, the degree of spatial coherence is small. That is, only small

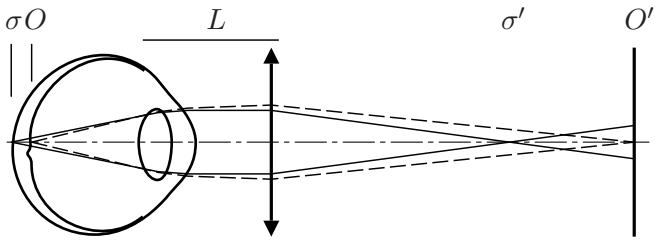

Fig. 3.6. Geometry for phase sensitive imaging using a point source of light σ on the photoreceptor outer segments and on the retinal pigment epithelium layer. In this drawing, the thickness of the ocular fundus is exaggerated.

features (high spatial frequencies) are coherently illuminated, and therefore can be imaged with phase sensitive techniques. When σ is small, the degree of spatial coherence is large. Large features are coherently illuminated, and may be imaged.

Application to retinal imaging

Using a simple model of the eye, it is found that, in principle, phase sensitive imaging techniques can be applied to image the retina. A drawing of the eye and of the optical setup is shown in Fig. 3.6. A point source σ is located on the photoreceptor segments and the retinal pigment epithelium layer. The light from this source propagates to a phase object O located in the inner retina. The optics of the eye and a positive lens forms an optical system L that conjugates the source plane with the output pupil P and the object plane with the image plane O'.

The dimension considered are the following:

- Pupil radius, $a = 3\,\text{mm}$, using adaptive optics;
- Equivalent focal length of the eye in air, $f = 17\,\text{mm}$;
- Source to object distance, $250\,\mu\text{m}$, equivalent in air;
- Object, array of ganglion cell nuclei with $9\,\mu\text{m}$ diameter modelled as a phase sinusoidal grating with a modulation of $\pi/3\,\text{rad}$ and spatial frequency $u_0 = 111\,\text{mm}^{-1}$;
- Wavelength, $\lambda = 550\,\text{nm}$.

The dimensions for the single lens equivalent system (see Fig. 3.5) are $z_1 = z_2 = 17.00\,\text{mm}$, $d = 16.75\,\text{mm}$, and $f = 8.5\,\text{mm}$. From Equation

3.1, the normalised magnitude of the zero and first order of diffraction are 0.870 and 0.064, respectively. The position of the first diffraction order in the output pupil is $15\,\mu$m (Equation 3.4). The image of a point source σ' is the Airy pattern with a first zero at a radius of $1.9\,\mu$m. The light distribution in the output pupil is shown in Fig. 3.7. At the top, the normalised wave $U_{\mathrm{P}}(\xi)$ is displayed, ignoring the quadratic phase factor in Equation 3.3. The first diffraction orders is seen as two small bumps at $\xi = \pm 15\,\mu$m. At the bottom, the corresponding intensity is plotted using a logarithm scale to reveal the diffracted light.

In Figure 3.7, the zero and the first orders of diffraction are spatially separated. A spatial filter can be used to block or to retard the different parts of the spectrum. Phase sensitive imaging techniques can be used for retinal imaging if a secondary source with lateral dimension smaller than about $11\,\mu$m can be created. This result was obtained for a point source and for free propagation from the source to the object. In Chapter 4, this illumination geometry is used *in vitro* to experiment with the effects of an extended source and of a thick phase object.

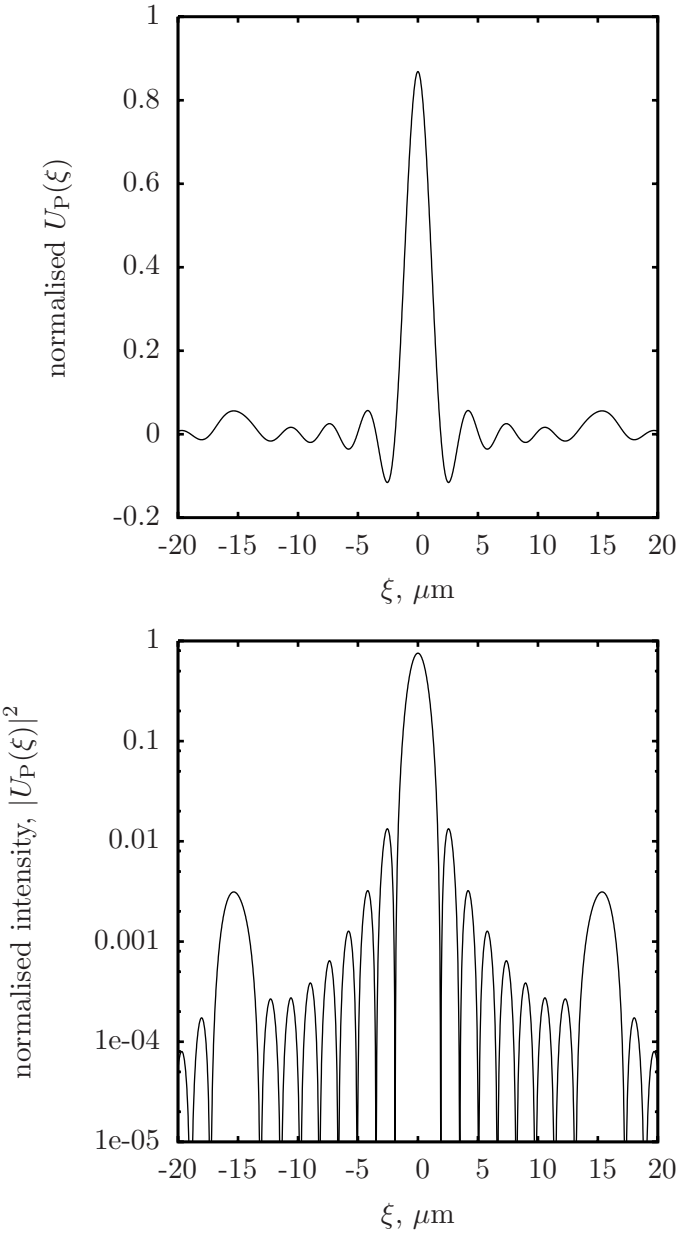

Fig. 3.7. Normalised wave amplitude in the output pupil for a sinusoidal phase grating corresponding to a single raw of ganglion cells. Top, normalised amplitude of the wave with respect to the wave obtained in the absence of the object. Bottom, normalised intensity plotted in logarithmic scale to reveal the diffracted light.

4

Experiments with *ex vivo* objects

In this chapter, the trans-illumination geometry discussed in Section 3.2 is used with the phase contrast method of Zernike to image phase objects. Using this illumination geometry, the source is at a finite distance from the object. In the first experiment, the effects of the distance between the source and the object are revealed. In the second experiment, phase contrast images of a glass object are obtained in reflection, in a geometry similar to the eye geometry. In the third experiment, phase contrast images of a thick phase object are obtained.

In microscopy, it is usual to introduce normalised coordinates or dimensionless optical units (o.u.) [214]. These coordinates are scaled against the diffraction pattern present in the diffraction limited microscope. For the axial length, the normalised coordinate u is defined for a plane wave incident on a circular aperture in the output pupil of an optical system.

$$u = ka^2 \left(\frac{1}{f} - \frac{1}{z} \right), \tag{4.1}$$

where k is the wave number, a the radius of the aperture, f the focal length of the system, and z the physical distance from the exit pupil to the observation plane.

For the dimensions considered in the simple eye model given in Section 3.4, the optical distance between the source and the object is -90 o.u. For the experimental conditions described in Chapter 5, $a = 3.35\,\text{mm}$ and $\lambda = 543\,\text{nm}$, this distance is -114 o.u. A normalised optical distance of about -100 o.u. is considered to be representative of

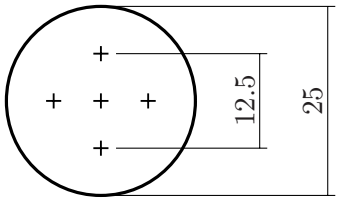

Fig. 4.1. The crosses indicate the location of the phase discs on the phase plate. Dimensions are in millimetres.

the geometry of an *in vivo* experiment with a human subject.

4.1 Finite source to object distance

In this experiment, a glass phase object is imaged using a transmission geometry with a light source at a finite distance. The phase plate and the phase object are described first, followed by the optical setup and the experimental results.

Phase plate

The phase plate consists of a set of five discs etched into a 3-mm thick optical window made of fused-silica, with a surface flatness of $\lambda/10$ at 633 nm over the 25 mm diameter. The location of the discs on the optical window is indicated in Fig. 4.1. The disc located at the centre of the phase plate has a radius $b = 10\,\mu$m. The radii of the four other discs are 20, 40, 80, and 160 μm. The depth of the etching is 350 nm. The refractive index* of the window at 675 nm is 1.456. The discs introduce an optical path difference of 160 nm, corresponding to a phase shift of 1.5 rad or 86°. This value is close to the desired phase shift of $\pi/2$ or 90°. At a wavelength of $\lambda = 543$ nm, the refractive index is 1.460, the optical path difference is 161 nm, and the phase shift is 1.86 rad or 107°.

As the discs are etched into the window, the phase shift advances the wave compared to the wave passing aside of the disc. This is a positive phase contrast. Notice that in the different drawings, the disc is represented with an added thickness, which produces a retarded wave.

*Data from the CVI Melles Griot catalogue.

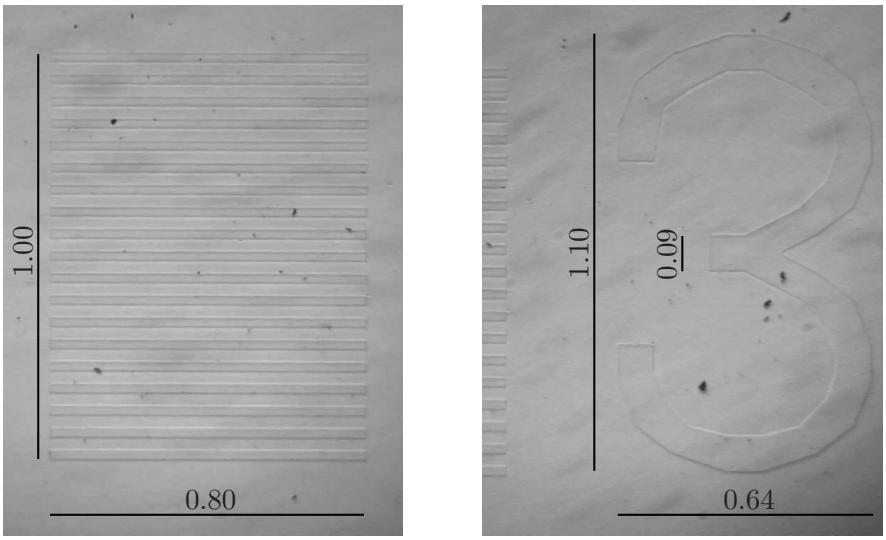

Fig. 4.2. Two features from the glass phase object observed with a transmission microscope using a 4× objective and a partially blocked illumination. On the left is a line grating and on the right is a number 3. The lengths of the markers are given in millimetres.

Phase objects

The phase objects are control marks located next to a Fresnel hologram etched into a glass-like material (probably fused silica or BK7) by Silios Technologies, France. One of these marks is a line grating, another one is a number 3. These two phase objects and their dimensions are shown in Fig. 4.2. For the line grating, the width of the etched lines is 26 μm and the separation between the lines is 30 μm. The first harmonic component of this grating has a spatial frequency of 17.86 mm^{-1}.

The depth of the object was measured with the Zygo interferometer from the National Centre for Laser Applications (NUIG). It is 120 $\pm$ 3 nm. Assuming a refractive index of 1.5 and using Equation 2.6, the optical path difference in transmission is approximately 60 nm, which corresponds to a phase shift of $\pi/5$ or 36°.

Optical setup

A drawing of the optical setup is shown in Fig. 4.3. A laser diode emitting at a wavelength $\lambda = 675$ nm is coupled into a single mode fibre, which tip is the source σ. The light from σ diverges and trans-

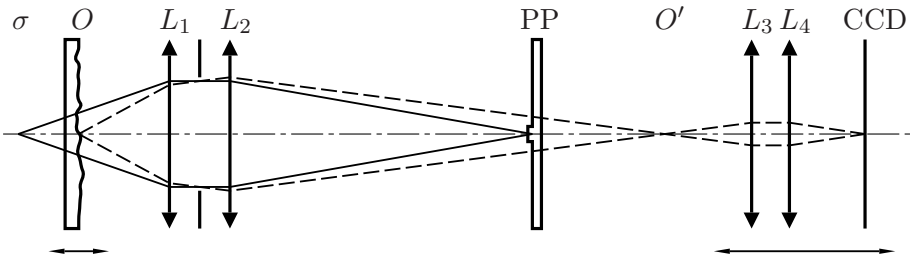

Fig. 4.3. Setup for phase contrast imaging with a source at a finite distance. The source σ is the tip of a single mode optical fibre. The phase object O is mounted on a translation stage. The lens system L_1 and L_2 images the source σ on the phase plate PP and the object O is imaged at O'. The axial position of O' depends on the position of O. A relay system L_3 and L_4 attached to a CCD camera is axially translated to image O' or the exit pupil.

illuminates the object O. The light passes through the lens system consisting in lenses L_1 and L_2, through the phase plate, through a second lens system (L_3 and L_4), to be detected by a charge coupled device (CCD) camera (Retiga EX, QImaging, USA). All the lenses are achromatic doublets with an infinite conjugate ratio. The lens L_1 has a focal length of 100 mm, the lens L_2, 250 mm, the lenses L_3 and L_4, 80 mm.

The source σ is located on the optical axis at the front focal length of the lens L_1. After L_1, the beam is collimated. A diaphragm with an aperture radius $a = 5.15$ mm limits the transmitted beam. The lens L_2 focuses the beam onto the phase plate PP. The diaphragm aperture is chosen such that the radius of the first zero of the diffraction pattern is equal to the radius of the phase-shifting disc of the phase plate, $b = 20\,\mu$m.

The object O is mounted on a translation stage allowing the source to object distance to be varied from 1.2 to 10.7 mm, or from -53 to -515 o.u. The position of the image O' changes as a function of the object position. The second lens system (L_3 and L_4) is a unit magnification relay attached to a CCD camera. The relay and the CCD camera are mounted on a translation stage to allow the acquisition of the light distribution in the exit pupil plane and the image O' for all the possible object positions.

Results

With the object located at 11 positions, four series of 10 images were acquired. For the first series, the CCD camera was conjugated with the output pupil plane and it observed the spatial frequency spectrum of the line grating object. Then the camera was conjugated with the image O' and the phase contrast images of the line grating object were acquired (second series). The object was laterally translated to centre the number 3 object and the phase contrast images of that object were acquired (third series). Finally, the object was laterally translated to centre a constant object and the phase contrast images of a 'constant' phase object were acquired (fourth series). The 10 images of each series were averaged to reduce the noise level.

Figure 4.4 shows the average images obtained with the object at an optical distance of -460, -305, -163, and -74 o.u. from the source. The first row shows the spatial frequency spectrum of the line grating object in logarithmic scale (rescaled). The logarithm was taken to reveal the first order of diffraction, which is faint compared to the zero order. The scale of the spatial frequency spectrum linearly depends on the source to object distance, $z_1 - d$ (Equation 3.4). The separation ξ between the first order of diffraction and the zero order of diffraction was plotted against $z_1 - d$. A linear fit to ξ returned a slope of 30.6×10^{-3}, a value close to the calculated $\lambda u\, z_2/z_1 = 30.1 \times 10^{-3}$, using the focal length of lenses L_1 and L_2 instead of z_1 and z_2. For the four images of Fig. 4.4, the scaling factor (Equation 3.6) is 24.4, 16.9, 9.4, and 4.4 mm. If the source was at infinity, the scaling factor would have been the back focal length of the lens system L_1 and L_2, about 80 mm. The spatial frequency spectra shown are from 3 to 18 times smaller than the spectrum that would have been measured with the source at infinity. In these images, the phase plate is not visible. It is within the strong zero order of diffraction and its size is similar to the visible first order diffraction.

The second and third rows show the phase contrast images of the line grating and of the number 3 objects. The illuminated part of the object, the field of view, is linearly related to the source to object distance $z_1 - d$, in the geometric approximation. These images show the illuminated part of the object with a good contrast for all source to object distances $z_1 - d$, superimposed on a spatially varying background light intensity.

The fourth row shows the background light distribution, that is the

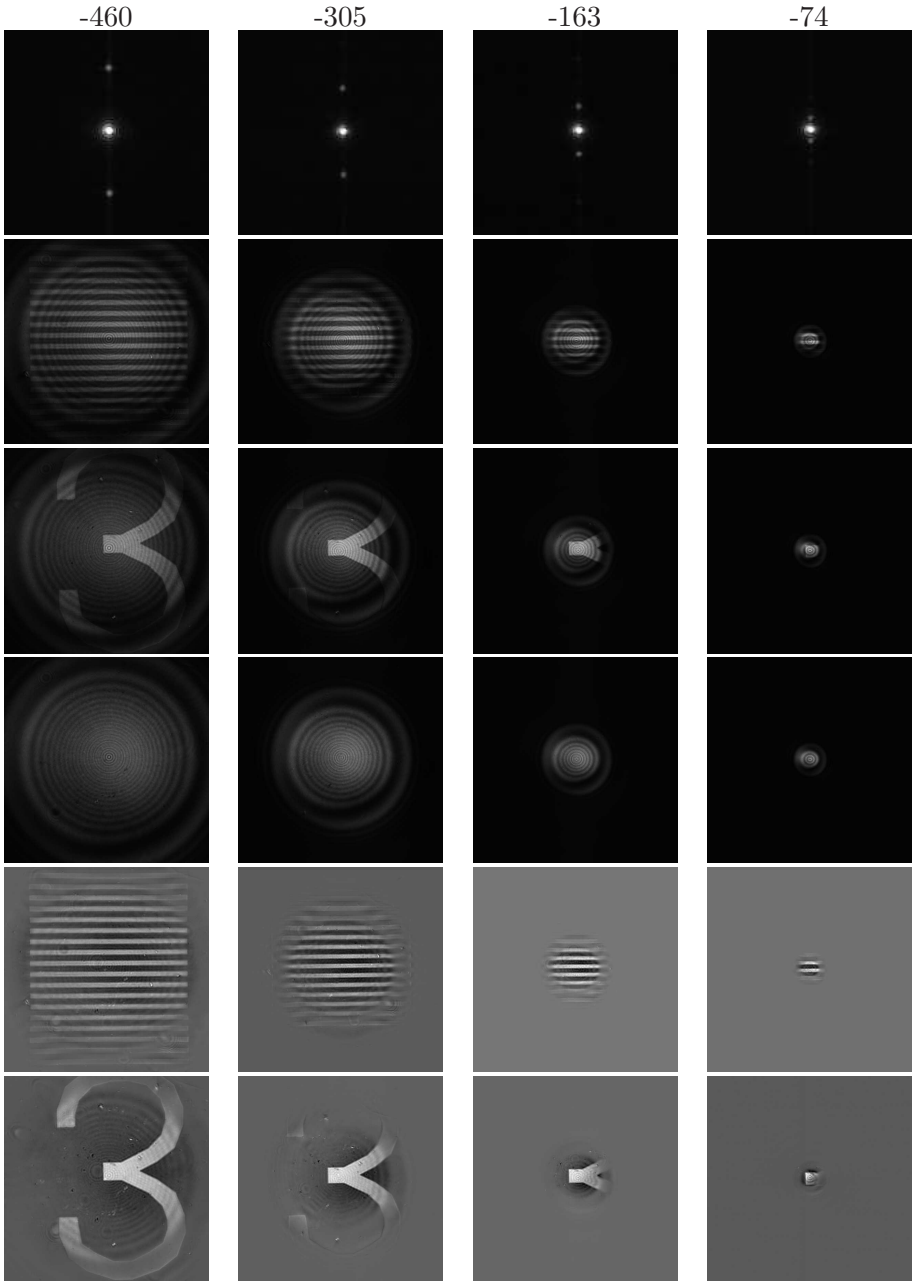

Fig. 4.4. Effect of the source to object distance. Each column shows images obtained with the object located at an optical distance given at the top (optical units) from the source. The first row shows the spatial frequency spectrum of the line grating object (logarithmic scale). The second and third rows show the phase contrast images of the line grating and of the number 3. The fourth row shows the background light distribution. The fifth and sixth rows show the difference between the phase contrast images and the background images with rescaled grey levels.

zero order of diffraction. This light distribution is the Fresnel diffraction pattern, in the image plane O', of the diaphragm aperture filtered by the phase plate. This light distribution is smooth close to the centre and shows ring features that are prominent at the edge. At an optical distance of -163 and -74 o.u., a small amount of aberration is revealed by the asymmetry of the ring pattern.

The fifth and sixth rows show the difference between the phase contrast images and the background images with rescaled grey levels. These images demonstrate what can be achieved when the background light distribution is known.

In Fig. 4.5, vertical line profiles (average of 5 pixels) through the phase contrast images of the line grating object (Fig. 4.4 second row), through the background light distribution (Fig. 4.4 fourth row), and through the differential images (Fig. 4.4 fifth row) are shown. The contrast of the phase contrast image and the variation of intensity across the field of view can be observed. In the third row, the profile corresponding to the differential image, the modulation of the contrast by the background light intensity is visible. The fourth row shows that the normalised image—the image divided by the background—has a constant contrast across the field of view and that the contrast does not depend on the source to object distance.

The image shows a good contrast as long as the diffracted light passes outside of the phase-shifting area of the phase plate. This can be observed by using a phase plate with a large phase-shifting area. In Fig. 4.6, the radius of the phase-shifting area is $b = 160\,\mu$m. The images A and B show the spatial frequency spectrum of the line grating object (saturated). In these images the disc, which was illuminated with a light emitting diode from the side, is visible. In A, the diffracted light passes outside of the disc. In B, the first order of diffraction passes inside of the disc. The images C and D are the corresponding phase contrast images. The image C is similar to the images in Fig. 4.4. The image D is the high-pass filtered image of the line grating object, where the first harmonic is suppressed.

4.2 Reflection

The geometry used in this experiment is directly relevant to *in situ* retinal imaging. The optical path is broken in two paths, an illumination

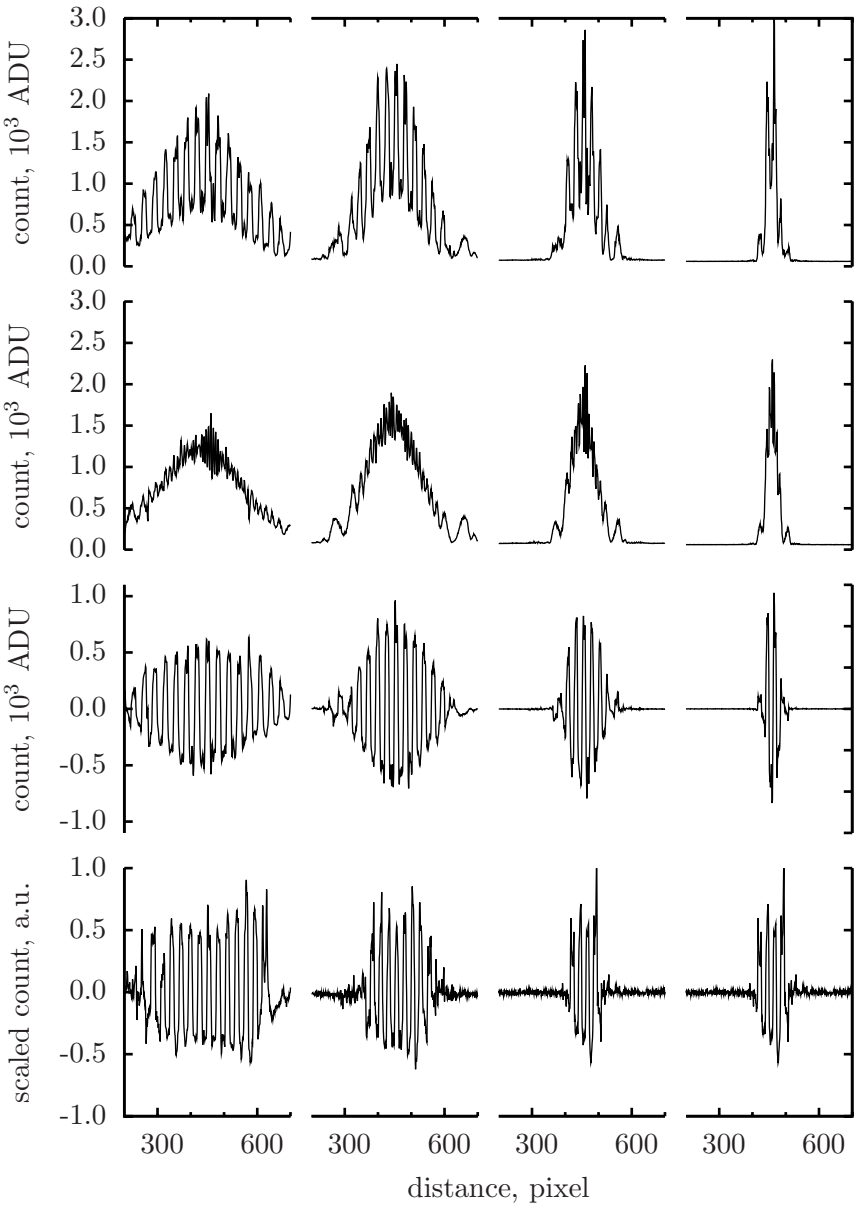

Fig. 4.5. The first row shows the intensity profile through the phase contrast image of the line grating (Fig. 4.4 second row). Each profile is an average of five-pixel columns. The second row shows the profile through the background image (Fig. 4.4 fourth row). The third row shows the difference between the data of the first row and the data of the second row (Fig. 4.4 fifth row). The fourth row shows the data of the third row scaled by the data of the second row.

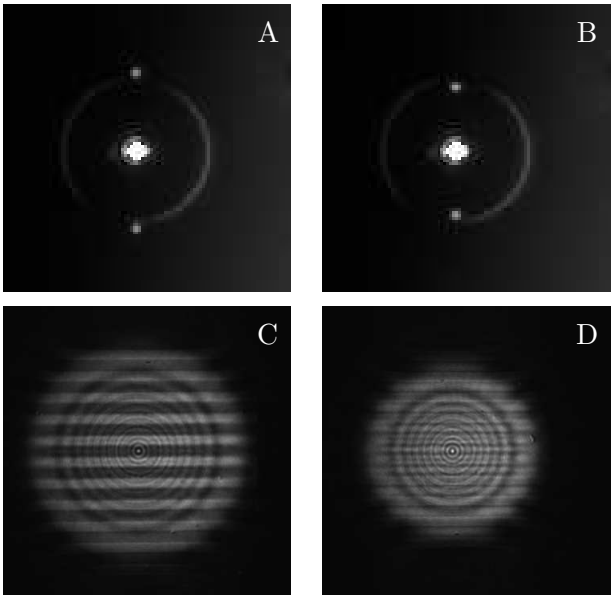

Fig. 4.6. High-pass filtering by the phase plate. A and B show the spatial frequency spectrum of the line grating object (saturated) and the phase-shifting area of the phase plate. C and D show the corresponding phase contrast images. The source to object distance is approximately -250 o.u.

and an observation. For illumination, the light from a laser source is focused by an objective lens onto a diffusing surface, creating a secondary source. For observation, the light from the secondary source trans-illuminates the object and it is used to form the phase contrast image. The number 3 object described in Section 4.1 is used. A phase plate with the same geometry as the one described in Section 4.1 is used, except that the thickness of the phase-shifting disc is 170 nm, producing a phase shift of about 0.72 rad at $\lambda = 675$ nm, about 41°.

Optical setup

A drawing or the main components of the optical setup is shown in Fig. 4.7. A collimated beam, from a laser diode emitting at 675 nm, is transmitted through a 50/50 cube beam splitter BS. The achromatic lens L_1 ($f = 100$ mm) focuses the light through the phase object O onto a piece of white paper. The illuminated part of the paper is a secondary light source σ. The light from σ is transmitted through the object O, the lens L_1, and the diaphragm D. The light is reflected by

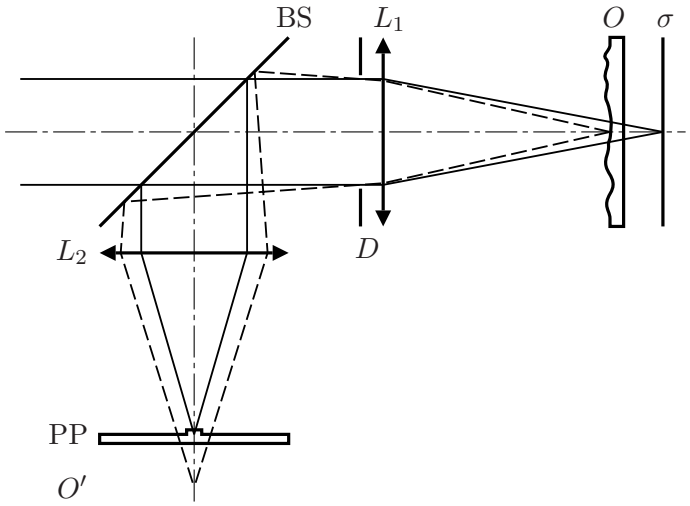

Fig. 4.7. Setup for phase contrast imaging in reflection. The light from a collimated beam is transmitted by the beam splitter BS and focused by the lens L_1 on a white paper. The illuminated spot forms a 'secondary' source σ. The light back scattered from σ trans-illuminates the object O. The lens system L_1 and L_2, limited by the diaphragm D, images the source σ on the phase plate PP and the object O is imaged at O'.

the beam splitter BS towards the lens L_2, which is an infinity corrected microscope objective (MPL 10×, Olympus Corp., Japan) with a focal length of 18.0 mm and a numerical aperture (NA) of 0.25. The lenses L_1 and L_2 form an image of the the source σ onto the phase plate PP, and they form an image of the object O at O'. The radius of the phase plate is $b = 10\,\mu$m. An additional relay system is used to image O'. This system consists of two achromatic lenses with infinite conjugate ratio and a focal length of 50 and 200 mm.

To reduce the amount of unwanted light reflection, a few steps were taken. The incoming beam diameter was limited, within the illumination part, to a diameter slightly smaller than the diameter of the aperture of D. In the relay system, another diaphragm was conjugated with D. The object O was tilted at about 80° from the optical axis. Furthermore, the speckle pattern was averaged by moving the paper during the acquisition period of the CCD camera.

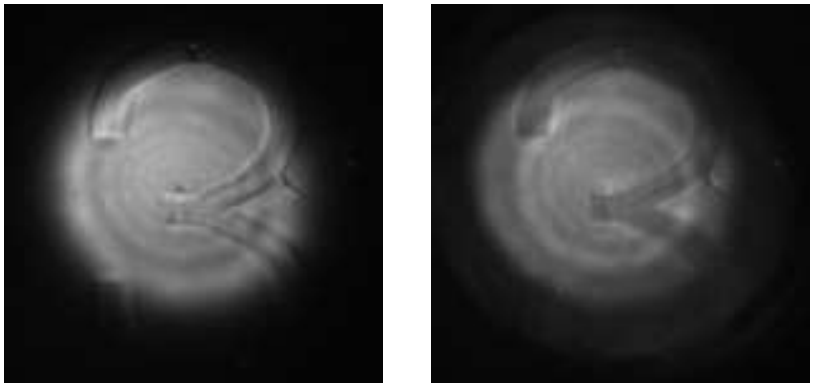

Fig. 4.8. Images of the number 3 object obtained in reflection. The object is located at an optical distance of −85 o.u. from the source. Left, without phase plate, the sharp edge of the object are visible dues to the low-pass filtering of the optical system. Right, with phase plate, the object appears darker than the background.

Results

The phase object was imaged with and without the phase plate. The object was located at an optical distance of −85 o.u. Figure 4.8 shows an image of part of the object obtained without the phase plate (left) and with the phase plate (right). The image without the phase plate reveals the phase discontinuities of the phase object through the normal low-pass filtering due to the limited aperture of the optical system used. The image with the phase plate shows a phase contrast image of the object where the number 3 appears darker than the background. The contrast for the central part of the number 3 is about 14 %.

The contrast of the number 3 in the image shown in the left side of Fig. 4.8 is reversed compared with the contrast shown in Fig. 4.4. Both images were acquired with the same object and with phase plates of the positive contrast type. Possible explanations for this contrast reversal lie in the difference in coherence of the illumination light due to scattering and the illumination geometry, or to some double pass effect.

4.3 Thick phase object

In this experiment, phase contrast images are obtained through a thick phase object. The optical system works in transmission and the thick object is a sample from a retina.

Phase object

I had access to different samples of retina, kindly provided by Professor Peter Dockery (Department of Anatomy, NUIG). Pig eyes fixed in a formaldehyde solution were obtained from an off-campus source. Each eye was cut open and the fixed retina, which has a consistency similar to a tissue paper, was peeled off from the eye fundus. The retina separates from the fundus between the photoreceptor outer segments and the retinal pigment epithelium [13]. The retina was mounted flat on a microscope slide. Its appearance was whitish probably due to the effect of the fixative on the retina. The fixed retina scatters the light and phase contrast images could not be obtained.

It was not practicable to obtain 'fresh', i.e., unfixed, retinas from the pig with minimal post-mortem alterations. On-campus, a few rats are euthanized every week for the needs of different research groups. Professor Dockery obtained fresh eyes from albino rats and extracted the retinas. The fresh rat retina appears more transparent than the fixed pig retina. The fresh retina, however, is difficult to manipulate, as it has the consistency of gel.

The rat retinas were mounted on a glass cover slip, immersed in a glycerin solution, and covered by another cover slip. The edges were sealed using a nail varnish. The mounted retinas reached the optical bench about two hours after the animal death, and the imaging session lasted for another two hours.

Optical setup

A drawing of the optical setup is shown in Fig. 4.9. A laser diode emitting at a wavelength of 675 nm is coupled into a single mode fibre, the tip of which is the source σ. The source is imaged on the left side (in Fig. 4.9) of the thick object O by the relay system consisting in lenses L_1 and L_2. The lenses L_1 and L_2 are achromats with infinite conjugate ratio working on axis with focal length of 25 mm for L_1 and 16 mm for L_2. The lens L_2 has a clear aperture radius of 3.5 mm. It is working at an f-number of 2.3 and probably introduces some aberrations.

The microscope arrangement (L_3 and L_4) conjugates the image of the source σ (left side of O) with the phase plate PP. This arrangement images the right side of the object O at O'. The lens L_3 is an infinity corrected microscope objective (MPL 10×, Olympus Corp., Japan) with

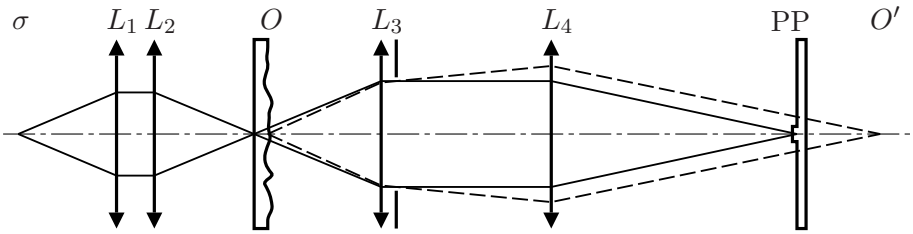

Fig. 4.9. Transmission setup for phase contrast imaging of a thick phase object. The source σ is the tip of a single mode optical fibre. The lens system L_1 and L_2 images the source σ on one side of the object O (left side in the drawing). The microscope system L_3 and L_4 conjugates the left side of the object O, i.e., the image of the source σ, with the phase plate PP and the right side of the object O with O'.

a focal length of 18.0 mm and a numerical aperture (NA) of 0.25. The lens L_4 is an achromat with a focal length of 120 mm.

An additional relay system (not shown in Fig. 4.9) with unit magnification conjugates the plane of interest with a CCD camera. The transverse magnification of the system was measured for different object positions using a graduated scale.

Both the lens system (L_1 and L_2) and the object O are mounted on two independent translation stages. For the experiments, the lens system (L_1 and L_2) was axially translated such that the image of the source σ is conjugated with the phase plate, and this with the light passing through an object with an equivalent optical path as the mounted retina (side of the sample mount). To axially position the object, Indian black ink was deposed on a small area of the cover slip facing the source (Fig. 4.10). The surface of the cover slip was positioned at the focus of the beam using the knife-edge technique. Then the object O was translated axially to bring the left side of the object O at the focus taking into account the refractive index difference between air and the cover slip material [228].

In practice, the images were obtained at source to object distance greater than the thickness of a retina. It is not clear whether the retina was folded, and therefore thicker, or whether the alignment procedure was imprecise.

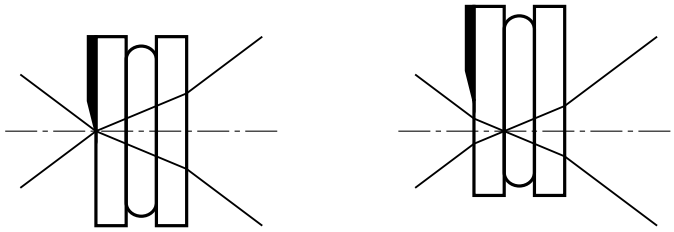

Fig. 4.10. Illustration of the thick phase object mounted between two cover slips and of the alignment procedure using the knife-edge technique. Left, The front surface of the cover slip is located at the beam focus. Right, The front surface of the object is at the beam focus. The object was moved to the left and up.

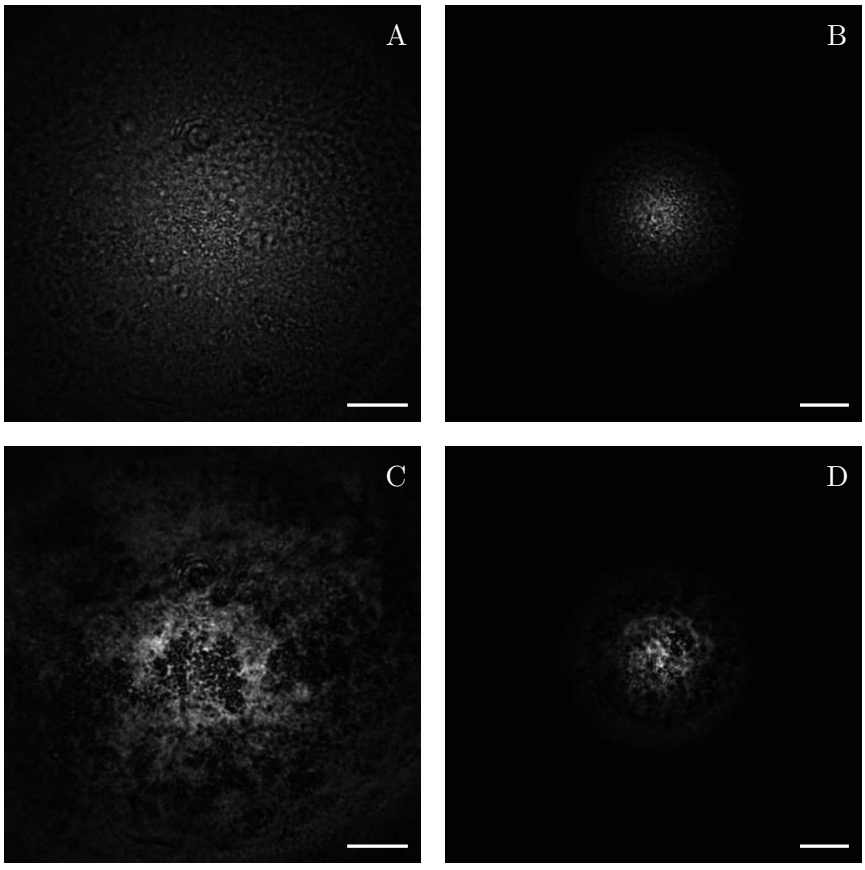

Fig. 4.11. Images of a rat retina; (A and B) without phase plate, (C and D) with the phase plate. The images A and C show the same area of the retina and they were obtained at a source to object distance of about −860 o.u. The image B and D show another area of the retina and they were obtained at −260 o.u. The scale bars represent a length of 50 μm.

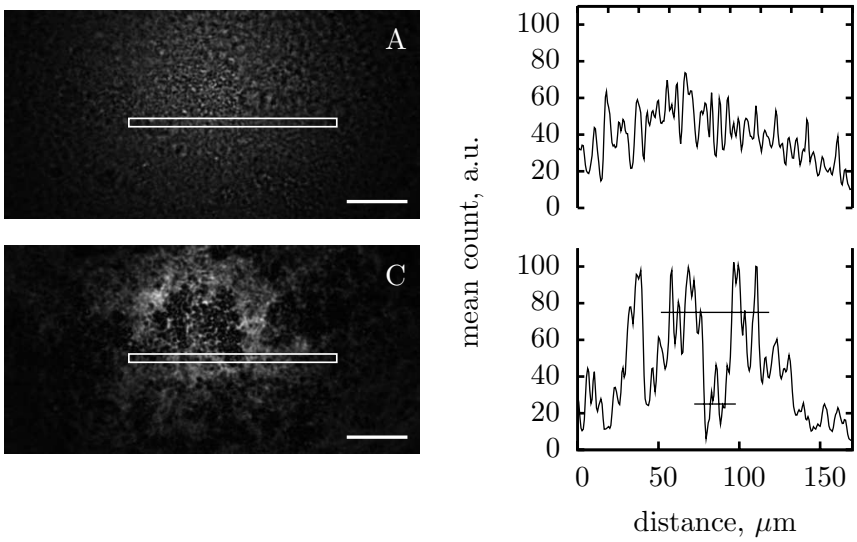

Fig. 4.12. (left) Part of the images A and C from Fig. 4.11 with an horizontal area passing through a contrasty feature in image C, (right) corresponding horizontal line profile of intensity given in arbitrary unit. The dark feature in image C has a contrast of approximately 50 % computed between the two horizontal lines shown in the line profile. This feature presents no contrast in image A.

Results

Samples images of a rat retina are shown in Fig. 4.11. The images A and B were obtained without the phase plate. The images C and D were obtained with the phase plate. The images A and C show the same area of the retina. They were obtained at a source to object distance of −860 o.u. The images B and D show another area of the retina. They were obtained at a distance of −260 o.u. The four images have a width of 500 pixels and are displayed without post-processing.

The images C and D, obtained with the phase plate, present contrasty features not visible in the images A and B. The left side of Fig. 4.12 shows part of the image A and C with an horizontal line passing through one contrasty feature. On the right, the corresponding line profile for the image A and C is shown. In the image A, there is no visible change in the measured intensity. In the image C, the feature presents a contrast of about 50 %. These features are present over the full field of view, but their visibility decreases away from the centre following the decrease of the background light intensity.

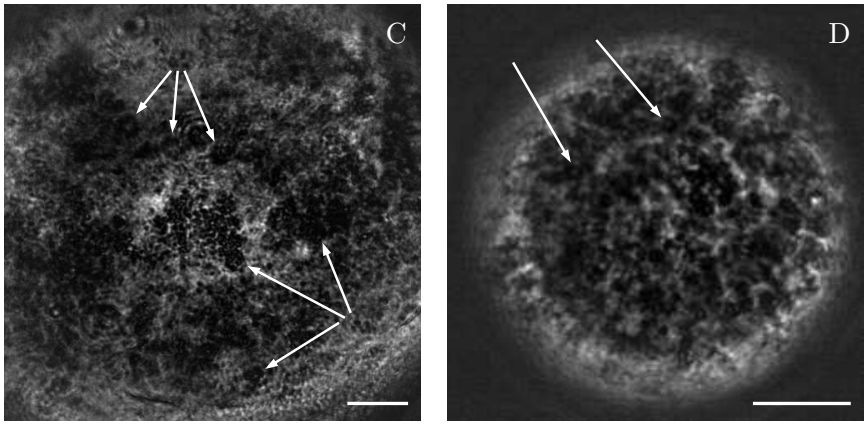

Fig. 4.13. Phase contrast images from Fig. 4.11 (C and D) after post-processing. The image D was rescaled. The scale bars represent a length of 50 μm and the arrows point to features discussed in the text.

In Section 4.1, the background light intensity in the absence of the object was known and this information was used to obtain a constant background level by post-processing. For the images of the rat retina, the background light intensity in the absence of the retina is not known. As an approximation, the background was flattened using the intensity distribution in the images A and B. The centre of the light distribution was found by cross-correlation of the image with a two dimensional Gaussian distribution. The radial intensity profile was calculated using all the pixels. This profile was averaged over radial bins of 10 pixels. The averaged profile was fitted with a Gaussian function

$$f(r) = \frac{C_1}{\sqrt{2\pi\sigma^2}} \exp\left[-\frac{1}{2}\frac{r^2}{\sigma^2}\right] + C_2, \tag{4.2}$$

where r is the radial distance, and C_1, C_2, and σ are free parameters. The images C and D shown in Fig. 4.11 were flattened and the result is shown in Fig. 4.13.

The arrows in image C point toward dark disc-like features, some with a bright centre. These features are between 8 and 18 μm wide and may be related to neural cells. In the image D, dark area exists, but they seems to be made up of a cluster of smaller features, as pointed by the arrows, with a width of about 8 μm. The small bright features seen in the dark area at the centre of the image C might be speckles. The bright annulus seen at the edge of the field of view in the image D is an

artifact from the post-processing.

4.4 Discussion

The experiments described in this chapter demonstrate that phase contrast images can be obtained using the original geometry proposed in Chapter 3, i.e., using the light back-reflected from a diffuser located at a finite distance from the object. This geometry for phase contrast imaging was patented [3].

The results obtained in the first experiment—using a point source at a variable distance from the object—confirmed the validity of the theoretical description given in Section 2.5 for an ideal point source. In particular, both the spatial spectrum and the field of view scale with the source to object distance, the diffracted light passing through the phase-shifting area of the phase plate does not contribute to the image, and the contrast of the image remains essentially constant, as long as the diffracted light is not shifted by the phase plate. The phase contrast method of Zernike works with a large departure from the usual collimated wave illumination.

In the second experiment, phase contrast images were obtained using the light back-reflected from a diffuser as a secondary light source. This result shows that phase contrast images can be obtained in a geometry similar to the eye and using the light from a diffuse secondary source.

In the third experiment, some features were made visible in phase contrast images of the retina of a rat. In this experiment, the light is transmitted through the full retina, a thick phase object. The interpretation of the phase contrast images is complicated by the nature of the object. In particular, the observed phase variations were accumulated along the optical path through the full retina. These images contain information from the object at different depths projected with different transverse magnifications onto a two dimensional plane. In addition, the unfixed retinas have undergone some post-mortem changes, which affect the optical properties of the tissue. The interpretation of these images could be facilitated by co-localising with images of fluorescence marked cells. The question of the interpretation was postponed until phase contrast images of the human retina are obtained *in situ*. The contrast enhancement obtained in this experiment demonstrates that phase contrast images can be obtained with light transmitted through

a thick inhomogeneous object.

The results obtained in this chapter demonstrate that the proposed geometry works with a diffuse secondary source and with light transmitted through a thick phase object. These two conditions are met in the experiments with human subject described in Chapter 5.

5

Experiments with human subjects

In Chapter 3, phase contrast imaging was discussed for a simple eye model. It was found that to image the ganglion cells with an optimal contrast, i.e., for a complete separation in the output pupil plane between the diffracted and the direct light, the secondary source should be smaller than approximately 11 μm. It is possible to control the light incident on the eye to illuminate a small part of the eye fundus. To overcome diffraction, the probing beam should be larger than 2 mm. The secondary source, however, cannot be fully controlled. Its extent depends on the amount of light scattering in the ocular media and on the light interaction with the tissue of the fundus, including back reflections by different layers and lateral diffusion. To minimise the size of the secondary source, I selected:

- Young subjects to minimise intraocular light scattering [229];
- An illumination light with a wavelength strongly absorbed by the pigments present in the ocular fundus, 543 nm [198];
- A large aperture at the subject pupil, 6.7 mm in diameter, with an adaptive optics system to correct the ocular aberrations.

In this chapter, the design and construction of the fundus camera and the adaptive optics system are described. The performance of the camera is analysed. The light distribution of the secondary light source obtained in four subjects is presented. And attempts to image the inner retina are described.

Part of this chapter has been the subject of a publication [230]. The safety of the exposure to pre-corrected laser beams used in the experiments described in this chapter is discussed in Appendix B.

5.1 Setups for *in vivo* retinal imaging

The main components of the fundus camera are shown in Fig. 5.1. Starting from the subject's eye at the top of the drawing, the system consists of a telescopic arrangement (ophthalmic lens OL and lens L_1) which images the pupil of the subject onto the deformable mirror (DM). After the DM, the optical system is separated in two parts by the dichroic beam splitter (DBS), which transmits the long waves (red) and reflects the short waves (green). One part of the system is for wavefront sensing and the other part is for fundus imaging.

Closed-loop adaptive optics system

The adaptive optics system is built with the same deformable mirror DM and wavefront sensor (WS) geometry as the system developed by Dalimier *et al.* [231], which was itself based on earlier works [73, 80].

For wavefront sensing, the laser beam B_1, coming from a laser diode (not shown in Fig. 5.1) emitting at 675 nm, is focused on the eye fundus from a 1-mm diameter pupil located 2-mm off-axis. The power of the beam B_1 at the cornea is less than 4 μW. The light back scattered from the fundus exits the eye pupil. This pupil is conjugated with the deformable mirror DM and the Hartmann–Shack wavefront sensor WS. At the wavefront sensor, the beam is spatially sampled by an array of lenses with a diameter of 0.2 mm and a focal length of 7.5 mm. At the cornea, the 6.7-mm pupil is sampled every 0.6 mm. An image of the spots is formed on a CCD camera (Retiga EX, QImaging, USA) by an unit magnification telescopic arrangement ($4f$-system) using two achromats with a focal length of 120 mm. The CCD camera acquires frames at a rate of 12 to 18 Hz depending on the frame acquisition period.

For wavefront correction, the data from the wavefront sensor is converted, using the pseudo-inverse of the interaction matrix of the system [231, 232], into the voltage commands used to control in closed-loop the 35-element bimorph DM (AOptix Inc, USA). The interaction matrix of the system is composed of columns of measured spot centroids. Each column contains the centroids measured in response to the activation

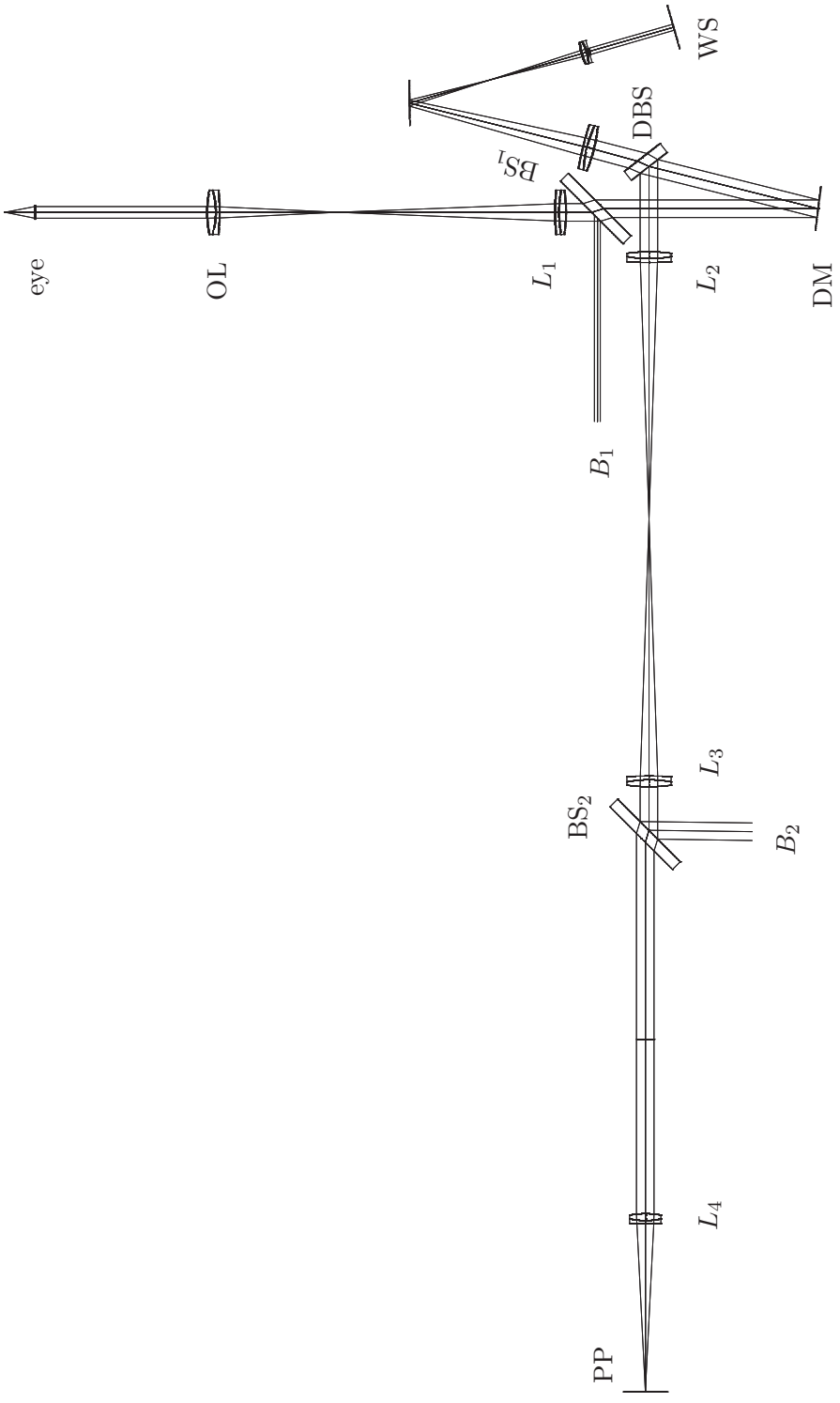

Fig. 5.1. Schematic drawing of the optical system, CCD charge coupled device, BS beam splitter (90 % transmission, 10 % reflection), DBS dichroic beam splitter, L lens, OL ophthalmic lens, B laser beams, DM deformable mirror, WS wavefront sensor

of a single actuator. The performance of the deformable mirror in correcting ocular aberrations was assessed by Dalimier and Dainty [233]. The calculated average root mean square (RMS) wavefront error was 60 nm, after correction of generated ocular aberrations over a pupil diameter of 4.8 mm. These ocular aberrations were generated using the wavefront statistics obtained by Thibos *et al.* from a population of 200 young subjects with well corrected defocus and astigmatism [61].

Compared to the adaptive optics system of Dalimier [232], the current system uses a slightly larger aperture diameter in the subject pupil, 6.7 mm instead of 6 mm, the system has no separated astigmatism corrector, and the probing beam is not scanned.

Retinal imaging

For imaging, a secondary source is created on the ocular fundus from the light of an He-Ne laser emitting at 543 nm. The light from the laser passes through a mechanical shutter (LST200, nmLaser Product, Inc, USA) which controls the exposure duration from a minimum of about 3 μs. The beam is spatially filtered and expanded 16 times (Linos Photonics, Germany). Its power is controlled by neutral density filters mounted on a wheel system. The beam passes through an aperture mask located in a plane conjugated with the subject pupil. This mask limits the beam diameter and blocks the central area—to avoid light reflections from the optical components of the system and from the surfaces of the cornea and the crystalline lens. At the eye pupil, the beam has a annulus shape with an inner diameter of 2.6 mm and an external diameter of 6.7 mm. The laser, mechanical shutter, beam expander, neutral density filters, and mask are not shown in Fig. 5.1.

About 10 % of the light from the laser beam (B_2 in Fig. 5.1) is reflected by the beam splitter BS_2 towards the lenses L_3 and L_2. The beam is reflected by the dichroic beam splitter DBS and by the deformable mirror DM. The shape of the DM is adjusted to minimise the effect of the ocular aberrations. The beam is transmitted at about 90 % by the beam splitter BS_1 towards the lenses L_1, the ophthalmic lens OL, and the subject eye.

The light back scattered by the ocular fundus exits the eye through a 6.7-mm diameter clear aperture. The light returns to the beam splitter BS_2, where it is transmitted at about 90 % towards the lens L_4 and the phase plate PP. Not shown in Fig. 5.1, a relay system mounted on

a translation stage—similar to the one shown in Fig. 4.3—conjugates the desired image plane with the CCD camera (Rolera-XR, QImaging, USA).

All the lenses of the system are achromats working at an f-number of 15. For an emmetropic eye, with an equivalent focal length in air of 17.0 mm, each pixel of the camera subtends an angle of 0.20 minute of arc (arcmin) at the pupil of the eye, an angle corresponding to approximately 1 μm at the retina.

The subject was asked to bite into a dental impression mounted on a three-axis translation stage. The subject pupil was aligned with the system with the aid of a pupil monitor (not shown in Fig. 5.1). The ocular aberrations were measured with the wavefront sensor. The tip and tilt was minimised by adjusting the incident angle of the wavefront sensor probing beam B_1. The defocus was minimised by axially translating the subject eye and the ophthalmic lens OL relative to the rest of the system. Due to the longitudinal chromatic aberration of the eye, the beam B_2 is not focused in the same plane as the wavefront sensing probing beam B_1. To correct for the longitudinal chromatic aberration and more generally to vary the conjugation of the beam B_2 relative to the beam B_1, the lens L_2 was axially translated.

5.2 Performance of the adaptive optics system

The performance of the mirror, the calibration of the wavefront sensor, the measured point-spread function (PSF) of the system, and some remarks on the adaptive optics system performance on subject eyes are described here.

The deformable mirror

In addition to the 35 actuators, the deformable mirror has two global actuators that control the overall shape of the mirror. The mirror used by Dr. Dalimier was set by the factory to be 'flat' when turned on. In addition, the non-linear response (surface changes) of the electrodes are compensated by the software. The surface of the mirror used for this work was measured using a commercial Twyman–Green interferometer (Fisba Optik, Switzerland). It was found

- that the mirror is not flat,

- the actuator response is not linear with the command, and
- the mirror resets itself when a high voltage is applied.

The commands needed to be sent to the two global actuators to flatten the mirror were found by trial and error. The non-linearity was measured for the central actuator. In closed-loop operation with a moderate gain, the non-linearity slows down the response time of the system. A correction of the non-linearity by the software was not attempted. The response time of the closed-loop system was not measured. The fact that the mirror reset itself was more problematic. The company informed us that it was a new security feature. When an actuator command is above 90 % of its range for about 10 seconds, the mirror is reset. To avoid loosing control of the mirror, the command was limited to 90 % of the range.

The influence functions of the 35 actuators were measured using a command at 25 % of the maximum. The calculated maximum stroke of the different actuators is comparable to the mirror used by Dalimier and Dainty [233].

The wavefront sensor calibration

The subject eye is replaced by an incident collimated beam, a point source whose light is collimated by a 80-mm focal length achromat. The interference fringes seen on the shear-plate, used to check the beam collimation, showed no sign of aberration. This collimated beam is used to measure the aberrations of the system. By axially translating the ophthalmic lens OL, a known defocus is added to the system. The calibration data is obtained by measuring the wavefront aberrations for different known defocus.

Aberrations of the system

In order to test the optical quality of the optical system including the presence of non-common path errors, the single-pass point-spread function (PSF) of the illumination path and the single-pass PSF of the observation path were measured separately. First, the adaptive optics system was used to correct the aberrations measured by the wavefront sensor using a collimated beam instead of the subject's eye (as for the wavefront sensor calibration).

For the illumination path, the subject's eye was replaced by an achromatic lens with a focal length of 16 mm and the PSF was re-imaged on

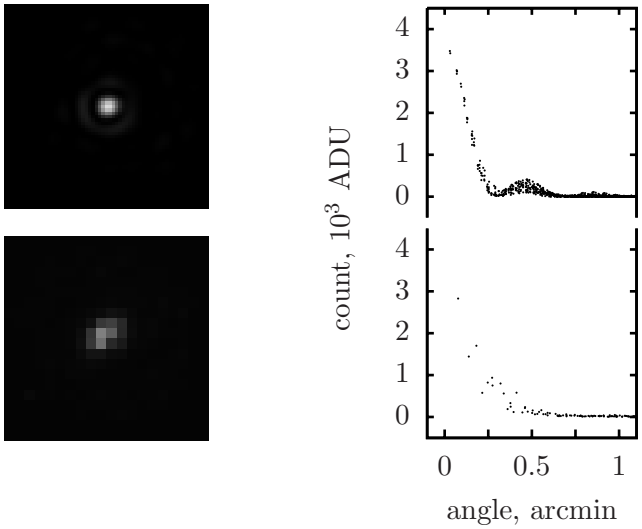

Fig. 5.2. (left) Single pass PSF image of the system illumination (top) and observation (bottom). On the right, the corresponding radial intensity profile are shown. The intensity is given in the CCD camera analog to digital counts, ADU. The image width is 4.0 arcmin.

the CCD camera (Rolera XR, QImaging, USA) using a 50x microscope objective. Figure 5.2 (top) shows an image of the single-pass PSF and its radial profile. The half width at half maximum (HWHM) of this profile was found to be 0.146 arcmin using a fit of the function $[2J_1(v)/v]^2$. This value is very close to 0.143 arcmin, the HWHM of a diffraction limited PSF. As seen by the height of the first ring, some small aberrations are present. These aberrations are probably introduced by the achromatic lens used as artificial eye, which is not part of the setup. This lens is working with an f-number of 2.4 compared to 15 for the lenses of the system. This assumption was not verified. The effect of the central obscuration was not considered.

To measure the PSF of the observation path, the subject's eye was replaced by a plane wave—a point source collimated by a 80-mm focal length achromat—and the PSF was recorded by the system CCD camera. The system was designed to sample the retinal image at the Shannon's critical frequency. The fine structures of the diffraction limited PSF are, therefore, under sampled (Fig. 5.2 right). Most of the intensity is within a radius of 0.5 arcmin (fit gives a HWHM of 0.22 arcmin). The observation path is identical to the illumination path except for the beam splitter BS_2, the lens L_4, the phase plate PP, and the relay system.

As the beam splitter BS_2 and the phase plate PP have a surface peak to valley figure given at 63 nm and the lenses are working at an f-number of 15, the single-pass PSF of the observation path is likely to be close to diffraction limit.

Measurements of ocular aberrations

It is impossible to prove that the adaptive optics system is correcting all the ocular aberrations. Only the correction of the *measured* aberrations is known to within a measurement error.

All the experiments with the human subjects were performed with the help of Dr. Dalimier. From her experience with a similar adaptive optics system, she was able to tell when the system was not performing well. A series of observations is consistent with a correctly working adaptive optics system.

- When the adaptive optics loop is closed, the amount of measured wavefront aberrations decreases to about 0.1 μm root mean square (RMS) without tip and tilt, a level comparable to the level obtained with similar adaptive optics systems [71, 92] (see Fig. 5.3).
- The measured aberrations were stable and the command vector, visualised at run-time, showed similar features between successive measurements. The same amount of static aberrations seems to be corrected at each trial. In addition, this indicates that the random and time-varying speckle noise did not dominate the measured signal.
- At most, only a few actuators were saturated. This was achieved by correcting an appropriate number of mirror modes ranging from 23 to 27.
- The width of the measured secondary source decreased after adaptive optics correction of the aberrations, see Section 5.3, Fig. 5.4.

We are, therefore, confident that the adaptive optics system was working as well as other single mirror closed-loop adaptive optics systems.

5.3 Images of the secondary source

In this thesis, the image of the secondary source is important for phase contrast imaging. Such images have been obtained since 1955, to obtain

the single-pass modulation transfer function (MTF) of the eye, at first using a slit source [234–237] and later using a point source [238–242]. The double-pass line (or point) spread function is related to the single-pass spread function by the autocorrelation operation [243, 244], assuming a negligible amount of scattering in the ocular media and a negligible contribution from the eye fundus, *i.e.*, that the eye fundus acts as a perfect single layer diffuser. This last assumption has been discussed in most papers on the double-pass techniques and it is still debated.

One group of studies shows data consistent with the presence of a significant amount of light scattering. Williams *et al.* [241] and Liang and Williams [240] compared the MTF obtained from wavefront sensor measurements, interferometry—the method of Le Grand [245,246] which consists in forming interference fringes at the retina from two coherent point sources conjugated with the subject pupil—and the double-pass point-spread function (PSF) using a red probing beam ($\lambda = 633\,\mathrm{nm}$). They obtained the highest MTF from the wavefront sensor data. The MTF from the double-pass PSF data was the lowest. Using a green probing beam, the MTF from the double-pass PSF data was similar to the MTF obtained from the interferometric data. Gorrand *et al.* obtained the MTF of the eye and a function characterising the retinal scattering from two interferometric double-pass measurements [247–249] assuming that the light back reflected from the ocular fundus is spatially incoherent. This assumption probably holds as the acquisition time of the measurements was 0.2 second, a value which allows some wandering of the retina. These authors found that the scattering function was minimal at the *foveola* and that it increases rapidly with eccentricity. Based on this result, Gorrand *et al.* wrote that '*the modulation transfer function of the optics of the eye deduced from measurements with the areal image must be considered cautiously*' [249].

Another group of studies shows data consistent with the assumption of a negligible contribution from light scattering. Rodrìguez and Navarro [242] compared the MTF obtained from wavefront sensor measurements with the MTF obtained from double-pass PSF measurements using a green probing beam ($\lambda = 532\,\mathrm{nm}$). In a group of young subjects (mean age: 28 years), the MTF obtained from the two methods were identical. For the two other groups (mean age: 42 and 65 years), the MTF obtained from the double-pass measurements were slightly lower than the MTF obtained from the wavefront sensor measurements. Artal and Navarro

[250] measured simultaneously the double-pass PSF at the *foveola* and at 1° of eccentricity using a red probing beam ($\lambda = 633\,\mathrm{nm}$). At 1° of eccentricity, the retina is somewhat thicker than at the *foveola*. The MTF at 1° of eccentricity was systematically lower than the MTF at the *foveola*, the magnitude of the difference being similar to the measurement standard error. These authors wrote that the retina has a small effect on the double-pass PSF. In addition, they measured in one subject the amount of light detected as a function of the pupil diameter and they found it to be consistent with a reflecting surface.

Measured double-pass PSFs obtained before and after adaptive optics (AO) correction were presented by three groups [73, 153, 251], using a probing beam diameter at the subject pupil much smaller than the corrected pupil. Two of these papers reported qualitatively a tightening of the double-pass PSF after AO correction [73, 153]. Vargas-Martìn *et al.* [251], measured the peak intensity of the double-pass PSF before and after AO correction in two subjects. The peak intensity increased by 74 and 46 % but it remained below the expected value for a diffraction limited pupil.

Here, I report on the double-pass PSF measurements before and after AO correction using a large ring-shaped input pupil and a large output pupil of 6.7 mm diameter.

Methods

Four subjects, one female and three males, aged between 25 and 36 years participated in this experiment. The subject A has hazel-brown pigmented eyes, the subject B has darkly pigmented eyes, and the two subjects C and D have lightly pigmented (blue) eyes. All eyes had spherical ametropia smaller than ±2 dioptres and less than 1 dioptre of astigmatism. The measured eye was dilated using 1 % Tropicamide drops.

Through-focus series of double-pass PSF were obtained from images taken at five different focus depths, in random order. These different focus settings correspond to the axial position -60, -30, 0, 30, 60 μm—in the retina—relative to the position that gave the narrowest double-pass PSF in preliminary measurements in subject A. Three series were obtained. For the series

1. the beam was at the *foveola* with AO correction,

2. the beam was at the *foveola* without AO correction,

3. the beam was at 2° of eccentricity (1.4° nasally, 1.4° superior) with AO correction.

For each series and at each focus depth three double-pass PSFs were obtained as follows. The subject was asked to bite a dental impression attached to a three-axis translation stage. After alignment of the subject pupil, the amplitude of the tip, tilt, and defocus terms read by the wavefront sensor were minimised by adjusting the incidence angle of the wavefront sensor probing beam (tip, tilt) and by axially translating OL and the subject head (defocus). Then the subject was asked to blink, the AO loop was closed for 30 wavefront sensor frames, the AO correction was frozen, and a double-pass PSF image was acquired using an acquisition time of 1 s and a power at the cornea of 80 nW. Following each exposure, the subject could blink normally and the deformable mirror was reset. After the third exposure, the subject removed his head from the instrument. For series 2, the series without AO correction, the deformable mirror was set to correct the aberrations of the system and the operator waited about three seconds after the blink before taking the exposure.

The double-pass PSF images were analysed as follows. For each frame, a constant bias level obtained from an unexposed corner of the CCD camera was subtracted. Then the centre of the light distribution was found by cross-correlation with a 1-arcmin half width at half maximum (HWHM) Lorentzian function,

$$L(r) = C\frac{w}{w^2 + r^2}, \tag{5.1}$$

where C is a constant and w is the HWHM. The distance (visual angle) from the centre of the light distribution to each pixel was computed and a plot of the radial intensity distribution was generated assuming rotational symmetry. A Lorentzian function was fitted to the radial intensity data, up to $r = 20$ arcmin, to obtain w, the HWHM of the double-pass PSF.

The measured double-pass PSFs were compared with the double-pass PSFs reconstructed from the wavefront sensor measurements using the data from the last 10 measurements preceding each frame acquisition. For each wavefront sensor measurement, the wavefront was obtained from a least-square fit using 35 Zernike modes [141, 231]. Assuming an

unit amplitude across the full pupil, the wave was propagated to the eye fundus and the single-pass PSF were obtained from the square modulus of the field. These 10 single-pass PSF were averaged. The double-pass PSF was obtained from the autocorrelation of the averaged single-pass PSF [243] assuming a delta-correlated scattering at the retina [244]. The reconstructed double-pass PSFs showed more radial variations than the measured double-pass PSFs. Therefore, instead of plotting all pixel values, the mean radial profile was generated by averaging over 0.025 arcmin radial bins. The HWHM of these profiles was taken to be the radial bin that held the value the closest to the half maximum.

For comparison, the double-pass PSF of a diffraction limited optical system was obtained by autocorrelation of the diffraction pattern, the Airy disc. For our experimental setup, the diffraction limited double-pass PSF has a width $w = 0.19$ arcmin. For the calculation of both, the reconstructed double-pass PSF and the diffraction limited double-pass PSF, the annular shape of the input pupil was not taken into consideration.

Width of the secondary source

Without AO correction, the root mean square (RMS) wavefront aberration, without tip, tilt, and with minimised defocus, was 0.59, 0.36, 0.96, 0.41 μm for subject A to D, respectively (average of 30 frames acquired in a single recording). A set of results obtained with AO correction is shown in Fig. 5.3. These data were obtained from one of the three measurements of series 1 at a focus position of 0 μm. The first line shows the RMS wavefront aberration obtained during AO correction and its average value over the last 10 recordings. This value is the RMS residual wavefront aberration after AO correction as measured by the wavefront sensor. The second line shows the measured double-pass PSF and the third line shows its radial profile with the Lorentzian fit and width w in arcmin. The fourth line shows the reconstructed double-pass PSF and the fifth line shows its radial profile with w in arcmin.

The mean residual wavefront aberrations for all the measurements was $0.087 \pm 0.016\,\mu$m ($\pm$ standard deviation) ranging from 0.052 to $0.127\,\mu$m (N = 120). The mean residual aberration for each subject (A to D) was 0.097, 0.085, 0.097, and $0.072\,\mu$m.

Figure 5.4 shows the width of the double-pass PSF. The three measurements obtained at each focus depth were averaged.

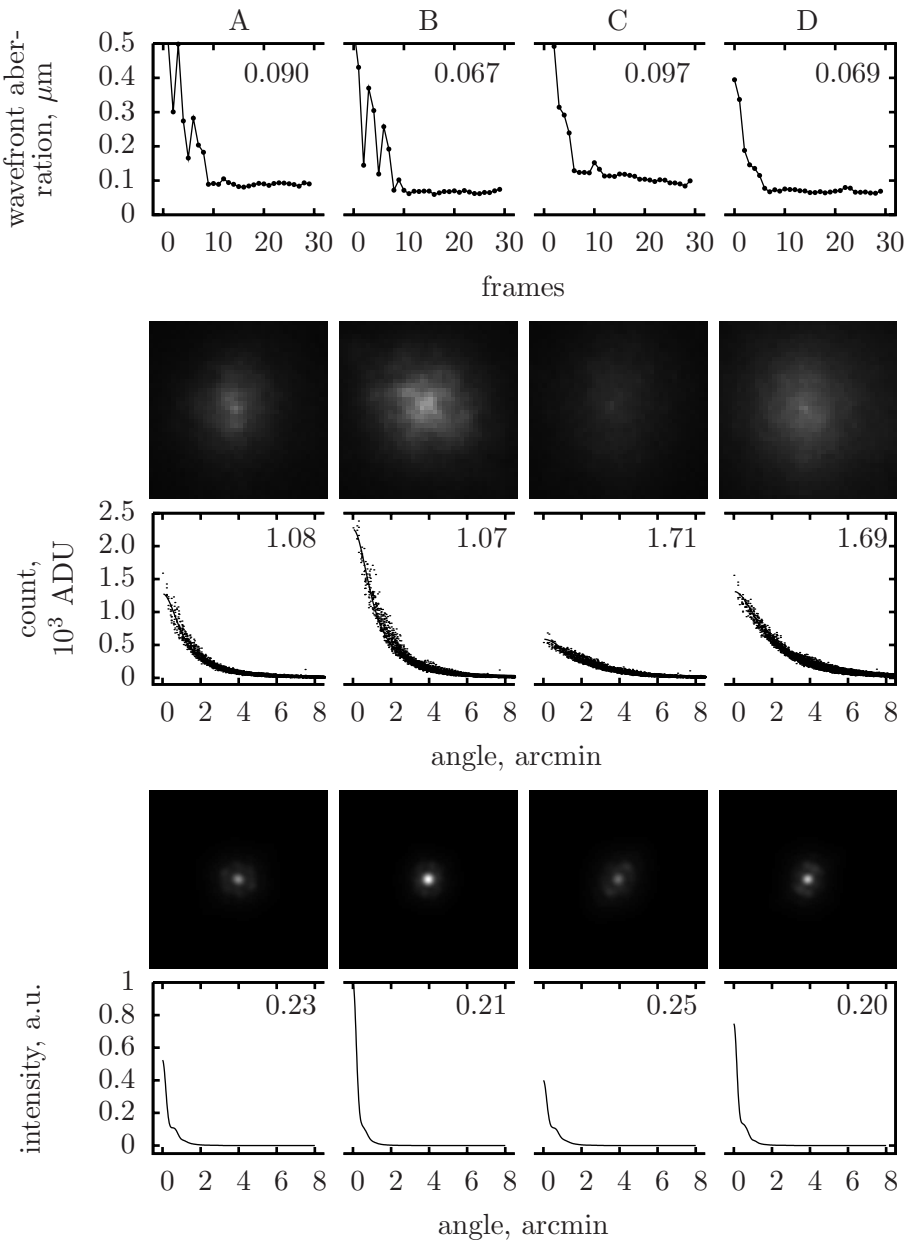

Fig. 5.3. Typical results obtained for the four subjects A to D (series 1, 0 μm). The first line shows the RMS wavefront aberration during AO correction. The following lines show the measured double-pass PSF image (second), its radial profile of intensity with the Lorentzian fit (third), the reconstructed double-pass PSF (fourth) and its radial profile (fifth), all related to the WS data of the first line. All PSF images have a width of 8 arcmin.

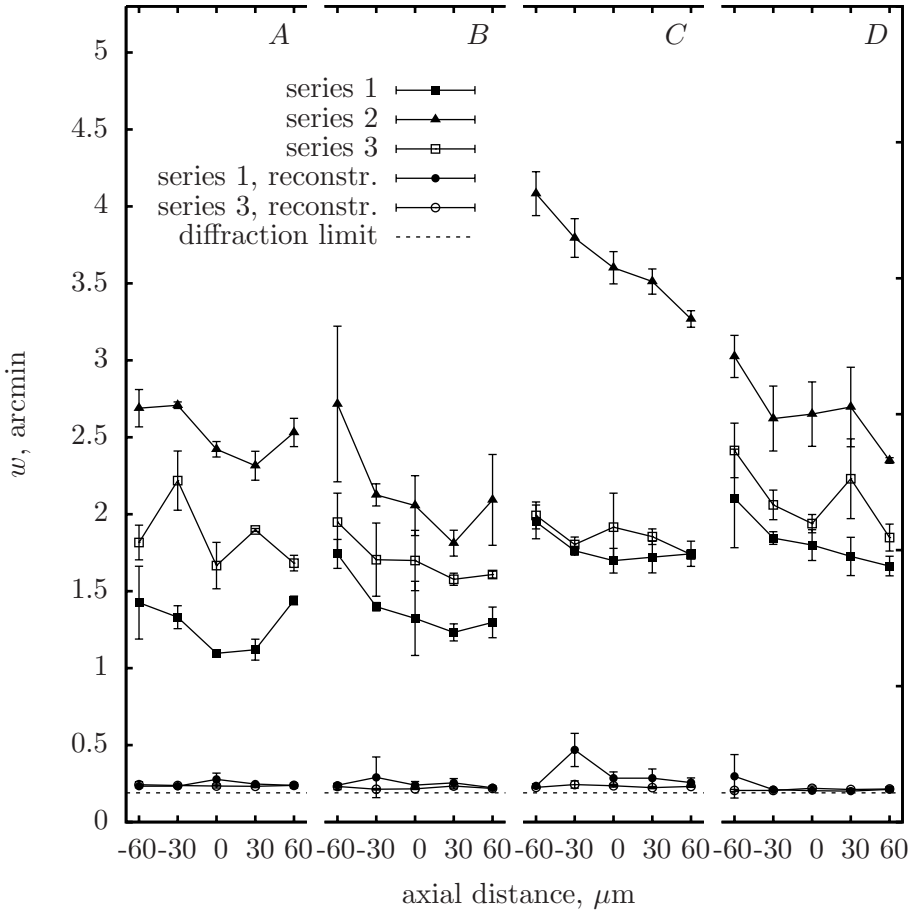

Fig. 5.4. Width w (HWHM) of the double-pass PSFs for the four subjects A to D and for the three series; triangle at the *foveola* without AO, black square at the *foveola* with AO, open square at 2° of eccentricity with AO. The width w of the reconstructed double-pass PSFs of the two series with AO corrections are shown using circles. The black circle shows the data obtained at the *foveola* and the open circle shows the data obtained at 2° of eccentricity. The annular shape of the input pupil was disregarded for the double-pass PSF reconstructions. Error bars represent the standard deviation of the mean ($N = 3$).

- The black squares represent the width of the measured double-pass PSF for series 1 (at the *foveola* with AO correction).
- The black triangles show the width obtained for series 2 (at the *foveola* without AO correction).
- The open squares show the result of series 3 (at 2° of eccentricity with AO correction).
- The circles show the width of the reconstructed double-pass PSF of series 1 (black) and series 3 (white).
- The horizontal dashed line represents the width of the diffraction limited double-pass PSF.

The width of the measured double-pass PSFs with AO correction (series 1) shows a broad minimum around the axial position 0 and 30 μm for subjects A, B, and C. For the subject D, the minimum width was measured at the axial position 60 μm. Without AO correction, the width of the double-pass PSFs of subject C decreases monotonically from the axial position -60 to 60 μm, possibly due to the uncorrected astigmatism.

The width of the minimum double-pass PSF obtained within each series is reported in Table 5.1. The following results can be noted.

- The width obtained with AO correction (series 1) was always less than the width obtained without AO correction (series 2). The width with AO correction was 48, 67, 53, and 74 % of the width without AO correction.
- The minimum width of the measured double-pass PSF for subject C and D is about 50 % larger than the width obtained for subject A and B.

series	A	B	C	D
1	1.09 ± 0.02	1.23 ± 0.06	1.70 ± 0.08	1.67 ± 0.06
2	2.32 ± 0.09	1.81 ± 0.08	3.25 ± 0.05	2.35 ± 0.02
3	1.67 ± 0.15	1.58 ± 0.04	1.74 ± 0.03	1.85 ± 0.09

Table 5.1. Minimum width w (HWHM) in arcmin of the measured double-pass PSFs obtained for each series and each subjects (mean $\pm$ standard deviation, $N = 3$).

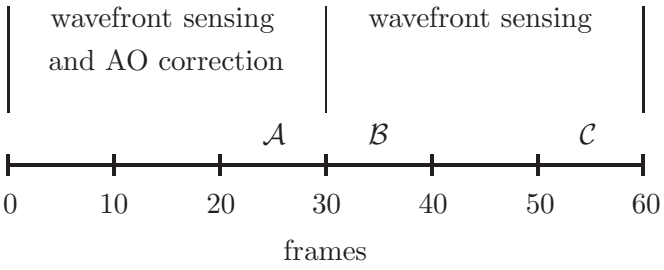

Fig. 5.5. Time frame for the analysis of the aberration evolution. $\mathcal{A}$ represents the ten frame used to measure the corrected wavefront aberration. $\mathcal{B}$ represents the ten frame used to measure the wavefront aberration during the time period corresponding to the double-pass PSF frame acquisition. $\mathcal{C}$ represents ten frames a short time after the double-pass PSF frame acquisition.

- The width of the measured double-pass PSF is 5.8 and 6.3 times larger than the width of the diffraction limited double-pass PSF, for subject A and B, respectively, and it is 9 times larger for both subjects, C and D.
- At 2° of eccentricity, the double-pass PSFs were larger than the ones obtained at the *foveola*. This difference was larger for the subjects A and B than for the subjects C and D (Fig. 5.4 open and filled squares).
- The width of the reconstructed double-pass PSFs after AO correction are smaller than 0.5 arcmin (most around 0.2 arcmin), only marginally wider the the diffraction limit (Fig. 5.4).

Additional analysis and experiments

The wavefront sensor data and its relation with the width of the double-pass PSF is further analysed and additional experiments are performed on subject A.

Wavefront aberration during 60 wavefront sensor frames. To test whether the ocular aberrations during the acquisition of the double-pass PSF images was different from the aberrations measured at the end of the period of AO correction, the wavefront aberrations was measured during 30 frames with AO correction followed by 30 frames with frozen correction (see Fig. 5.5). The frames were acquired at 15 Hz. The last frame was acquired 4 to 5 seconds after the blink. During the acquisition

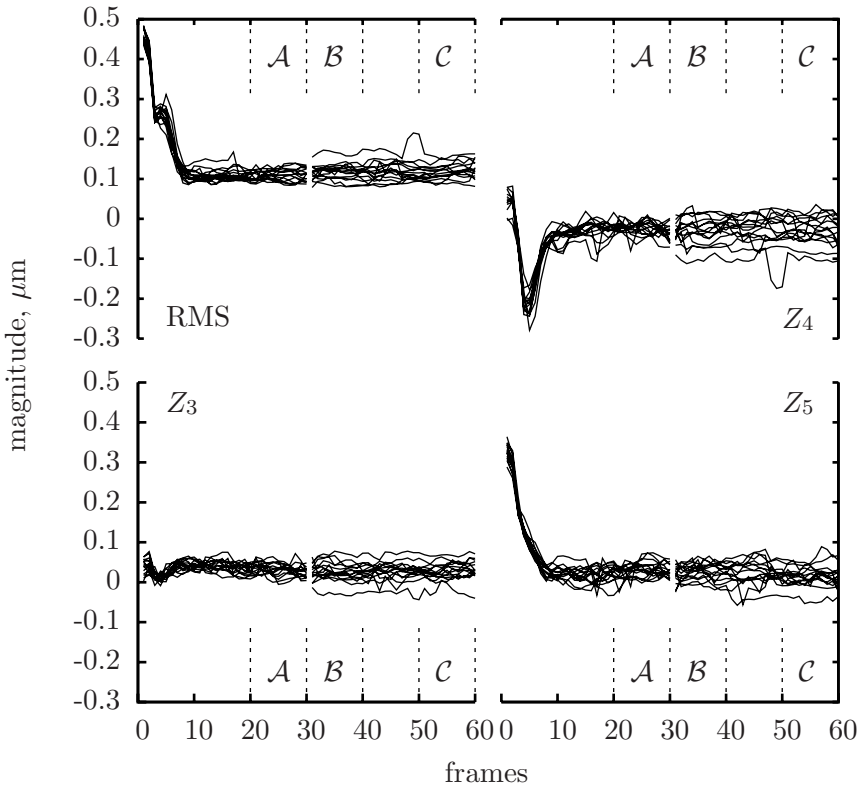

Fig. 5.6. Time sequence of the 15 wavefront aberration measurements, (top, left) RMS aberration, (top, right) Zernike defocus term, Z_4, (bottom, left) oblique astigmatism Z_3, (bottom,right) horizontal/vertical astigmatism, Z_5. The three periods considered in the text are marked $\mathcal{A}$, $\mathcal{B}$, and $\mathcal{C}$.

period, the tear film is evolving. On average, after an initial stabilising period, its contribution to the aberration increases with time [191]. Furthermore, from frame 30 to 60, the dynamic aberrations of the eye are not corrected.

The experimental conditions described for the measurements on the four subjects were repeated. After alignment, the subject was asked to blink. A sequence of 60 frames was acquired and the subject was asked to blink a few times. Two other sequences of 60 frames were acquired similarly, and the subject removed his head from the instrument. These measurements were repeated five times.

For analysis, the aberration obtained for the frames 21 to 30, period $\mathcal{A}$, for the frames 31 to 40, period $\mathcal{B}$, and for the frames 51 to 60, period $\mathcal{C}$, were considered (see Fig. 5.5). All the RMS wavefront aberrations reported, thus far, were measured during the period $\mathcal{A}$. The period

period	frames	mean ± standard error
$\mathcal{A}$	21–30	0.110 ± 0.003
$\mathcal{B}$	31–40	0.117 ± 0.005
$\mathcal{C}$	51–60	0.119 ± 0.005

Table 5.2. Mean ± standard error of the mean of the measured RMS wavefront aberration (in μm) during the three periods $\mathcal{A}$, $\mathcal{B}$, and $\mathcal{C}$ ($N = 15$).

$\mathcal{B}$ corresponds to the period used to record the double-pass PSF. The period $\mathcal{C}$ corresponds to a later period.

The time sequence of the RMS wavefront aberration and of three individual Zernike coefficients (see Appendix A), defocus (Z_4), oblique astigmatism (Z_3), and horizontal/vertical astigmatism (Z_5) is shown in Fig. 5.6. The wavefront evolves slowly. Between the three periods $\mathcal{A}$, $\mathcal{B}$, and $\mathcal{C}$, none of the Zernike coefficients increases markedly. For each measurement, the RMS wavefront aberration for the three periods was averaged. Table 5.2 shows the mean and standard error ($N = 15$) of the mean of the RMS aberration. It is 0.110 μm for the period $\mathcal{A}$, 0.117 μm the period $\mathcal{B}$, and 0.119 μm for the period $\mathcal{C}$. These mean values are not statistically different at a 95 % level, within the sensitivity of the test and of the measurements. The variations of the measured aberration are too small to explain the width of the measured double-pass PSFs (see Table 5.1).

Correlation between the RMS wavefront aberration and the width of the double-pass PSF. To test whether the width of the double-pass PSF obtained after AO correction is correlated with the remaining RMS aberration, the data from series 1 was analysed. Confounding co-variables are avoided by normalising both the measured width and the RMS aberration with the mean of the three measurements obtained in the same experimental conditions, i.e., the same axial position and the same subject. The correlation coefficient between the two groups of normalised data is 0.04.

Double-pass PSF using co-linear polarisation. As discussed in Section 3.1, the polarisation properties of the light reflected from the

ocular fundus is still debated. If the light that forms the tail of the double-pass PSF has undergone several large-angle scattering events, then the orientation of its polarisation should be random. Bueno [252] measured the degree of polarisation in the double-pass PSF image using a pupil diameter of 5 mm and a wavelength $\lambda = 633$ nm. The degree of polarisation at the centre of the double-pass PSF was 0.7 and it was 0.3 at an angle of 12 arcmin. This diffuse component may be decreased by illuminating the fundus with a linearly polarised probing beam and by blocking the cross-polarised light returning from the fundus.

To illuminate the fundus with linearly polarised light, the probing beam must pass through the cornea with its linear polarisation oriented parallel to one of the axes of the corneal birefringence. The orientation of the corneal birefringence of the tested eye was measured with a device, built by Dr. Lara-Saucedo, based on a method published by Greenfield *et al.* [253]. The corneal birefringence had the same orientation as the probing beam. Therefore, it was sufficient to place a linear polariser in the imaging path.

Three double-pass PSF images were acquired after AO correction with and without linear polariser. The time interval between these measurements was approximately three minutes. The width (HWHM) with the polariser was $w = 1.25 \pm 0.3$ arcmin and without the polariser $w = 1.20 \pm 0.3$ arcmin. The mean RMS wavefront aberration was 0.106 ± 0.005 and $0.099 \pm 0.007\,\mu$m with the polariser and without the polariser, respectively.

Double-pass PSF obtained without central obscuration. The central obscuration blocks the back reflections from the components of the optical system and from the corneal and crystalline lens surfaces. As the probing light does not enter the eye through the centre of the pupil, the light is not coupled in the photoreceptors and the contribution from this layer is strongly reduced.

Whether the light returning from the deeper layers of the fundus is coupled into the photoreceptors is still a subject of controversies (see Section 3.1). Assuming that it is not, then the optical Stiles–Crawford effect—the observed light intensity variation at the exit pupil of the eye—is only due to the incident light coupled and reflected from the photoreceptors. If the incident beam is focused on that layer and the beam is nearly diffraction limited, the double-pass PSF should reveal a

central core with a width close to the diffraction limit.

When the fundus is illuminated from a small input pupil centred on the maximum of the Stiles–Crawford effect, the directional component represents approximately 50 % of the total light returning from the fundus [201]. The magnitude of the directional component that could be measured with the optical system described here can be approximated as being half of the ratio of the obscured pupil area with the full pupil area,

$$\frac{1}{2}\left(\frac{2.6}{6.7}\right)^2 = 0.075 \approx 8\,\%.$$

With such a central core, the selected metric, the HWHM, could strongly decrease. For phase contrast imaging, however, the ratio of the light passing within and the light passing outside of the phase-shifting area of the phase plate would not change significantly.

The central obscuration was removed and three important reflections were observed. Each reflection converged to a focus in different planes of the imaging path. A small dot of Indian ink deposed on a parallel plate was placed at each focus location to block the unwanted light.

Three double-pass PSF images were obtained after AO correction using different input pupil diameters and an output pupil diameter of 6.7 mm. A strong central core was not apparent on the double-pass PSF. The measured widths were, however, smaller than the width obtained with the central obscuration. The thinnest double-pass PSF was obtained using an input pupil diameter of 4 mm, for which $w = 0.70 \pm 0.06$ arcmin. The graph in Fig. 5.7 shows the mean width w versus the diameter of the input pupil. The average RMS wavefront aberration after AO correction was $0.095 \pm 0.013\,\mu$m.

The double-pass PSF images were also recorded using different combinations of input and output pupil diameter. The width of these profiles showed a broad minimum for input and output pupil diameter of 5 mm with $w = 0.76 \pm 0.12$ arcmin. The width obtained for the full pupil diameter (6.7 mm) was $w = 1.18 \pm 0.08$ arcmin, a value larger than previously measured (see Fig. 5.7, 1.00 ± 0.05 arcmin). The average RMS wavefront aberration after AO correction was $0.091 \pm 0.011\,\mu$m.

Double-pass PSF using a red probing beam. The double-pass PSF was measured using a laser diode emitting at $\lambda = 675$ nm with a power of $3\,\mu$W at the cornea. The adaptive optics system used an

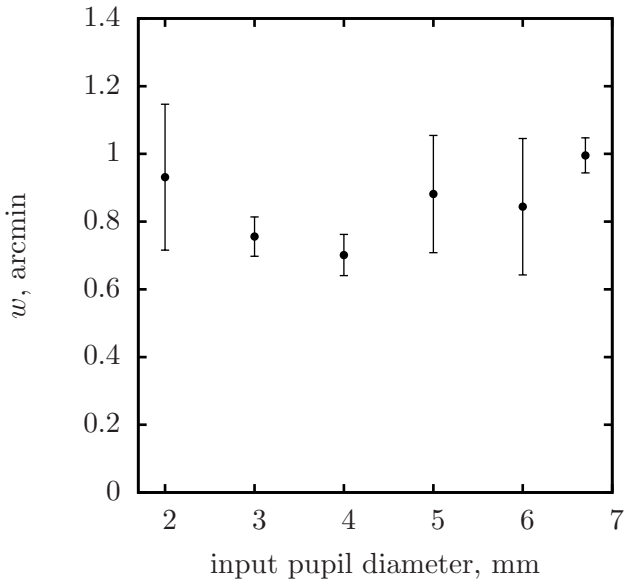

Fig. 5.7. Width w (HWHM) of the double-pass PSF obtained with an un-obstructed input pupil and an output pupil diameter of 6.7 mm, in subject A. Error bars represent the standard deviation of the mean ($N = 3$).

annular input beam with an external diameter of 7.0 mm and an inner diameter of 3.2 mm at the subject pupil. The output pupil had a diameter of 7.0 mm without obscuration.

The Hartmann–Shack spots were visually more diffuse than the spots obtained using a small input beam diameter. The adaptive optics system was not very stable. The number of corrected mirror modes was set to 15. The measured RMS aberration after AO correction was $0.13 \pm 0.01\,\mu$m.

After AO correction, a series of 30 short-exposure frames (20 ms) was acquired at 7 axial positions. For each series, the average frame was computed, the centre of the double-pass PSF was found manually, and the vertical and horizontal line profiles were fitted with a Lorentzian function. The HWHM of the profile were 3.1 and 3.4 arcmin at the best focus position [254].

5.4 Phase contrast imaging of the inner retina

To obtain phase contrast images of the inner retina, most of the light from the secondary source must pass through the phase-shifting area of the phase plate. With the knowledge that the measured light distribution of the secondary source follows approximately a Lorentzian function, it is possible to compute the fraction of light passing within a given radius and therefore within the phase-shifting area of the phase plate. I assume that there is no light beyond a radius of 20 arcmin and I approximate the fraction of light within a radius r by the ratio between the light passing through a centred area with a radius r and the light passing through a centred area with a radius of 20 arcmin. The volume under the rotationally symmetric light distribution with a Lorentzian radial profile (Equation 5.1) is [255]

$$2\pi \int_0^r L(r) r \, \mathrm{d}r = \pi C w^2 \, \ln\left[1 + \left(\frac{r}{w}\right)^2\right], \tag{5.2}$$

and the ratio of light within a given radius r is

$$\frac{\ln\left[1 + \left(\frac{r}{w}\right)^2\right]}{\ln\left[1 + \left(\frac{20}{w}\right)^2\right]}. \tag{5.3}$$

The error made by assuming that there is no light beyond a radius of 20 arcmin is likely to be small. The light distribution beyond that radius was close to the noise level. It is therefore difficult to estimate the error made using the measured light distribution. An estimate of the error can be obtained from the glare function of Vos and van den Berg [256, Equation 11] using an age of 30 years and a pigmentation factor of 1, corresponding to blue eyes. The volume below the scaled glare function from 20 arcmin to 100° was less than 1/1000 of the light within the central 20 arcmin.

A plot of the fraction of light within the radial distance r is shown in Fig. 5.8 for two light distributions. One distribution has a width $w = 0.7$ arcmin, a value corresponding to the width of the thinnest measured double-pass PSF. The other distribution has a width $w = 0.19$ arcmin and corresponds to the diffraction limited double-pass PSF. For both curves, the fraction of light within a given radius increases slowly with increasing radius. For the measured double-pass PSF, half of the light

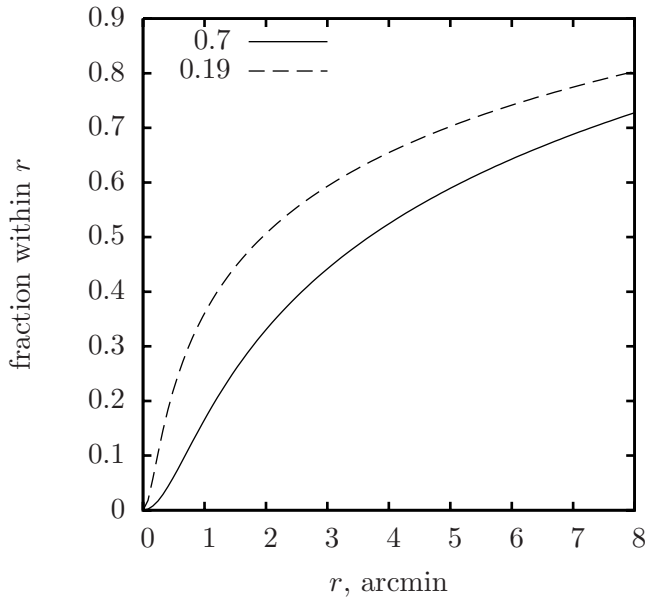

Fig. 5.8. Ratio of the light passing within a radius r and the light passing within a radius of 20 arcmin. This ratio was calculated for two-dimensional rotationally symmetric Lorentzian distributions with w equals to 0.7 and 0.19 arcmin. The first corresponds to the thinnest measured profile. The second is the profile with a width equals to the width of the diffraction limited profile.

returns within a radius r of 3.7 arcmin.

According to the calculation made in Chapter 3 using a simple model, i.e., a point source on the diffusing layer and free propagation from the source to the object, the maximum radius of the phase-shifting area of the phase plate for complete separation of the diffracted and un-diffracted light is approximately 5.5 μm or about 1.1 arcmin. From Fig. 5.8, the fraction of the light returning from the eye fundus that passes through the phase-shifting area is 0.19. This value is far from optimum. Most of the light misses the phase-shifting area and does not contribute to the image contrast. At worst, this strong light component add a 'constant' background of light and therefore it reduces the possible contrast.

Even if the width of the secondary source was equal to the width of the diffraction limited light distribution, the fraction of light passing through the phase plate with a radius $r = 1.1$ arcmin would be only 0.38.

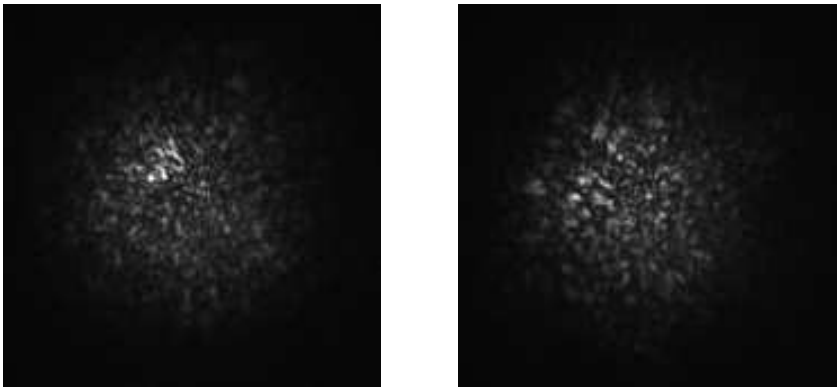

Fig. 5.9. (Left) image obtained with the phase plate, (right) without the phase plate, at an eccentricity of 2.5° and with a source to object distance of about 300 μm.

Despite the non-optimum light distribution of the secondary light source, phase contrast imaging of the inner retina was attempted in the subject A. Two images of the retina are shown in Fig. 5.9. One was obtained with phase contrast (left) and the other without phase contrast (right). These images were taken at an eccentricity of approximately 2.5° and with the focus plane located at approximately 300 μm from the source. The input pupil had a diameter of 6.7 mm with a central obscuration of 2.6 mm. The output pupil had a diameter of 6.7 mm. Between these two images, there is no visible change in the contrast of the apparent features. These images are typical of the few images acquired at different eccentricities and different focus position.

5.5 Discussion

The light distribution of the secondary source measured in the eye of four young subjects was found to follow approximately a two dimensional rotationally symmetric Lorentzian function, up to a radius of 20 arcmin. The tightest measured distribution has a half width at half maximum (HWHM) of 0.7 arcmin, approximately 3.5 μm at the fundus. The fraction of the light from the source that passes through the phase-shifting area of the phase plate is less than 20 %, and the effect of the phase plate on the image is small. The attempts to image retinal cells were not successful.

The double-pass PSF

The measured double-pass PSF is very different from the diffraction limited double-pass PSF computed assuming a negligible contribution from the light scattering in the eye. Therefore, this assumption is rejected. The light scattering in the eye together with the residual aberrations and the back reflections at the different layers from the fundus must account for the difference.

The reconstructed double-pass PSFs obtained from the wavefront sensor data are very close to the diffraction limited double-pass PSF. This result indicates that the residual ocular aberrations after AO correction are too small to account for the measured double-pass PSF, assuming that the wavefront sensor is not biased.

The light scattering in the eye comes mainly from the cellular structures of the cornea, the crystalline lens, the inner retina (part anterior to the photoreceptors), and the deeper layers including the retinal pigment epithelium (RPE), the choroid, and the sclera.

- The measurements were acquired in young subjects to minimise the light scattering from the cornea and the lens. Yet, an unknown amount of light scattering from the cornea and lens is present.

- The width of the double-pass PSF measured at 2° of eccentricity is slightly larger than at the *foveola*. This difference may be explained by the light scattering in the inner retina because the thickness of the retina at 2° of eccentricity is about two times larger than at the *foveola*. Retinal light scattering is known to exist. It was measured subjectively by Vos and Bouman [26], it is visible in the work of Zeimer *et al.* [84], and it forms the signal measured by OCT. Another difference between these two sites of measurement is a difference in the pigmentation of the deeper layers. Weiter *et al.* showed that the melanin concentration in the RPE peaks at the *foveola* [22]. Yet another difference is the diameter of the cone photoreceptors, which are larger at 2° of eccentricity than at the *foveola* [19].

- In the two lightly pigmented eyes, the width of the double-pass PSF is about 50 % larger in the two darkly pigmented eyes. The colour of the iris reflects the concentration of melanin pigment in the choroid [198]. This result indicates that the light returning

from the choroid contributes significantly to the measured double-pass PSF, in the lightly pigmented eyes. In the darkly pigmented eyes, some light returning from the choroid probably contributes to the double-pass PSF. Geeraets *et al.* found in *ex vivo* preparations from very pigmented eyes that about 5 % of the green light is transmitted through the RPE and the complete choroid [23].

From this discussion, it appears that each source of light scattering adds a contribution of unknown magnitude to the double-pass PSF. However, as the interaction of light with the different tissues of the eye is still poorly understood, three alternative explanations for the measured width of the double-pass PSF can not be fully excluded.

1. The wavefront sensor might be biased. I cannot prove that it is not. However, for the four measured subjects, the measured RMS wavefront aberrations is similar to the RMS wavefront aberrations obtained with different systems in the laboratory.

2. The width of what I call the secondary source might be the light diffracted by the object, i.e., the inner retina. This implies that the retina is not a weak phase object. Although, the approximation made in Chapter 3 shows that the amount of light diffracted from a single layer of ganglion cells is small, about 4/1000 of the incident intensity, this approximation is not valid for a thick inhomogeneous layer such as the whole retina. A more appropriate estimation requires precise knowledge of the size and the refractive indexes of the different cell components. This information is not known.

3. The double-pass PSF may be strongly affected by the forward scattering of light in the eye media, i.e., the cornea and the crystalline lens. This scattering is usually not measured for visual angles smaller than 1° [257].

For any one of these three arguments to explain the measured double-pass PSF, its effect must be quite large. If the residual ocular aberrations were large or if the forward light scattering in the ocular media and in the inner retina was strong, then it is likely that the cone photoreceptor images and our vision will be affected. If, however, most of the widening of the double-pass PSF is due to scattering occurring behind the photoreceptors, with a small contribution from the aberrations and

scattering in the ocular media, then the measured 'large' double-pass PSF is not disagreement with the presented photoreceptor images.

Comparison with previous double-pass PSF measurements

Without AO correction and using 6-mm diameter pupil, early works obtained line spread functions with width w (HWHM) ranging from 3.1 to 6.6 arcmin using a polychromatic source [236, 237]. These values are larger than the results of series 2 obtained without AO correction (w ranging from 1.8 to 3.3 arcmin). The longitudinal chromatic aberration of the eye could explain this difference. Using a 6-mm diameter pupil and a monochromatic source emitting a 532 nm, Rodríguez and Navarro measured a double-pass PSF with a width of 2.1 arcmin [242]. This value is within the range of values obtained in series 2 without AO correction. Using a 3.5-mm pupil and a wavelength of 633 nm, Liang and Westheimer showed a double-pass PSF with a width of 0.9 and 1.7 arcmin for an x and y profile, respectively [239]. These values are similar in magnitude to the values we obtained through a large pupil after AO correction. The diffraction limit for a 3.5-mm pupil is about two times larger than the diffraction limit for the pupil size used in our study.

Future directions for retinal imaging

To achieve the narrowest light distribution at the fundus, there may be an optimum pupil size that balances the effects of the light scattering and of the out of focus reflections with the effect of diffraction. The measurements obtained in subject A without central obscuration and with varying input and output pupil diameter indicate that the optimum pupil diameter is around 5 mm. The gain, however, seems to be limited. The width of the tightest double-pass PSF was 0.7 arcmin. For phase contrast imaging, even a double-pass PSF with a width of 0.19 arcmin may be insufficient due to the Lorentzian behaviour rather than the absolute width w.

If the scattering of light in the tissue of the ocular fundus plays a major role in the generation of the Lorentzian shape of the double-pass PSF, then future work should concentrate on techniques that discriminate between the light that has undergone multiple scattering events and the light that has undergone a few scattering events. Such techniques

include polarisation gating and coherence gating.

Polarisation gating has been used in a diffusing medium with low anisotropy [258, 259]. The light multiply scattered gradually looses the memory of the incident polarisation state [260]. The number of scattering events needed to randomise the polarisation depends on the medium anisotropy [258, 261]. A medium with large scattering particles has a large anisotropy and more scattering events is needed to randomise the polarisation. In the eye, large particles are present, such as the melanin granules with size ranging from 1 to 3 μm [13] and the red blood cells with diameter of about 8 μm for a thickness of about 2.7 μm [262]. The polarisation is mostly preserved [32], and the measured polarised double-pass PSF was not different than the double-pass PSF measured using all the light from the fundus (in subject A). Based on these observations, polarisation gating may not be optimum for the ocular tissue.

Coherence gating requires both a maintained polarisation and an optical path within the medium that does not differ from a reference length by more than the coherence length of the light. It is used in optical coherence tomography to obtain images in diffusing media [28]. Recently, coherence gating was used for wavefront sensor in microscopy [263, 264], and in holographic optical coherence imaging [265].

The phase contrast method of Zernike or the phase sensitive techniques based on imaging are one approach to use the phase information to image the inner retina. In Chapter 3, I pointed out a few other approaches, which should be attempted. These approaches include phase contrast OCT using a common path interferometric arrangements and the intensity transport equation. Yet another approach uses the light directly back reflected from the object with a confocal scanning laser ophthalmoscope and a phase sensitive detection mode, e.g., the differential interference contrast of Nomarski.

Future directions for phase contrast imaging in the eye

The potential of the phase contrast method of Zernike to extract information from the eye may be higher for the anterior part of the eye. With the secondary source at the ocular fundus, the source to object distance is large, and therefore, the scale of the Fourier transform is more favourable to spatial filtering. Different information may be accessed using the phase contrast method:

Wavefront sensing. The phase contrast method of Zernike has been proposed as a wavefront sensor in astronomy to detect the aberrations from the atmosphere [266–268] and to align the segmented mirror [269, 270]. Recently, Paterson has shown that the phase contrast method of Zernike is a very efficient wavefront sensor [271]. Its application to wavefront sensing of the ocular aberration was patented by Rozema *et al.* [272].

As the strongest aberrations in the eye are the low-order terms, the source needed to measure these terms must be very small, i.e., diffraction limited for the measured pupil. This may be difficult to achieve due to the light scattering in the eye. The measured intensity variations may have different sources besides phase contrast, e.g., the Stiles–Crawford effect. These effects may be removed by taking the difference between two frames, one acquired with the phase plate the other without.

Tear film. The phase contrast method of Zernike can be used to image the break up of the tear film. When the tear breaks, it forms line patterns with dimension much smaller than the observed pupil [273]. In the Fourier plane, the contribution from these lines is well separated from the continuous term and the phase contrast method should be able to reveal them.

Cells of the cornea. The spatial frequencies from the corneal cells are higher than the ones from the tear film. The diffracted light from these cells should be easily separated from the direct light. Therefore, phase contrast imaging of the cornea seems possible.

I studied the possibility to use the phase contrast method of Zernike to image cells from the cornea and I did a few tests. Here are some preliminary findings.

- The power to be sent into the eye to obtain one photon every 10 ms (to freeze the eye motion) through an area of $1\times1\,\mu\mathrm{m}^2$ (for high resolution imaging) is approximately $1.3\,\mu\mathrm{W}$ at a wavelength of $0.7\,\mu\mathrm{m}$ and assuming a Lambertian reflectance of 5 % at the fundus [199]. Using the Rolera EX CCD camera (QImaging, USA) with a quantum efficiency of 0.5 and a readout noise of $12\,\mathrm{e}^-$, a power of $31\,\mu\mathrm{W}$ is required for a signal to noise ratio of 1. If a power of $220\,\mu\mathrm{W}$ is used then the signal to noise ratio is approximately 7. This power at the cornea is 10 times below the maximum

permissible exposure for a single exposure of 10 ms according to safety standards [182, 274]. The experiment is therefore possible. However, the subject is likely to find this amount of light quite bright and several images are required. In practice, the power used should be smaller and therefore the signal to noise ratio will be smaller.

- The secondary source could be the light reflected from the anterior surface of the lens. The focus of the probing beam on this surface must be done very carefully.

- The focusing of the source and of the imaging system is constantly perturbed by the eye movements. I measured an amplitude of axial movement of subject's A cornea of $40 \pm 12\,\mu$m, a value similar to the one found in the literature [186, 187].

- In the rat eye, the light back scattered from the cornea was stronger than the light returning from the third Purkyně's image (*ex vivo*). Therefore, the incoming beam must avoid the observed area. One may discuss the need of phase contrast imaging of the cornea as confocal microscopy provides images of the corneal cells using the light back reflected from the tissue, see for example Böhnke and Masters [275].

6

Conclusions

The development of adaptive optics for the eye enabled imaging of the ocular fundus with unprecedented resolution. Images of the cone photoreceptor mosaic are now routinely obtained in different groups around the world. Twelve years after the pioneering work of Liang *et al.* [1], images of the other retinal cells are starting to be reported. But, why did the imaging of other cells take so long?

I believe that it took so long because imaging requires resolution and *contrast*. Adaptive optics provides the resolution but the retinal cells, except the photoreceptors, present little or no contrast to an intensity-based imaging system. The cells of the inner retina—anterior to the photoreceptors—are transparent. And the small contrast from the retinal pigment epithelium (RPE) cells is buried in the strong signal from the photoreceptors. Remove the photoreceptors and the RPE cells can be imaged [96].

To fully exploit the possibilities offered by the adaptive optics technique, a mechanism is needed to obtain some contrast from the retinal cells. Morgan *et al.* used the faint intrinsic fluorescence of the lipofuscin pigment located in the RPE cells to obtain images of the mosaic of these cells [113]. The other cells of the retina, however, do not naturally fluoresce. By injecting a fluorescent dye in the cells, imaging is possible. Fluorescent markers have been used to obtain superb images of the ganglion cells in animals [118, 119]. Unfortunately, the existing dyes are toxic and may not be used in humans.

Fluorescence has two advantages. It is incoherent, i.e., it does not suffer from speckle noise, and its contrast is specific to the marked object. The solution to cellular imaging of the inner retina is to be found in

the field of chemistry. The development of a non-toxic fluorescent dye will be a tremendous progress in medical imaging in general and in ophthalmology in particular.

In the mean time, I proposed to use the phase of light as a contrast agent. In this work, I reviewed the different phase sensitive techniques with regard to their applicability to retinal imaging. In the course of this study, I found that a large class of phase sensitive techniques, the ones based on imaging, can potentially be applied to retinal imaging, provided that the proper illumination geometry is used. This geometry consists in illuminating the scattering layers of the ocular fundus with a focused beam of light in order to create a point-like secondary source. The light from this source illuminates the inner retina in transmission. The output of this review is that the techniques with the greatest potential for retinal imaging are:

- The optical coherence tomography using a common-path interferometer, measuring the phase directly from the interferometric signal or from a phase-sensitive arrangement;
- The confocal scanning laser ophthalmoscope with a phase-sensitive arrangement;
- The intensity transport equation;
- The proposed illumination geometry for the image-based phase sensitive techniques.

Out of these four techniques I studied the possibility of using the image-based phase sensitive techniques.

Using the proposed geometry and the phase contrast method of Zernike, I obtained images of a glass object for various source to object distances. These images confirmed that the proposed illumination can be used for phase contrast imaging and that the field of view and the contrast formation behave has expected. Phase contrast images were obtained using the light back scattered from a diffuser in a geometry close to the eye geometry. Phase contrast images were also obtained with light passing through rat retinas, *ex vivo*. Some contrasty features were visible in the phase contrast images that were not present in the conventional images. The proposed illumination geometry was successfully used to obtain phase contrast images of *ex vivo* objects in a geometry similar to the geometry of the eye.

A fundus camera with an adaptive optics system was built for *in situ* phase contrast imaging of the human retina. The light distribution of the secondary source, called the double-pass point-spread function (PSF), was studied in detail. It was found that the double-pass PSF follows approximately a Lorentzian function within a circular area with a radius of 20 arcmin. For the measured eyes, the width of the double-pass PSF is at least 3.5 times the width of the diffraction limited double-pass PSF calculated assuming a negligible contribution from light scattering in the eye. The measured residual wavefront aberrations are too small to explain the measured double-pass PSF. The assumption of negligible light scattering in the eye is rejected. All the known sources of light scattering in the eye add their contribution to the measured double-pass PSF. The observed dependence of the double-pass PSF on the pigmentation of the eye, which is located in the choroid, and the fact that adaptive optics corrected images of the retina reveal details smaller than the width of the double-pass PSF, support the argument that a strong component of light scattering in the eye originates from the light diffusion into the tissue located posterior to the photoreceptors.

At most 20 % of the light returning from the secondary source created at the fundus of the human eye returns through the phase shifting area of the phase plate. The contrast that can be obtained using such secondary source is strongly reduced compared to the optimum condition, i.e., using a thin secondary source. The answer to the thesis question:

> Is is possible to image the retina using a phase-sensitive imaging technique by using a point-source of light created at the surface of the diffusing layer of the eye fundus?

is no. At least, it is not possible, when all the light scattered in the tissue of the fundus is used. If the size of the secondary source can be reduced, using for example, coherence-gating, then phase contrast imaging of the retina may be possible. The simplicity of the proposed method will be lost and it might be simpler to use the optical coherence tomography technique with a common-path interferometer.

In the future, images of all the retinal cells will be obtained using the high resolution provided by adaptive optics and a contrast mechanism. Whether this mechanism will be based on the phase information remains to be seen. Ultimately, a non-toxic fluorescence marker will be developed and imaging of the human body will be revolutionised.

A

$\int_0^b J_0(r'\rho)\, J_1(\rho)\, \mathrm{d}\rho$

In this appendix, the solution of the definite integral (Equation 2.31) of two Bessel functions,

$$\begin{aligned}
&\int_0^b J_0(r'\rho)\, J_1(\rho)\, \mathrm{d}\rho \\
&\quad = \quad [1 - J_0(b)]\ 2\ \frac{J_1(br')}{br'} \\
&\qquad + [1 - J_0(b) - 2\, J_2(b)]\ 6\ \frac{J_3(br')}{br'} \\
&\qquad + [1 - J_0(b) - 2\, J_2(b) - 2\, J_4(b)]\ 10\ \frac{J_5(br')}{br'} \\
&\qquad + \ \ldots \\
&\qquad + [1 - J_0(b) - 2\, J_2(b) - \ldots - 2\, J_{2n}(b)]\ (4n+2)\ \frac{J_{2n+1}(br')}{br'} \\
&\qquad + \ \ldots,
\end{aligned} \tag{A.1}$$

is obtained following an English translation [167] of Zernike's original paper [276]. In the same paper, Zernike introduced his—well known—circle polynomials. These polynomials are the basis of the diffraction theory of aberrations presented by Nijboer [8,277], they are widely used to describe wavefront aberration [128], and Zernike used them to obtain the series A.1.

In addition to the circle polynomials, three relations between Bessel

functions are needed to obtain the series A.1 [278]:

$$\int_0^z x^v\, J_{v-1}(x)\,\mathrm{d}x = z^v\, J_v(z) \tag{A.2}$$

$$\int_0^x J_1(x)\,\mathrm{d}x = 1 - J_0(z) \tag{A.3}$$

$$\int_0^z J_{v+2}(x)\,\mathrm{d}x = \int_0^z J_v(x)\,\mathrm{d}x - 2\,J_{v+1}(z). \tag{A.4}$$

The Equation A.2 is used with $v = 1$, $\int_0^z x\,J_0(x)\,\mathrm{d}x = z\,J_1(z)$, and the equations A.3 and A.4 are used to integrate odd-order Bessel functions iteratively.

A.1 The circle polynomials of Zernike

The circle polynomials of Zernike [167, 276, 277] form a complete set of orthogonal polynomials over the inner surface of a unit circle. Let (ρ, ϕ) be the polar coordinates of a point in the circle, with $0 \le \rho \le 1$ and $0 \le \phi \le 2\pi$. The circle polynomial $Z_n^m(\rho, \phi)$ takes one of the forms $R_n^m(\rho)\cos(m\phi)$ and $R_n^m(\rho)\sin(m\phi)$, where n and m are positive integers including zero, $n - m \ge 0$, $n - m$ is even, and

$$R_n^m(\rho) = \sum_{s=0}^{\frac{n-m}{2}} \frac{(-1)^s (n-s)!}{s!\left(\frac{n+m}{2}-s\right)!\left(\frac{n-m}{2}-s\right)!}\,\rho^{n-2s} \tag{A.5}$$

is a radial polynomial of degree n in ρ containing terms in $\rho^n, \rho^{n-2}, \ldots, \rho^m$. The radial polynomials are orthogonal over the unit circle

$$\int_0^1 R_n^m(r)\,R_{n'}^m(r) r\,\mathrm{d}r = \frac{\delta_{nn'}}{2n+2}, \tag{A.6}$$

where δ_{ij} is the Kronecker delta. Zernike gives the following relation

$$\int_0^1 R_n^m(r)\,J_m(\rho r) r\,\mathrm{d}r = (-1)^{\frac{n-m}{2}}\,\frac{J_{n+1}(\rho)}{\rho}, \tag{A.7}$$

where r is a radial coordinate with $0 \le r \le 1$ (see [8, 277]).

A function $W(\rho, \phi)$ defined over the unit circle can be written as an infinite sum of circle polynomials

$$W(\rho, \phi) = \sum_{n=0}^{\infty} \sum_{m=0}^{n} a_{nm}\, Z_n^m(\rho, \phi), \tag{A.8}$$

where m takes only values for which the circle polynomials are defined and the coefficients a_{nm} are given by

$$a_{nm} = \frac{1}{\pi} \int_0^{2\pi} \int_0^1 W(\rho, \phi)\, Z_n^m(\rho, \phi)\, \mathrm{d}\rho\, \mathrm{d}\phi. \tag{A.9}$$

A.2 Zernike's solution for $\int_0^b J_0(r'\rho)\, J_1(\rho)\, \mathrm{d}\rho$

In Section A.1, ρ was the normalised radial distance whereas in Equation A.1, ρ is the radial distance in optical units. In this section, the normalised distance is $\rho' = \rho/b$.

Zernike expands the $J_1(\rho)/\rho$ function in a series of polynomials,

$$\frac{J_1(\rho)}{\rho} = \sum_{n=0}^{\infty} k_{2n}\, R_{2n}^0(\rho'). \tag{A.10}$$

This equation is a simplified version of Equation A.8 obtained using the rotational property of the Bessel function. The coefficients k_{2n} are obtained—using the orthogonality property—by multiplying the two sides of the equation by another polynomial $R_{2n'}^0$ and integrating over the unit circle,

$$\int_0^1 \frac{J_1(b\rho')}{b\rho'}\, R_{2n'}^0(\rho')\rho'\, \mathrm{d}\rho' = \int_0^1 \sum_{n=0}^{\infty} k_{2n}\, R_{2n}^0(\rho')\, R_{2n'}^0(\rho')\rho'\, \mathrm{d}\rho' = \frac{k_{2n}}{4n+2}. \tag{A.11}$$

The right side is from Equation A.6. After re-arrangement,

$$k_{2n} = (4n+2) \int_0^1 R_{2n}^0(\rho') \frac{J_1(b\rho')}{b\rho'} \rho'\, \mathrm{d}\rho'. \tag{A.12}$$

Then Zernike states: *One inserts here the integral according to (25), and easily finds....* He probably meant equation (23), which is Equation A.7. By writing the Equation A.7 using $m = 0$ and $2n$,

$$\int_0^1 R_{2n}^0(r)\, J_0(\rho' r) r\, \mathrm{d}r = \frac{(-1)^n}{\rho'}\, J_{2n+1}(\rho'), \tag{A.13}$$

it appears that a solution may exist if the Bessel function of order 1 in Equation A.12 can be replaced by a Bessel function of order 0. Using Equation A.2 with $v = 1$ and $z = b\rho'$

$$\int_0^{b\rho'} x\, J_0(x)\, \mathrm{d}x = b\rho'\, J_1(b\rho'), \tag{A.14}$$

and changing the variable of integration using $x = \rho' r$ and $\mathrm{d}x = \rho'\,\mathrm{d}r$, we find

$$\rho'^2 \int_0^b J_0(\rho' r) r\,\mathrm{d}r = b\rho'\, J_1(b\rho'). \tag{A.15}$$

Replacing the Bessel function in Equation A.12 using Equation A.15 gives

$$k_{2n} = \frac{(4n+2)}{b^2} \int_0^1 R_{2n}^0(\rho')\rho' \int_0^b J_0(\rho' r) r\,\mathrm{d}r\,\mathrm{d}\rho', \tag{A.16}$$

which can be rewritten as

$$k_{2n} = \frac{(4n+2)}{b^2} \int_0^b r \int_0^1 R_{2n}^0(\rho')\, J_0(\rho' r)\rho'\,\mathrm{d}\rho'\,\mathrm{d}r. \tag{A.17}$$

The solution of the inner integral is given by Equation A.7. By replacing the variable x by r and by using Equation A.7,

$$k_{2n} = \frac{(-1)^n}{b^2}(4n+2) \int_0^b J_{2n+1}(x)\,\mathrm{d}x. \tag{A.18}$$

Let rewrite $\int_0^b J_0(r'\rho)\, J_1(\rho)\,\mathrm{d}\rho$ using the series of polynomials A.10 and the coefficients k_{2n} given by Equation A.18

$$\begin{aligned}
&\int_0^b J_0(r'\rho)\, J_1(\rho)\,\mathrm{d}\rho \\
&\qquad = \int_0^b J_0(r'\rho) \sum_{n=0}^{\infty} k_{2n}\, R_{2n}^0(\rho')\rho\,\mathrm{d}\rho \\
&\qquad = \int_0^b J_0(r'\rho) \sum_{n=0}^{\infty} \frac{(-1)^n}{b^2}(4n+2) \int_0^b J_{2n+1}(x)\,\mathrm{d}x\;\; R_{2n}^0(\rho')\rho\,\mathrm{d}\rho
\end{aligned} \tag{A.19}$$

with $\rho' = \rho/b$. After re-ordering, we have

$$\begin{aligned}
&\int_0^b J_0(r'\rho)\, J_1(\rho)\,\mathrm{d}\rho \\
&\qquad = \sum_{n=0}^{\infty} \frac{(-1)^n}{b^2}(4n+2) \int_0^b J_0(r'\rho)\, R_{2n}^0(\rho')\rho\,\mathrm{d}\rho \int_0^b J_{2n+1}(x)\,\mathrm{d}x.
\end{aligned} \tag{A.20}$$

The first integral of the right side is solved using Equation A.7 after

changing the variable of integration using $\rho' = \rho/b$ and $\mathrm{d}\rho' = \mathrm{d}\rho/b$,

$$b^2 \int_0^1 J_0(r'b\rho')\, R_{2n}^0(\rho')\rho'\, \mathrm{d}\rho' = b^2 \frac{(-1)^n}{b\rho'}\, J_{2n+1}(b\rho'). \tag{A.21}$$

The second integral of the right side is obtained for $n = 0$ from Equation A.3 and for $n > 0$ from Equation A.4 by iteration. By combining the equations A.3 and A.4 we get

$$\int_0^b J_{2n+1}(x)\, \mathrm{d}x = 1 - J_0(b) - 2\, J_2(b) - 2\, J_4(b) - \ldots - 2\, J_{2n}(b). \tag{A.22}$$

The series A.1 is obtained by inserting the equations A.21 and A.22 in Equation A.20.

$$\begin{aligned}
&\int_0^b J_0(r'\rho)\, J_1(\rho)\, \mathrm{d}\rho \\
&\quad = \quad [1 - J_0(b)]\ 2\ \frac{J_1(br')}{br'} \\
&\qquad + [1 - J_0(b) - 2\, J_2(b)]\ 6\ \frac{J_3(br')}{br'} \\
&\qquad + [1 - J_0(b) - 2\, J_2(b) - 2\, J_4(b)]\ 10\ \frac{J_5(br')}{br'} \\
&\qquad + \ \ldots \\
&\qquad + [1 - J_0(b) - 2\, J_2(b) - \ldots - 2\, J_{2n}(b)]\ (4n+2)\ \frac{J_{2n+1}(br')}{br'} \\
&\qquad + \ \ldots
\end{aligned} \tag{A.1}$$

A.3 Modified circle polynomials

Different definitions of the circle polynomials are in common use. In this section, I mention two of these definitions, one that gives an orthonormal set of polynomials and the one adopted by the vision science community.

Orthonormal circle polynomials

Noll introduced the normalised circle polynomials [279]

$$Z_j(\rho,\phi) = \begin{cases} \sqrt{n+1}\ R_n^m(\rho)\ \sqrt{2}\ \cos(m\phi) & , m \neq 0 \text{ and } j \text{ is even}, \\ \sqrt{n+1}\ R_n^m(\rho)\ \sqrt{2}\ \sin(m\phi) & , m \neq 0 \text{ and } j \text{ is odd}, \\ \sqrt{n+1}\ R_n^0(\rho) & , m = 0 \end{cases} \tag{A.23}$$

with the definition of n, m, and R_n^m being identical as Zernike's original definition. The index j is a number to order the polynomials [128] such that, an even j corresponds to a polynomial varying in $\cos(m\phi)$, and an odd j corresponds to a polynomial varying in $\sin(m\phi)$. For a given j,

$$n = \text{int}\left(\sqrt{2j-1} + 0.5\right) - 1, \tag{A.24}$$

where $\text{int}(x)$ implies the integer value of x, and

$$m = \begin{cases} 2\ \text{int}\left[\frac{2j+1-n(n+1)}{4}\right] & , n \text{ even} \\ 2\ \text{int}\left[\frac{2(j+1)-n(n+1)}{4}\right] - 1 & , n \text{ odd}. \end{cases} \tag{A.25}$$

The variance of a given set of orthonormal polynomial is the sum of the square of the corresponding expansion coefficients a_{nm}

$$\sigma_W^2 = \sum_j a_j^2, \tag{A.26}$$

excluding $j = 1$, which is the piston term.

Circle polynomials adopted by the vision science community

A taskforce formed at the Vision Science and its Application (VSIA) 1999 meeting developed standards to report the ocular aberrations [280]. In these standards, the coordinate system shown in Fig. A.1 are used. The coordinate system is the same for both eyes. Furthermore, $r = \sqrt{x^2+y^2}$, $\theta = \arctan(y/x)$, from which we have $x = r\cos(\theta)$ and $y = r\sin(\theta)$. Following Dai's notation [141], the orthonormal circle polynomials are,

$$Z_j(\rho,\phi) = R_n^{|m|}(\rho)\ \Phi^m(\phi), \tag{A.27}$$

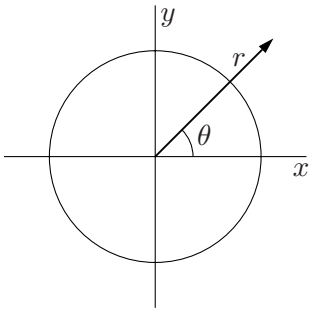

Fig. A.1. Cartesian and polar coordinate systems for reporting Zernike's polynomial in vision science (clinician's view of the patient's eye).

where $n \leq m$ and $n - m$ is even, and for each order n, m goes from $-n$ to n by steps of 2. The radial polynomials are re-defined to account for negative m

$$R_n^{|m|}(\rho) = \sqrt{n+1} \sum_{s=0}^{\frac{n-|m|}{2}} \frac{(-1)^s (n-s)!}{s! \left(\frac{n+m}{2} - s\right)! \left(\frac{n-m}{2} - s\right)!} \rho^{n-2s} \tag{A.28}$$

and the functions Φ^m are defined as

$$\Phi^m(\rho) = \begin{cases} \sqrt{2}\cos(|m|\,\phi) & , m > 0, \\ 1 & , m = 0, \\ \sqrt{2}\sin(|m|\,\phi) & , m < 0. \end{cases} \tag{A.29}$$

The ordering number j and its relation to n and m are given by

$$j = \frac{n^2 + 2n + m}{2}, \tag{A.30}$$

$$n = \text{int}\left(\sqrt{2j+1} + 0.5\right) - 1, \tag{A.31}$$

$$m = 2j - n\,(n+2)\,, \tag{A.32}$$

where $\text{int}(x)$ returns the largest integer smaller than x.

B

Safe level of laser radiation

From the point of view of safety, the experimental conditions described in Chapter 5 are potentially unsafe if the proper measures are not taken. The subject's retina is exposed to laser radiation while the head movements are neutralised, the pupil constriction is inhibited, and the aberrations of the eye are compensated to achieve a maximal concentration of light at the retina.

Standards have been developed to protect a person from hazardous exposures to laser radiation. They condense years of scientific work into simple rules from which a limiting exposure, called maximum permissible exposure (MPE), can be computed. Exposures below the MPE are expected to be safe. Sometimes, newer data reveals conditions to which the MPE are not safe [281]. Therefore, it is a good practice to limit the exposures to levels many times lower than the MPE.

It is of utmost importance to know for which viewing conditions the rules are valid. These conditions may not be explicitly stated. For example the British Standard Institute (BSI) [181] states that it adopted the rules published by the International Commission on Non-Ionizing Radiation Protection [183, 282], but the BSI publication does not mention that the rules are restricted to *normal, awake, task-oriented viewing conditions* and exclude ophthalmic instruments or devices *where the impact of normal head movements is neutralised* [282, page 439].

Most of the rules given by the American National Standard Institute [182] are identical to the rules from the International Commission on Non-Ionizing Radiation Protection. For ocular exposure with an immobilised eye or a dilated pupil, the rules are modified by the Section 8.3 entitled *Special Qualifications for Ocular Exposure* [182, page 38]. In

ophthalmic settings, the aversion reflex, which prevents someone staring at a bright source of radiation for a long duration, and the natural pupil constriction mechanism are defeated by asking the subject to look at a bright light and by using drugs to dilate the pupil [274].

In a similar fashion, when the effect of ocular aberrations are compensated and a beam of light is focused on the retina, the exposure limit given by the rules may have to be reduced to avoid hazardous exposures. A similar concern was expressed by Lund *et al.* [283].

In this Appendix, I evaluate the exposure limit based on the rules of the American National Standard Institute, following Delori *et al.* formalism [274], and I present the measures I took to avoid injury from a pre-corrected beam.

B.1 Exposure limits based on the Standard

For the exposure duration and the radiation wavelength used in this work, the hazards are of thermal and of photochemical nature. The thermal damage is the result of the absorption of optical radiation by the tissue, mainly by the melanin pigment, and its conversion to heat. It is rate dependent. The photochemical damage is the result of direct break of molecular bounds by the short wavelength radiation, which generates highly reactive free-radical that oxidise the retina. It is dose dependent, added over a period of 24 hours [274].

An important factor in the determination of the MPE is the size of the illuminated area at the eye fundus, measured as the angular substance of the source at the cornea α. For a small-source, that is for a source subtending an angle α smaller than a limiting angle $\alpha_{\min} = 1.5\,\mathrm{mrad}$, the illuminated area is not given by the source but by the optical quality of the eye and the light tissue interaction at the fundus. The two light sources used in this work are small-sources.

Wavefront sensing

The probing beam of the wavefront sensor has a power at the cornea of $3.0\,\mu\mathrm{W}$ and a wavelength of $0.675\,\mu\mathrm{m}$. This wavelength is too long to cause photochemical damage. For thermal damage, the maximum permissible power (Φ) for small-source viewing and for an exposure duration of 8.3 hours is $6.93{\times}10^{-5}\ C_\mathrm{T}\ C_\mathrm{E}\ P^{-1}$ [274, Table 3, Cell 5], with

the factors $C_{\mathrm{T}} = C_{\mathrm{E}} = 1$ and $P = 10^{7.4(0.7-0.675)} = 1.531$. The maximum permissible power Φ is $45\,\mu$W. This value is larger than the power used. Therefore, it is safe to use the wavefront sensor for up to 8.3 hours.

Retinal imaging

For retinal imaging, a laser beam emitting at $0.543\,\mu$m exposed the retina for periods of 1 s with 80 nW at the cornea. The exposures were repeated at most 3 times within 30 s and at most 30 times at a given fundus location. At this temporal frequency, the eye fundus has time, between exposure, to remove the excess thermal energy (based on the three rules for repeated exposure, not shown). Therefore, the maximal exposure will be given by either the thermal limit for a single exposure or the photochemical limit for the combined exposure. The maximum permissible power Φ according to the single exposure thermal limit is $6.93{\times}10^{-4}\ C_{\mathrm{T}}\ C_{\mathrm{E}}\ P^{-1}\ t^{-025}$ for exposure duration t ranging from 0.07 s and 2.8 hours [274, Table 3, Cell 4b], with $C_{\mathrm{T}} = C_{\mathrm{E}} = 1$ and $P = 5.4$. The maximum permissible power Φ is $128\,\mu$W. The power used are below the Φ for thermal hazard. For photochemical hazard, the maximum radiant exposure at the retina (ignoring intraocular losses) is $2.7C_{\mathrm{B}}\,\mathrm{J/cm^2}$ [182, Page 38], where $C_{\mathrm{B}} = 10^{20(0.543-0.45)} = 72.4$. For an exposed area with radius α_{min}, the maximum permissible energy is 999μJ. The exposures can be repeated more than 12000 times.

B.2 Exposure limits for pre-corrected beams

By correcting the ocular aberrations, a protection mechanism, i.e., the blur in the image of a small source, is defeated and the MPE should be reduced to prevent any risk of injury. A fully secure approach is to limit the retinal irradiance in the illuminated area at the retinal irradiance given by the Standard.

Here, I compute a correction factor C_{S}, which is the ratio of the area of the limiting surface (with a diameter given by α_{min}) and the illuminated surface. The Standard defines the beam diameter as the diameter that includes 63.2 % of the beam power. For a diffraction limited optical system with a circular pupil, the fractional power $\mathcal{L}$ within a given radial

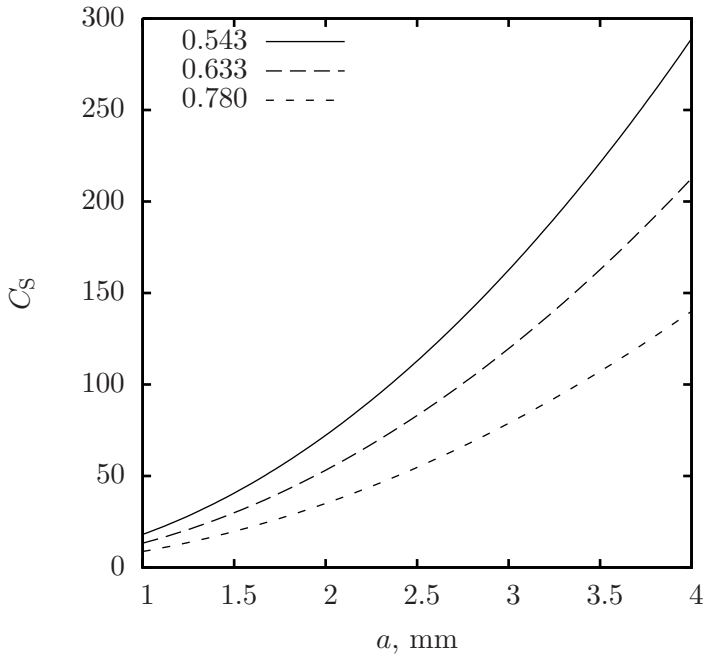

Fig. B.1. Plot of the surface ratio C_{S} for three different wavelengths in unit of μm

angle $\alpha/2$ (in radians) is [8]

$$\mathcal{L}\left(\frac{\alpha}{2}\right) = 1 - J_0^2\left(\frac{ka\alpha}{2}\right) - J_1^2\left(\frac{ka\alpha}{2}\right), \tag{B.1}$$

where $k = 2\pi/\lambda$ and a is the radius of the pupil. Solving numerically for $\mathcal{L}(\alpha/2) = 0.632$ gives $ka\alpha/2 = 2.045$ and $\alpha = 0.65\lambda/a$. The factor

$$C_{\mathrm{S}} = \left(\frac{\alpha_{\min}}{\alpha}\right)^2 = \left(\frac{1.5\times10^{-3}}{\frac{0.65\,\lambda}{a}}\right)^2 = 5.325\times10^{-6}\,\frac{a^2}{\lambda^2}, \tag{B.2}$$

with a and λ in meters. A plot of C_{S} is shown in Fig. B.1 for three different wavelengths. Both the thermal limit and the photochemical limit given by the Standard should be divided by the factor C_{S}.

For wavefront sensing, the probing beam diameter is 1 mm and the difference is very small. For retinal imaging, however, the beam diameter is 6.7 mm and $C_{\mathrm{S}} = 203$ at $\lambda = 0.543\,\mu$m. The limits computed in Section B.1 become $0.63\,\mu$W (thermal) and $4.9\,\mu$J or 61 exposures (photochemical).

The correction factor C_{S} used in this work is probably too restrictive. Several arguments can be advanced for a smaller correction.

- The factor C_S strongly depends on the definition of the beam diameter. By using the diameter given by the first zeros of the Airy disk, the factor C_S would be 3.5 times smaller.

- The measured wavefront aberrations after adaptive optics correction are larger than Maréchal criterion. Therefore, the light distribution at the fundus is not diffraction limited.

- The minimum measured retinal injuries have a diameter of 25 μm corresponding to the limiting angle $\alpha_{\min}$ [274].

- The MPE given by the Standard have a quadratic dependence with α for large angles and a linear dependence for small angles. Two mechanisms can explain this difference. For small illuminated area, the choroidal blood circulation is more efficient at removing the excess heat [284] and the small ocular movements have a larger effect [285]. There is no reason to assume that these two mechanisms will not work for illuminated area smaller than the limiting area.

- Recently Lund *et al.* showed that the retinal damage threshold measured after adaptive optics correction for an exposure duration comparable with the exposure duration used in this work was only marginally smaller that the threshold measured without adaptive optics correction [286]. The threshold reduction ranged from 20 to 50 %.

- The fraction of light within a given radius for the measured double-pass PSF (Chapter 5) is much smaller than the fraction of light expected for a diffraction limited double-pass PSF.

An extrapolation towards small angle α of the linear relationship between the Standard's MPE and the angle α might be a sufficient correction. In that case, the factor C_S becomes 2.3×10^{-3} a/λ, with a and λ in meters. For retinal imaging with a beam diameter of 6.7 mm and a wavelength of 0.543 nm, $C_S = 14$ and the limits computed in Section B.1 become 9.2 μW (thermal) and 71 μJ or 880 exposures (photochemical).

Bibliography

[1] J. Liang, D. R. Williams, and D. T. Miller. Supernormal vision and high-resolution retinal imaging through adaptive optics. *J. Opt. Soc. Am. A*, 14(11):2884–2892, 1997.

[2] E. H. Thall. Retinal diagnostic device, 1998. United States Patent #5751395.

[3] E. Logean and C. Dainty. Imaging of phase objects, 2008. European Patent # EP1964510 (A1).

[4] H. A. Quigley. Neuronal death in glaucoma. *Prog. Retin. Eye Res.*, 18(1):39–57, 1998.

[5] H. A. Quigley. Number of people with glaucoma worldwide. *Br. J. Ophthalmol.*, 80:389–393, 1996.

[6] D. A. Atchison and G. Smith. *Optics of the Human Eye*. Butterworth-Heinemann, Edinburgh, 2000.

[7] J. Porter, H. M. Queener, J. E. Lin, K. Thorn, and A. Awwal, editors. *Adaptive Optics for Vision Science: Principle, Practices, Design, and Applications*. Wiley-Interscience, USA, 2006.

[8] M. Born and E. Wolf. *Principles of Optics: Electromagnetic Theory of Propagation, Interference and Diffraction of Light*. Cambridge University Press, Cambridge, UK, 7$^{\text{th}}$ edition, 1999.

[9] V. Ronchi. Resolving power of calculated and detected images. *J. Opt. Soc. Am.*, 51(4):458–460, 1961.

[10] J. W. Strutt (Baron Rayleigh). Investigations in optics, with special reference to the spectroscope. In *Scientific Papers by John William Strutt, Baron Rayleigh*, volume 1, 1969–1881 (originally published in Phil. Mag. 8 and 9, 1879 and 1880), pages 416–459, Cambridge, 1899. Cambridge University Press.

[11] A. J. den Dekker and A. van den Bos. Resolution: A survey. *J. Opt. Soc. Am. A*, 14(3):547–557, 1997.

[12] B. Považay, B. Hofer, C. Torti, B. Hermann, A. R. Tumlinson, M. Esmaeelpour, C. A. Egan, A. C. Bird, and W. Drexler. Impact of enhanced resolution, speed and penetration on three-dimensional retinal optical coherence tomography. *Opt. Express*, 17(5):4134–4150, 2009.

[13] M. J. Hogan, J. A. Alvarado, and J. Esperson Weddell. *Histology of the Human Eye: An Atlas and Textbook*. W. B. Saunders Compagny, Philadelphia, USA, 1971.

[14] J. E. Dowling. *The Retina An Approachable Part of the Brain*. Belknap Press of Harvard University Press, Cambridge, 1987.

[15] R. W. Rodieck. *The First Steps in Seeing*. Sinauer Associates, Inc., Sunderland, USA, 1998.

[16] R. K. Sharma and B. E. J. Ehinger. Development and structure of the retina. In P. L. Kaufmann and A. Alm, editors, *Adler's Physiology of the Eye*, chapter 10, pages 319–347. Mosby, St. Louis, 10^{th} edition, 2003.

[17] B. B. Boycott and J. E. Dowling. Organization of the primate retina: Light microscopy. *Philos. T. Roy. Soc. B*, 255(799):109–184, 1969.

[18] R. Navarro, P. Artal, and D. R. Williams. Modulation transfer of the human eye as a function of retinal eccentricity. *J. Opt. Soc. Am. A*, 10(2):201–212, 1993.

[19] C. A. Curcio, K. R. Sloan, R. E. Kalina, and A. E. Hendrickson. Human photoreceptor topography. *J. Comp. Neurol.*, 292:497–523, 1990.

[20] C. A. Curcio and K. A. Allen. Topography of ganglion cells in human retina. *J. Comp. Neurol.*, 300(1):5–25, 1990.

[21] S. Hattar, H.-W. Liao, M. Takao, D. M. Berson, and K.-W. Yau. Melanopsin-containing retinal ganglion cells: Architecture, projections, and intrinsic photosensitivity. *Science*, 295(5557):1065–1070, 2002.

[22] J. J. Weiter, F. C. Delori, G. L. Wing, and K. A. Fitch. Retinal pigment epithelial lipofuscin and melanin and choroidal melanin in human eyes. *Invest. Ophthalmol. Vis. Sci.*, 27(2):145–152, 1986.

[23] W. J. Geeraets, R. C. Williams, G. Chan, Jr. W. T. Ham, D. Guerry III, and F. H. Schmidt. The relative absorption of thermal energy in retina and choroid. *Invest. Ophthalmol.*, 1(3):340–347, 1962.

[24] R. Barer. Refractometry and interferometry of living cells. *J. Opt. Soc. Am.*, 47(6):545–556, 1957.

[25] A. K. Dunn. *Light Scattering Properties of Cells*. PhD thesis, University of Texas at Austin, Austin, Texas, USA, 1997.

[26] J. J. Vos and M. A. Bouman. Contribution of the retina to entoptic scatter. *J. Opt. Soc. Am.*, 54(1):95–100, 1964.

[27] R. Zeimer, M. T. Mori, and B. Khoobehi. Feasibility test of a new method to measure retinal thickness noninvasively. *Invest. Ophthalmol. Vis. Sci.*, 30(10):2099–2105, 1989.

[28] D. Huang, E. A. Swanson, C. P. Lin, J. S. Schuman, W. G. Stinson, W. Chang, M. R. Hee, T. Flotte, K. Gregory, C. A. Puliafito, and J. G. Fujimoto. Optical coherence tomography. *Science*, 254:1178–1181, 1991.

[29] M. Hammer, A. Roggan, D. Schweitzer, and G. Müller. Optical properties of ocular fundus tissues—an in vitro study using the double-integrating-sphere technique and inverse Monte Carlo simulation. *Phys. Med. Biol.*, 40:963–978, 1995.

[30] J. M. Enoch. Optical properties of the retinal receptors. *J. Opt. Soc. Am.*, 53(1):71–85, 1963.

[31] W. S. Stiles and B. H. Crawford. The luminous efficiency of rays entering the eye pupil at different points. *P Roy. Soc. Lond. B Bio.*, 112(778):428–450, 1933.

[32] G. J. van Blokland and D. van Norren. Intensity and polarization of light scattered at small angles from the human fovea. *Vision Res.*, 26(3):485–494, 1986.

[33] S. A. Burns, S. Wu, F. Delori, and A. E. Elsner. Direct measurement of human-cone-photoreceptor alignment. *J. Opt. Soc. Am. A*, 12(10):2329–2338, 1995.

[34] K Franze, J. Grosche, S. N. Skatchkov, S. Schinkinger, C. Foja, D. Schild, O. Uckermann, K. Travis, A. Reichenbach, and J. Guck. Müller cells are living optical fibers in the vertebrate retina. *Proc. Natl. Acad. Sci. U.S.A.*, 104(20):8287–8292, 2007.

[35] J. Méry. Des mouvements de l'iris, et par occasion, de la partie principale de l'organe de la vûe. *Mem. Acad. R. Sci.*, pages 261–271, 1704.

[36] R. F. Heitz. Jean Méry's neutralization of corneal dioptric power in a living eye. In *History of the Contact Lens (Part 1): Early Neutralization of Corneal Dioptric Power*, volume 11-3a of *J.*

Hirschberg's History of Ophthalmology, chapter 5, pages 156–201. Wayenborgh Publishing, 2003.

[37] N. J. Wade. Image, eye, and retina. *J. Opt. Soc. Am. A*, 24(5):1229–1249, 2007.

[38] H. von Helmholz. *Helmholtz's Treatise on Physiological Optics*. The Optical Society of America, translated from the Third German edition edition, 1924. University of Pennsylvania 2001 electronic.

[39] J. G. Ravin. Gullstrand, Einstein, and the Nobel prize. *Arch. Ophthalmol.*, 117(5):670–672, 1999.

[40] Carl Zeiss Meditec AG, Jena. *Eye Examination with the Slit Lamp*. www.meditec.zeiss.com.

[41] D. B. Henson. Optical methods for measurement of ocular parameters. In W. N. Charman, editor, *Visual Optics and Instrumentation*, volume 1 of *Vision and visual dysfunction*, chapter 17, pages 371–398. CRC Press, Inc., Boston, 1991.

[42] F. C. Delori, E. S. Gragoudas, R. Francisco, and R. C. Pruett. Monochromatic ophthalmoscopy and fundus photography. The normal fundus. *Arch. Ophthalmol.*, 95(5):861–868, 1977.

[43] R. Grey. *Vascular Disorders of the Ocular Fundus*. Butterworths, London, 1991.

[44] H. Novotny and D. L. Alvis. A method of photographing fluorescence in circulating blood in the human retina. *Circulation*, 24(1):82–86, 1961.

[45] A. von Rückmann, F. W. Fitzke, and A. C. Bird. Distribution of fundus autofluorescence with a scanning laser ophthalmoscope. *Br. J. Ophthalmol.*, 79(5):407–412, 1995.

[46] B. F. Hochheimer and H. A. Kues. Retinal polarization effects. *Appl. Opt.*, 21(21):3811–3818, 1982.

[47] A. Sommer, H. A. Kues, S. A. D'Anna, S. Arkell, A. Robin, and H. A. Quigley. Cross-polarization photography of the nerve fiber layer. *Arch. Ophthalmol.*, 102(6):864–869, 1984.

[48] J. D. Briers and A. F. Fercher. Retinal blood-flow visualization by means of laser speckle photography. *Invest. Ophthalmol. Vis. Sci.*, 22(2):255–259, 1982.

[49] P. E. Kilbride, K. R. Alexander, M. Fishman, and G. A. Fishman. Human macular pigment assessed by imaging fundus reflectometry. *Vision Res.*, 29(6):663–674, 1989.

[50] T. T. J. M. Berendschot and D. van Norren. Objective determination of the macular pigment optical density using fundus reflectance spectroscopy. *Arch. Biochem. Biophys.*, 430:149–155, 2004.

[51] J. B. Hickam, R. Frayser, and J. C. Ross. A study of retinal venous blood oxygen saturation in human subjects by photographic means. *Circulation*, 27:375–385, 1963.

[52] F. C. Delori. Noninvasive technique for oximetry of blood in retinal vessels. *Appl. Opt.*, 27(6):1113–1125, 1988.

[53] D. Schweitzer, M. Hammer, J. Kraft, E. Thamm, E. Königsdörffer, and J. Strobel. In vivo measurement of the oxygen saturation of retinal vessels in healthy volunteers. *IEEE Trans. Biomed. Eng.*, 46(12):1454–1465, 1999.

[54] M. Sharifzadeh, D.-Y. Zhao, P. S. Bernstein, and W. Gellermann. Resonant Raman imaging of macular pigment distributions in the human retina. *J. Opt. Soc. Am. A*, 25(4):947–957, 2008.

[55] M. Crittin and C. E. Riva. Functional imaging of the human papilla and peripapillary region based on flicker-induced reflectance changes. *Neurosci. Lett.*, 360(3):141–144, 2004.

[56] K. Tsunoda, Y. Oguchi, G. Hanazono, and M. Tanifuji. Mapping cone- and rod-induced retinal responsiveness in macaque retina by optical imaging. *Invest. Ophthalmol. Vis. Sci.*, 45(10):3820–3826, 2004.

[57] M. D. Abràmoff, Y. H. Kwon, D. Ts'o, P. Soliz, B. Zimmerman, J. Pokorny, and R. Kardon. Visual stimulus-induced changes in human near-infrared fundus reflectance. *Invest. Ophthalmol. Vis. Sci.*, 47(2):715–721, 2006.

[58] W. N. Charman. Optics of the human eye. In W. N. Charman, editor, *Visual Optics and Instrumentation*, volume 1 of *Vision and visual dysfunction*, chapter 1, pages 1–26. CRC Press, Inc., Boston, 1991.

[59] H. C. Howland and B. Howland. A subjective method for the measurement of monochromatic aberrations of the eye. *J. Opt. Soc. Am.*, 67(11):1508–1518, 1977.

[60] J. W. Goodman. *Introduction to Fourier Optics*. Electrical and Computer Engineering. McGraw-Hill, Boston, 2nd edition, 1996.

[61] L. N. Thibos, X. Hong, A. Bradley, and X. Cheng. Statistical variation of aberration structure and image quality in a normal population of healthy eyes. *J. Opt. Soc. Am. A*, 19(12):2329–2348, 2002.

[62] D. T. Miller, D. R. Williams, G. M. Morris, and J. Liang. Images of cone photoreceptors in the living human eye. *Vision Res.*, 36(8):1067–1079, 1996.

[63] J. I. Yellott Jr. Spectral analysis of spatial sampling by photoreceptors: Topological disorder prevents aliasing. *Vision Res.*, 22(9):1205–1210, 1982.

[64] J. I. Yellott Jr. Spectral consequences of photoreceptor sampling in the rhesus retina. *Science*, 221(4608):382–385, 1983.

[65] H. W. Babcock. The possibility of compensating astronomical seeing. *Publ. Astron. Soc. Pac.*, 65(386):229–236, 1953.

[66] C. Dainty. Adaptive optics. In P. Török and F.-J. Kao, editors, *Optical Imaging and Microscopy, Techniques and Advanced Systems*, volume 87 of *Springler Series in Optical Sciences*, chapter 10, pages 235–255. Springler, Berlin, 2003.

[67] R. K. Tyson. *Introduction to Adaptive Optics*, volume TT41 of *SPIE Tutorial Texts in Optical Engineering*. SPIE Publications, Bellingham, USA, 2000.

[68] J. W. Hardy. *Adaptive Optics for Astronomical Telescopes*. Optical and Imaging Sciences. Oxford University Press, Oxford, 1998.

[69] A. W. Dreher, J. F. Bille, and R. N. Weinreb. Active optical depth resolution improvement of the laser tomographic scanner. *Appl. Opt.*, 28(4):804–808, 1989.

[70] A. Roorda and D. R. Williams. The arrangement of the three cone classes in the living human eye. *Nature*, 397:520–522, 1999.

[71] H. Hofer, L. Chen, G. Y. Yoon, B. Singer, Y. Yamauchi, and D. R. Williams. Improvement in retinal image quality with dynamic correction of the eye's aberrations. *Opt. Express*, 8(11):631–643, 2001.

[72] E. J. Fernández, I. Iglesias, and P. Artal. Closed-loop adaptive optics in the human eye. *Opt. Lett.*, 26(10):746–748, 2001.

[73] L. Diaz-Santana, C. Torti, I. Munro, P. Gasson, and C. Dainty. Benefit of higher closed-loop bandwidths in ocular adaptive optics. *Opt. Express*, 11(20):2597–2605, 2003.

[74] J. Carroll, M. Neitz, J. Neitz, and D. R. Williams. Functional photoreceptor loss revealed with adaptive optics: An alternative cause of color blindness. *Proc. Natl. Acad. Sci. U.S.A.*, 101(22):8461–8466, 2004.

[75] A. Pallikaris, D. R. Williams, and H. Hofer. The reflectance of single cones in the living human eye. *Invest. Ophthalmol. Vis. Sci.*, 44(10):4580–4592, 2003.

[76] J. Rha, R. S. Jonnal, K. E. Thorn, J. Qu, Y. Zhang, and D. T. Miller. Adaptive optics flood-illumination camera for high speed retinal imaging. *Opt. Express*, 14(10):4552–4569, 2006.

[77] R. S. Jonnal, J. Rha, Y. Zhang, B. Cense, W. Gao, and D. T. Miller. In vivo functional imaging of human cone photoreceptors. *Opt. Express*, 15(24):16141–16160, 2007.

[78] J. Carroll, S. S. Choi, and D. R. Williams. In vivo imaging of the photoreceptor mosaic of a rod monochromat. *Vision Res.*, 48:2564–2568, 2008.

[79] H. Hofer, P. Artal, B. Singer, J. L. Aragón, and D. R. Williams. Dynamics of the eye's wave aberration. *J. Opt. Soc. Am. A*, 18(3):497–506, 2001.

[80] K. M. Hampson, I. Munro, C. Paterson, and C. Dainty. Weak correlation between the aberration dynamics of the human eye and the cardiopulmonary system. *J. Opt. Soc. Am. A*, 22(7):1241–1250, 2005.

[81] D. R. Iskander, M. J. Collins, M. R. Morelande, and M. Zhu. Analyzing the dynamic wavefront aberrations in the human eye. *IEEE Trans. Biomed. Eng.*, 51(11):1969–1980, 2004.

[82] T. Nirmaier, G. Pudasaini, and J. Bille. Very fast wave-front measurements at the human eye with a custom CMOS-based Hartmann–Shack sensor. *Opt. Express*, 11(21):2704–2716, 2003.

[83] D. D. Donaldson. A new camera for stereoscopic fundus photography. *T. Am. Ophthalmol. Soc.*, 62:429–458, 1964.

[84] R. Zeimer, M. Shahidi, M. Mori, S. Zou, and S. Asrani. A new method for rapid mapping of the retinal thickness at the posterior pole. *Invest. Ophthalmol. Vis. Sci.*, 37(10):1994–2001, 1996.

[85] R. H. Webb, G. W. Hughes, and O. Pomerantzeff. Flying spot TV ophthalmoscope. *Appl. Opt.*, 19(17):2991–2997, 1980.

[86] T. Wilson and C. Sheppard. Image formation in scanning microscopes. In *Theory and Practice of Scanning Optical Microscope*, chapter 3, pages 37–78. Academic Press, London, 1984.

[87] R. H. Webb, G. W. Hughes, and F. C. Delori. Confocal scanning laser ophthalmoscope. *Appl. Opt.*, 26(8):1492–1499, 1987.

[88] A. W. Dreher, K. Reiter, and R. N. Weinreb. Spatially resolved birefringence of the retinal nerve fiber layer assessed with a retinal laser ellipsometer. *Appl. Opt.*, 31(19):3730–3735, 1992.

[89] A. W. Dreher and K. Reiter. Retinal laser ellipsometry: A new method for measuring the retinal nerve fiber layer thickness distribution? *Clin. Vision Sci.*, 7(6):481–488, 1992.

[90] G. Michelson and B. Schmauss. Two dimensional mapping of the perfusion of the retina and optic nerve head. *Br. J. Ophthalmol.*, 79(12):1126–1132, 1995.

[91] T. Tanaka, C. E. Riva, and I. Ben-Sira. Blood velocity measurements in human retinal vessels. *Science*, 186:830–831, 1974.

[92] A. Roorda, F. Romero-Borja, W. J. Donnelly III, H. Queener, T. J. Herbert, and M. C. W. Campbell. Adaptive optics scanning laser ophthalmoscopy. *Opt. Express*, 10(9):405–412, 2002.

[93] F. Romero-Borja, K. Venkateswaran, A. Roorda, and T. Hebert. Optical slicing of human retinal tissue in vivo with the adaptive optics scanning laser ophthalmoscope. *Appl. Opt.*, 44(19):4032–4040, 2005.

[94] J. A. Martin and A. Roorda. Direct and noninvasive assessment of parafoveal capillary leukocyte velocity. *Ophthalmology*, 112(12):2219–2224, 2005.

[95] A. S. Vilupuru, N. V. Rangaswamy, L. J. Frishman, E. L. Smith III, R. S. Harwerth, and A. Roorda. Adaptive optics scanning laser ophthalmoscopy for in vivo imaging of lamina cribrosa. *J. Opt. Soc. Am. A*, 24(5):1417–1425, 2007.

[96] A. Roorda, Y. Zhang, and J. L. Duncan. High-resolution in vivo imaging of the RPE mosaic in eyes with retinal disease. *Invest. Ophthalmol. Vis. Sci.*, 48(5):2297–2303, 2007.

[97] T. Y. P. Chui, H. Song, and S. A. Burns. Adaptive-optics imaging of human cone photoreceptor distribution. *J. Opt. Soc. Am. A*, 25(12):3021–3029, 2008.

[98] H. Song, X. Qi, T. Chui, and S. A. Burns. High-resolution in vivo retinal imaging of glial cell endfeet. In *Invest. Ophthalmol. Vis. Sci.*, pages ARVO E–Abstract 4515, 2008, 49.

[99] R. C. Youngquist, S. Carr, and D. E. N. Davies. Optical coherence-domain reflectometry: a new optical evaluation technique. *Opt. Lett.*, 12(3):158–160, 1987.

[100] A. F. Fercher, C. K. Hitzenberger, W. Drexler, G. Kamp, and H. Sattmann. In vivo optical coherence tomography. *Am. J. Ophthalmol.*, 116(1):113–114, 1993.

[101] E. A. Swanson, J. A. Izatt, M. R. Hee, D. Huang, C. P. Lin, J. S. Schuman, C. A. Puliafito, and J. G. Fujimoto. In vivo retinal imaging by optical coherence tomography. *Opt. Lett.*, 18(21):1864–1866, 1993.

[102] W. Drexler, U. Morgner, R. K. Ghanta, F. X. Kärtner, J. S. Schuman, and J. G. Fujimoto. Ultrahigh-resolution ophthalmic optical coherence tomography. *Nat. Med.*, 7(4):502–507, 2001.

[103] A. F. Fercher, C. K. Hitzenberger, G. Kamp, and S. Y. El-Zaiat. Measurement of intraocular distances by backscattering spectral interferometry. *Opt. Commun.*, 117:43–48, 1995.

[104] M. Wojtkowski, R. A. Leitgeb, A. Kowalczyk, T. Bajraszewski, and A. F. Fercher. In vivo human retinal imaging by Fourier domain optical coherence tomography. *J. Biomed. Opt.*, 7(3):457–463, 2002.

[105] B. Hermann, E. J. Fernández, A. Unterhuber, H. Sattmann, A. F. Fercher, W. Drexler, P. M. Prieto, and P. Artal. Adaptive-optics ultrahigh-resolution optical coherence tomography. *Opt. Lett.*, 29(18):2142–2144, 2004.

[106] Y. Zhang, J. Rha, R. S. Jonnal, and D. T. Miller. Adaptive optics parallel spectral domain optical coherence tomography for imaging the living retina. *Opt. Express*, 13(12):4792–4811, 2005.

[107] R. J. Zawadzki, S. M. Jones, S. S. Olivier, M. Zhao, B. A. Bower, J. A. Izatt, S. Choi, S. Laut, and J. S. Werner. Adaptive-optics optical coherence tomography for high-resolution and high-speed 3D retinal in vivo imaging. *Opt. Express*, 13(21):8532–8546, 2005.

[108] D. Merino, C. Dainty, A. Bradu, and A. Gh. Podoleanu. Adaptive optics enhanced simultaneous en-face optical coherence tomography and scanning laser ophthalmoscopy. *Opt. Express*, 14(8):3345–3353, 2006.

[109] R. J. Zawadzki, S. S. Choi, S. M. Jones, S. S. Olivier, and J. S. Werner. Adaptive optics-optical coherence tomography: Optimizing visualization of microscopic retinal structures in three dimensions. *J. Opt. Soc. Am. A*, 24(5):1373–1383, 2007.

[110] R. J. Zawadzki, B. Cense, Y. Zhang, S. S. Choi, D. T. Miller, and J. S. Werner. Ultrahigh-resolution optical coherence tomography with monochromatic and chromatic aberration correction. *Opt. Express*, 16(11):8126–8143, 2008.

[111] E. J. Fernández, B. Hermann, B. Považay, A. Unterhuber, H. Sattmann, B. hofer, P. K. Ahnelt, and W. Drexler. Ultrahigh resolution optical coherence tomography and pancorrection for cellular imaging of the living human retina. *Opt. Express*, 16(15):11083–11094, 2008.

[112] D. C. Gray, W. Merigan, J. I. Wolfing, B. P. Gee, J. Porter, A. Dubra, T. H. Twietmeyer, K. Ahmad, R. Tumbar, F. Reinholz, and D. R. Williams. In vivo fluorescence imaging of primate retinal ganglion cells and retinal pigment epithelial cells. *Opt. Express*, 14(16):7144–7158, 2006.

[113] J. I. W. Morgan, A. Dubra, R. Wolfe, W. H. Merigan, and D. R. Williams. In vivo autofluorescence imaging of the human and macaque retinal pigment epithelial cell mosaic. *Invest. Ophthalmol. Vis. Sci.*, 50(3):1350–1359, 2009.

[114] M. Paques, M. Simonutti, M. J. Roux, S. Picaud, E. Levavasseur, C. Bellman, and J.-A. Sahel. High resolution fundus imaging by confocal scanning laser ophthalmoscopy in the mouse. *Vision Res.*, 46:1336–1345, 2006.

[115] T. Higashide, I. Kawaguchi, S. Ohkubo, H. Tekeda, and K. Sugiyama. In vivo imaging and counting of rat retinal ganglion cells using a scanning laser ophthalmoscope. *Invest. Ophthalmol. Vis. Sci.*, 47(7):2943–2950, 2006.

[116] B. A. Sabel, R. Engelmann, and M. F. Humphrey. In vivo confocal neuroimaging (ICON) of CNS neurons. *Nat. Med.*, 3(2):244–247, 1997.

[117] M. F. Cordeiro, L. Guo, V. Luong, G. Harding, W. Wang, H. E. Jones ans S. E. Moss, A. M. Sillito, and F. W. Fitzke. Real-time imaging of single nerve cell apoptosis in retinal neurodegeneration. *Proc. Natl. Acad. Sci. U.S.A.*, 101(36):13352–13356, 2004.

[118] D. P. Biss, D. Sumorok, S. A. Burns, R. H. Webb, Y. Zhou, T. G. Bifano, D. Côté, I. Veilleux, P. Zamiri, and C. P. Lin. In vivo fluorescent imaging of the mouse retina using adaptive optics. *Opt. Lett.*, 32(6):659–661, 2007.

[119] D. C. Gray, R. Wolfe, B. P. Gee, D. Scoles, Y. Geng, B. D. Masella, A. Dubra, S. Luque, D. R. Williams, and W. H. Merigan. In vivo imaging of the fine structure of rhodamine-labeled macaque retinal ganglion cells. *Invest. Ophthalmol. Vis. Sci.*, 49(1):467–473, 2008.

[120] H.-U. Dodt. Infrarot-Ophthalmoskop, 1991. German patent # DE 4001893 A1.

[121] J. L. Calkins and C. D. Leonard. Holographic recording of a retina using a continuous wave laser. *Invest. Ophthalmol.*, 9(6):458–462, 1970.

[122] C. Hitzenberger and A. F. Fercher. Differential phase contrast in optical coherence tomography. *Opt. Lett.*, 24(9):622–624, 1999.

[123] K. A. Nugent, D. Paganin, and T. E. Gureyev. A phase odyssey. *Phys. Today*, 54(8):27–32, 2001.

[124] E. Hecht. *Optics*. Addison Wesley Publishing Company, Reading, USA, 2nd edition, 1987.

[125] J. W. Goodman. *Statistical Optics*. Wiley-Interscience, New-York, 2000.

[126] E. Goulielmakis, M. Uiberacker, R. Kienberger, A. Baltuska, V. Yakovlev, A. Scrinzi, Th. Westerwalbesloh, U. Kleineberg, U. Heinzmann, M. Drescher, and F. Krausz. Direct measurement of light waves. *Science*, 305:1267–1269, 2004.

[127] B. E. A. Saleh and M. C. Teich. *Fundamentals of Photonics*. Pure and Applied Optics. Wiley, New York, 1991.

[128] D. Malacara, editor. *Optical Shop Testing*. Wiley-Interscience, New Jersey, 3rd edition, 2007.

[129] M. R. Teague. Deterministic phase retrieval: A Green's function solution. *J. Opt. Soc. Am.*, 73(11):1434–1441, 1983.

[130] M. R. Teague. Image formation in terms of the transport equation. *J. Opt. Soc. Am. A*, 2(11):2019–2026, 1985.

[131] T. E. Gureyev, C. Raven, A. Snigirev, I. Snigireva, and S. W. Wilkins. Hard x-ray quantitative non-interferometric phase-contrast microscopy. *J. Phys. D: Appl. Phys.*, 32:563–567, 1999.

[132] F. Roddier. Wavefront sensing and the irradiance transport equation. *Appl. Opt.*, 29(10):1402–1403, 1990.

[133] F. Roddier. Curvature sensing and compensation: A new concept in adaptive optics. *Appl. Opt.*, 27(7):1223–1225, 1988.

[134] E. L. O'Neill and A. Walther. The question of phase in image formation. *Opt. Acta*, 10(1):33–40, 1963.

[135] A. Walther. The question of phase retrieval in optics. *Opt. Acta*, 10(1):41–49, 1963.

[136] J. C. Dainty and J. R. Fienup. Phase retrieval and image reconstruction for astronomy. In H. Stark, editor, *Image Recovery: Theory and Application*, chapter 7, pages 231–275. Academic Press, 1987.

[137] R. W. Gerchberg and W. O. Saxton. A practical algorithm for the determination of phase from image and diffraction plane pictures. *Optik*, 35(2):237–246, 1972.

[138] J. R. Fienup. Phase retrieval algorithms: a comparison. *Appl. Opt.*, 21(15):2758–2769, 1982.

[139] R. V. Shack and B. C. Platt. Production and use of a lenticular Hartmann screen. *J. Opt. Soc. Am.*, 61:656, 1971.

[140] J. Liang, B. Grimm, S. Goelz, and J. F. Bille. Objective measurement of wave aberrations of the human eye with the use of a Hartmann–Shack wave-front sensor. *J. Opt. Soc. Am. A*, 11(7):1949–1957, 1994.

[141] G. m. Dai. *Wavefront Optics for Vision Correction*. SPIE Press, Bellingham, Washington, 2008.

[142] S. Bará. Measuring eye aberrations with Hartmann–Shack wave-front sensors: Should the irradiance distribution across the eye pupil be taken into account? *J. Opt. Soc. Am. A*, 20(12):2237–2245, 2003.

[143] L. Diaz-Santana. *Wavefront Sensing in the Human Eye with a Shack–Hartmann Sensor*. PhD thesis, Imperial College of Science, Technology, and Medicine, University of London, London, UK, 2000.

[144] M. J. Kidger. *Fundamental Optical Design*. SPIE Press, Bellingham, Washington, USA, 2002.

[145] R. N. Bracewell. *The Fourier Transform and its Applications*. Electrical and Electronic Engineering. McGraw-Hill, New York, 1st edition, 1965.

[146] O. Scherzer. The theoretical resolution limit of the electron microscope. *J. Appl. Phys.*, 20(1):20–29, 1949.

[147] L. Foucault. Description des procédés employés pour reconnaître la configuration des surfaces optiques. *C. r. hebd. séances Acad. sci.*, T.47:958–959, 1858.

[148] L. Foucault. Mémoire sur la construction des télescopes en verre argenté. In U.-J. Le Verrier, editor, *Annales de l'Observatoire Impérial de Paris*, volume 5, pages 197–237. Mallet-Bachelier, Paris, 1859.

[149] G. S. Settles. *Schlieren and Shadowgraph Techniques: Visualizing Phenomena in Transparent Media*. Experimental Fluid Mechanics. Springer-Verlag, Berlin, 2001.

[150] S. Lowenthal and Y. Belvaux. Observation of phase objects by optically processed Hilbert transform. *Appl. Phys. Lett.*, 11(2):49–51, 1967.

[151] R. Ragazzoni. Pupil plane wavefront sensing with an oscillating prism. *J. Mod. Optics*, 43(2):289–293, 1996.

[152] I. Iglesias, R. Ragazzoni, Y. Julien, and P. Artal. Extended source pyramid wave-front sensor for the human eye. *Opt. Express*, 10(9):419–428, 2002.

[153] S. R. Chamot, C. Dainty, and S. Esposito. Adaptive optics for ophthalmic applications using a pyramid wavefront sensor. *Opt. Express*, 14(2):518–526, 2006.

[154] J. J. Lister. On some properties in achromatic object-glasses applicable to the improvement of the microscope. *Phil. T. Roy. Soc.*, 120:187–200, 1830.

[155] E. L. O'Neill. Spatial filtering in optics. *IRE Trans. Inform. Theory*, IT-2:56–65, 1956.

[156] F. Zernike. Diffraction theory of the knife-edge test and its improved form, the phase-contrast method. *Mon. Not. R. Astron. Soc.*, 94(5):377–384, 1934.

[157] C. S. Yelleswarapu, S.-R. Kothapalli, F. J. Aranda, D. V. G. L. N. Rao, Y. R. Vaillancourt, and B. R. Kimball. Phase contrast imaging using photothermally induced phase transitions in liquid crystals. *Appl. Phys. Lett.*, 89:211116, 2006.

[158] C. Maurer, A. Jesacher, S. Bernet, and M. Ritsch-Marte. Phase contrast microscopy with full numerical aperture illumination. *Opt. Express*, 16(24):19821–19829, 2008.

[159] V. Ronchi. Forty years of history of a grating interferometer. *Appl. Opt.*, 3(4):437–451, 1964.

[160] R. Hoffman and L. Gross. The modulation contrast microscope. *Nature*, 254(5501):586–588, 1975.

[161] R. Hoffman and L. Gross. Modulation contrast microscope. *Appl. Opt.*, 14(5):1169–1176, 1975.

[162] S. Fürhapter, A. Jesacher, S. Bernet, and M. Ritsch-Marte. Spiral phase contrast imaging in microscopy. *Opt. Express*, 13(3):689–694, 2005.

[163] M. G. Nomarski. Microinterféromètre différentiel à ondes polarisées. *J. Phys. Radium*, 16(3):9S–13S, 1955.

[164] D. Gabor. A new microscopic principle. *Nature*, 161(4098):777–778, 1948.

[165] E. Cuche, F. Bevilacqua, and C. Depeursinge. Digital holography for quantitative phase-contrast imaging. *Opt. Lett.*, 24(5):291–293, 1999.

[166] F. Zernike. How I discovered phase contrast. *Science*, 121:345–349, 1955.

[167] F. Zernike. Diffraction theory of the knife-edge test and its improved form, the phase-contrast method. *J. Microlith. Microfab. Microsyst.*, 1(2):87–94, 2002. Translated from Physica I, 689–704, 1934, by A. Yen.

[168] F. Zernike. Phase contrast, a new method for the microscopic observation of transparent objects, part I. *Physica*, 9(7):686–698, 1942.

[169] F. Zernike. Phase contrast, a new method for the microscopic observation of transparent objects, part II. *Physica*, 9(10):974–986, 1942.

[170] B. Lyot. Procédés permettant d'étudier les irrégularités d'une surface optique bien polie. *C. R. Acad. Sci. (Paris)*, 222(14):765–768, 1946.

[171] E. H. Armstrong. A method of reducing disturbances in radio signaling by a system of frequency modulation. *Proc. IRE*, 24(5):689–740, 1936.

[172] P. C. Mogensen and J. Glückstad. Reverse phase contrast: An experiment demonstration. *Appl. Opt.*, 41(11):2103–2110, 2002.

[173] T. Noda and S. Kawata. Separation of phase and absorption images in phase-contrast microscopy. *J. Opt. Soc. Am. A*, 9(6):924–931, 1992.

[174] M. Françon. *Le Contraste de Phase en Optique et en Microscopie*. Éditions de la Revue d'Optique Théorique et Instrumentale, Paris, 1950.

[175] H. Osterberg. The polanret microscope. *J. Opt. Soc. Am.*, 37(9):726–730, 1947.

[176] E. H. Linfoot. On the Zernike phase-contrast test. *Proc. Phys. Soc.*, 58(6):759–768, 1946.

[177] C. S. Anderson. Fringe visibility, irradiance, and accuracy in common path interferometers for visualization of phase disturbances. *Appl. Opt.*, 34(32):7474–7485, 1995.

[178] J. Glückstad and P. C. Mogensen. Optimal phase contrast in common-path interferometry. *Appl. Opt.*, 40(2):268–282, 2001.

[179] W. J. Geeraets and E. R. Berry. Ocular spectral characteristics as related to hazards from lasers and other light sources. *Am. J. Ophthalmol.*, 66(1):15–20, 1968.

[180] E. A. Boettner and J. R. Wolter. Transmission of the ocular media. *Invest. Ophthalmol.*, 1(6):776–783, 1962.

[181] BSi British Standards. *Safety of Laser Products—Equipment Classification, Requirements and User's Guide.* BS EN 60825-1:1994 with Amendment 1–3 and Corrigendum 1. BSi British Standards, 1994.

[182] American National Standard Institute. *American National Standard for Safe Use of Lasers.* Z136.1-2000. Laser Institute of America, Orlando, USA, 2000.

[183] International Commission on Non-Ionizing Radiation Protection. Guidelines on limits of exposure to laser radiation of wavelengths between 180 nm and 1000 μm. *Health Phys.*, 71(5):804–819, 1996.

[184] S. Martinez-Conde, S. L. Macknik, and D. H. Hubel. The role of fixational eye movements in visual perception. *Nature Neurosci.*, 5:229–240, 2004.

[185] L. F. Schmetterer, F. Lexer, C. J. Unfried, H. Sattmann, and A. F. Fercher. Topical measurement of fundus pulsations. *Opt. Eng.*, 34(3):711–716, 1995.

[186] D. R. Iskander and H. T. Kasprzak. Dynamics in longitudinal eye movements and corneal shape. *Ophthal. Physiol. Opt.*, 26(6):572–579, 2006.

[187] M. Pircher, B. Baumann, E. Götzinger, H. Sattmann, and C. K. Hitzenberger. Simultaneous SLO/OCT imaging of the human retina with axial eye motion correction. *Opt. Express*, 15(25):16922–16932, 2007.

[188] W. N. Charman and G. Heron. Fluctuations in accommodation: A review. *Ophthal. Physiol. Opt.*, 8(2):153–164, 1988.

[189] R. Tutt, A. Bradley, C. Begley, and L. N. Thibos. Optical and visual impact of tear break-up in human eyes. *Invest. Ophthalmol. Vis. Sci.*, 41(13):4117–4123, 2000.

[190] E. Goto, Y. Yagi, Y. Matsumoto, and K. Tsubota. Impaired functional visual acuity of dry eye patients. *Am. J. Ophthalmol.*, 133(2):181–186, 2002.

[191] A. Dubra, C. Paterson, and C. Dainty. Study of the tear topography dynamics using a lateral shearing interferometer. *Opt. Express*, 12(25):6278–6288, 2004.

[192] S. Gruppetta, F. Lacombe, and P. Puget. Study of the dynamic aberrations of the human tear film. *Opt. Express*, 13(19):7631–7636, 2005.

[193] R. M. Steinman, R. J. Cunitz, G. T. Timberlake, and M. Herman. Voluntary control of microsaccades during maintained monocular fixation. *Science*, 155:1577–1579, 1967.

[194] L. A. Riggs, J. C. Armington, and F. Ratliff. Motions of the retinal image during fixation. *J. Opt. Soc. Am.*, 44(4):315–321, 1954.

[195] L. A. Riggs, F. Ratliff, J. C. Cornsweet, and T. N. Cornsweet. The disappearance of steadily fixated visual test objects. *J. Opt. Soc. Am.*, 43(6):495–501, 1953.

[196] J. J. Koenderink and A. J. van Doorn. Method of stabilizing the retinal image. *Appl. Opt.*, 13(4):955–961, 1974.

[197] D. X. Hammer, D. Ferguson, J. C. Magill, M. A. White, A. E. Elsner, and R. H. Webb. Image stabilization for scanning laser ophthalmoscopy. *Opt. Express*, 10(26):1542–1549, 2002.

[198] F. C. Delori and K. P. Pflibsen. Spectral reflectance of the human ocular fundus. *Appl. Opt.*, 28(6):1061–1077, 1989.

[199] N. P. A. Zagers, J. van de Kraats, T. T. J. M. Berendschot, and D. van Norren. Simultaneous measurement of foveal spectral reflectance and cone-photoreceptor directionality. *Appl. Opt.*, 41(22):4686–4696, 2002.

[200] J. van de Kraats, T. T. J. M. Berendschot, and D. van Norren. The pathways of light measured in fundus reflectometry. *Vision Res.*, 36(15):2229–2247, 1996.

[201] J. van de Kraats and D. van Norren. Directional and nondirectional spectral reflection from the human fovea. *J. Biomed. Opt.*, 13(2):024010, 2008.

[202] T. T. J. M. Berendschot, P. J. DeLint, and D. van Norren. Fundus reflectance—historical and present ideas. *Prog. Retin. Eye Res.*, 22(2):171–200, 2003.

[203] S. Y. Schmidt and R. D. Peisch. Melanin concentration in normal human retinal pigment epithelium. Regional variation and age-related reduction. *Invest. Ophthalmol. Vis. Sci.*, 27(7):1063–1067, 1986.

[204] R. W. Knighton. Quantitative reflectometry of the ocular fundus. *IEEE Eng. Med. Biol.*, 14(1):43–51, 1995.

[205] J.-M. Gorrand and F. C. Delori. A reflectometric technique for assessing photoreceptor alignment. *Vision Res.*, 35(7):999–1010, 1995.

[206] S. A. Burns, S. Wu, J. C. He, and A. E. Elsner. Variations in photoreceptor directionality across the central retina. *J. Opt. Soc. Am. A*, 14(9):2033–2040, 1997.

[207] S. S. Choi, N. Doble, J. Lin, J. Christou, and D. R. Williams. Effect of wavelength on in vivo images of the human cone mosaic. *J. Opt. Soc. Am. A*, 22(12):2598–2605, 2005.

[208] P. M. Prieto, J. S. McLellan, and S. A. Burns. Investigating the light absorption in a single pass through the photoreceptor layer by means of the lipofuscin fluorescence. *Vision Res.*, 45:1957–1965, 2005.

[209] W. Gao, B. Cense, Y. Zhang, R. S. Jonnal, and D. T. Miller. Measuring retinal contributions to the optical Stiles–Crawford effect with optical coherence tomography. *Opt. Express*, 16(9):6486–6501, 2008.

[210] J. Beuthan, O. Minet, J. Helfmann, M. Herrig, and G. Müller. The spatial variation of the refractive index in biological cells. *Phys. Med. Biol.*, 41:369–382, 1996.

[211] C. G. Rylander, D. P. Davé, T. Akkin, T. E. Milner, K. R. Diller, and A. J. Welch. Quantitative phase-contrast imaging of cells with phase-sensitive optical low coherence microscopy. *Opt. Lett.*, 29(13):1509–1511, 2004.

[212] A. Brunsting and P. F. Mullaney. Differential light scattering from spherical mammalian cells. *Biophys. J.*, 14(6):439–453, 1974.

[213] W. Choi, C. Fang-Yen, K. Badizadegan, S. Oh, N. Lue, R. R. Dasari, and M. S. Feld. Tomographic phase microscopy. *Nat. Methods*, 4(9):717–719, 2007.

[214] T. Wilson and C. Sheppard. *Theory and Practice of Scanning Optical Microscope*. Academic Press, London, 1984.

[215] A. W. Kulawiec and D. T. Moore. Quantitative phase imaging in confocal microscopy by optical differentiation. *Appl. Opt.*, 33(28):6582–6590, 1994.

[216] C. J. Cogswell and C. J. R. Sheppard. Confocal differential interference contrast (DIC) microscopy: Including a theoretical analysis of conventional and confocal DIC imaging. *J. Microsc. Oxford*, 165(1):81–101, 1990.

[217] S. A. Burns, R. Tumbar, A. E. Elsner, D. Ferguson, and D. X. Hammer. Large-field-of-view, modular, stabilized, adaptive-optics-based scanning laser ophthalmoscope. *J. Opt. Soc. Am. A*, 24(5):1313–1326, 2007.

[218] X. J. Wang, T. E. Milner, and J. S. Nelson. Characterization of fluid flow velocity by optical Doppler tomography. *Opt. Lett.*, 20(11):1337–1339, 1995.

[219] S. Yazdanfar, A. M. Rollins, and J. A. Izatt. Imaging and velocimetry of the human retinal circulation with color Doppler optical coherence tomography. *Opt. Lett.*, 25(19):1448–1450, 2000.

[220] Y. Zhao, Z. Chen, C. Saxer, S. Xiang, J. F. de Boer, and J. S. Nelson. Phase-resolved optical coherence tomography and optical Doppler tomography for imaging blood flow in human skin with fast scanning speed and high velocity sensitivity. *Opt. Lett.*, 25(2):114–116, 2000.

[221] R. A. Leitgeb, L. Schmetterer, W. Drexler, A. F. Fercher, R. J. Zawadzki, and T. Bajraszewski. Real-time assessment of retinal blood flow with ultrafast acquisition by color Doppler Fourier domain optical coherence tomography. *Opt. Express*, 11(23):3116–3121, 2003.

[222] R. A. Leitgeb, L. Schmetterer, C. K. Hitzenberger, A. F. Fercher, F. Berisha, M. Wojtkowski, and T. Bajraszewski. Real-time measurement of in vitro flow by Fourier-domain color Doppler optical coherence tomography. *Opt. Lett.*, 29(2):171–173, 2004.

[223] B. R. White, M. C. Pierce, N. Nassif, B. Cense, B. Hyle Park, G. J. Tearney, B. E. Bouma, T. C. Chen, and J. F. de Boer. In vivo dynamic human retinal blood flow imaging using ultra-high-speed spectral domain optical Doppler tomography. *Opt. Express*, 11(25):3490–3497, 2003.

[224] B. H. Park, M. C. Pierce, B. Cense, S.-H. Yun, M. Mujat, G. J. Tearney, B. E. Bouma, and J. F. de Boer. Real-time fiber-based multi-functional spectral-domain optical coherence tomography at 1.3 μm. *Opt. Express*, 13(11):3931–3944, 2005.

[225] M. Sticker, C. K. Hitzenberger, R. Leitgeb, and A. F. Fercher. Quantitative differential phase measurement and imaging in transparent and turbid media by optical coherence tomography. *Opt. Lett.*, 26(8):518–520, 2001.

[226] A. F. Fercher, W. Drexler, C. K. Hitzenberger, and T. Lasser. Optical coherence tomography—principles and applications. *Rep. Prog. Phys.*, 66:239–303, 2003.

[227] H. H. Hopkins. A note on the theory of phase-contrast images. *P. Phys. Soc. Lond. B*, 66(400):331–333, 1953.

[228] W. J. Smith. *Modern Optical Engineering*. McGraw-Hill, New York, 3rd edition, 2000.

[229] T. J. T. P. van den Berg. Analysis of intraocular straylight, especially in relation to age. *Optom. Vis. Sci.*, 72(2):52–59, 1995.

[230] E. Logean, E. Dalimier, and C. Dainty. Measured double-pass intensity point-spread function after adaptive optics correction of ocular aberrations. *Opt. Express*, 16(22):17348–17357, 2008.

[231] E. Dalimier, K. M. Hampson, and J. C. Dainty. Effects of adaptive optics on visual performance. In F. D. Murtagh, editor, *Proc. SPIE: Opto-Ireland 2005: Imaging and Vision*, volume 5823, pages 20–28, 2005.

[232] E. Dalimier. *Adaptive Optics Correction of Ocular Higher-Order Aberrations and the Effects on Functional Vision*. PhD thesis, National University of Ireland, Galway, Ireland, 2007.

[233] E. Dalimier and C. Dainty. Comparative analysis of deformable mirrors for ocular adaptive optics. *Opt. Express*, 13(11):4275–4285, 2005.

[234] F. Flamant. Étude de la répartition de lumière dans l'image rétinienne d'une fente. *Rev. Opt. Theor. Instrum.*, 34(9):433–459, 1955.

[235] J. Krauskopf. Light distribution in human retinal images. *J. Opt. Soc. Am.*, 52(9):1046–1050, 1962.

[236] G. Westheimer and F. W. Campbell. Light distribution in the image formed by the living human eye. *J. Opt. Soc. Am.*, 52(9):1040–1045, 1962.

[237] F. W. Campbell and R. W. Gubisch. Optical quality of the human eye. *J. Physiol. (Lond.)*, 186(3):558–578, 1966.

[238] J. Santamaría, P. Artal, and J. Bescós. Determination of the point-spread function of human eyes using a hybrid optical-digital method. *J. Opt. Soc. Am. A*, 4(6):1109–1114, 1987.

[239] J. Liang and G. Westheimer. Optical performances of human eyes derived from double-pass measurements. *J. Opt. Soc. Am. A*, 12(7):1411–1416, 1995.

[240] J. Liang and D. R. Williams. Aberrations and retinal image quality of the normal human eye. *J. Opt. Soc. Am. A*, 14(11):2873–2883, 1997.

[241] D. R. Williams, D. H. Brainard, M. J. McMahon, and R. Navarro. Double-pass and interferometric measures of the optical quality of the eye. *J. Opt. Soc. Am. A*, 11(12):3123–3135, 1994.

[242] P. Rodríguez and R. Navarro. Double-pass versus aberrometric modulation transfer function in green light. *J. Biomed. Opt.*, 12(4):044018, 2007.

[243] P. Artal, S. Marcos, R. Navarro, and D. R. Williams. Odd aberrations and double-pass measurements of retinal image quality. *J. Opt. Soc. Am. A*, 12(2):195–201, 1995.

[244] L. Diaz-Santana and J. C. Dainty. Effects of retinal scattering in the ocular double-pass process. *J. Opt. Soc. Am. A*, 18(7):1437–1444, 2001.

[245] Y. Le Grand. Sur la mesure de l'acuité visuelle au moyen de franges d'interférence. *C. R. Acad. Sci. (Paris)*, 200:490–491, 1935.

[246] W. N. Charman and P. Simonet. Yves Le Grand and the assessment of retinal acuity using interference fringes. *Ophthal. Physiol. Opt.*, 17(2):164–168, 1997.

[247] J. M. Gorrand, O. Dupuy, F. Farfal, M. T. Plantegenest, and S. Slansky. Contributions de la rétine et du système optique de l'œil à l'abaissement de la modulation de l'image par double traversée de l'œil. *J. Optics (Paris)*, 9(6):359–364, 1978.

[248] J. M. Gorrand. Diffusion of the human retina and quality of the optics of the eye on the fovea and the peripheral retina. *Vision Res.*, 19(8):907–912, 1979.

[249] J.-M. Gorrand, R. Alfieri, and J.-Y. Boire. Diffusion of the retinal layers of the living human eye. *Vision Res.*, 24(9):1097–1106, 1984.

[250] P. Artal and R. Navarro. Simultaneous measurement of two-point-spread functions at different locations across the human fovea. *Appl. Opt.*, 31(19):3646–3656, 1992.

[251] F. Vargas-Martín, P. M. Prieto, and P. Artal. Correction of the aberrations in the human eye with a liquid-crystal spatial light modulator: Limits to performance. *J. Opt. Soc. Am. A*, 15(9):2552–2562, 1998.

[252] J. M. Bueno. Depolarization effects in the human eye. *Vision Res.*, 41:2687–2696, 2001.

[253] D. S. Greenfield, R. W. Knighton, and X.-R. Huang. Effect of corneal polarization axis on assessment of retinal nerve fiber layer thickness by scanning laser polarimetry. *Am. J. Ophthalmol.*, 129(6):715–722, 2000.

[254] E. Logean, E. Dalimier, and C. Dainty. Double pass intensity images of a point source after adaptive optics correction of ocular aberrations. In *Invest. Ophthalmol. Vis. Sci.*, pages ARVO E–Abstract 4196, 2008, 49.

[255] I. N. Bronshtein, K. A. Semendyayev, G. Musiol, and H. Muehlig. *Handbook of Mathematics*. Springer, Berlin, 4$^{\text{th}}$ edition, 2004.

[256] J. J. Vos and T. J. T. P. van den Berg. Report on disability glare. *CIE Collection*, 135(1):1–9, 1999.

[257] J. J. Vos, J. Walraven, and A. van Meeteren. Light profiles of the foveal image of a point source. *Vision Res.*, 16(2):215–219, 1976.

[258] J. M. Schmitt, A. H. Gandjbakhche, and R. F. Bonner. Use of polarized light to discriminate short-path photons in a multiply scattering medium. *Appl. Opt.*, 31(30):6535–6546, 1992.

[259] H. Horinaka, K. Hashimoto, K. Wada, Y. Cho, and M. Osawa. Extraction of quasi-straightforward-propagating photons from diffused light transmitting through a scattering medium by polarization modulation. *Opt. Lett.*, 20(13):1501–1503, 1995.

[260] F. C. MacKintosh, J. X. Zhu, D. J. Pine, and D. A. Weitz. Polarization memory of multiply scattered light. *Phys. Rev. B*, 40(13):9342–9345, 1989.

[261] D. Bicout, C. Brosseau, A. S. Martinez, and J. M. Schmitt. Depolarization of multiply scattered waves by spherical diffusers: Influence of the size parameter. *Phys. Rev. E*, 49(2):1767–1770, 1994.

[262] J. P. Woodcock. Physical properties of blood and their influence on blood-flow measurement. *Rep. Prog. Phys.*, 39:65–127, 1976.

[263] M. Feierabend, M. Rückel, and W. Denk. Coherence-gated wave-front sensing in strongly scattering samples. *Opt. Lett.*, 29(19):2255–2257, 2004.

[264] M. Rueckel, J. A. Mack-Bucher, and W. Denk. Adaptive wavefront correction in two-photon microscopy using coherence-gated wavefront sensing. *Proc. Natl. Acad. Sci. U.S.A.*, 103(46):17137–17142, 2006.

[265] K. Jeong, J. J. Turek, and D. D. Nolte. Phase-contrast optical coherence imaging of tissue. In V. V. Tuchin, J. A. Izatt, and J. G. Fujimoto, editors, *Proc. SPIE: Coherence Domain Optical Methods and Optical Coherence Tomography in Biomedicine IX*, volume 5690, pages 412–421, 2005.

[266] R. H. Dicke. Phase-contrast detection of telescope seeing errors and their correction. *Astrophys. J.*, 198(3):605–615, 1975.

[267] E. E. Bloemhof and J. K. Wallace. Simple broadband implementation of a phase contrast wavefront sensor for adaptive optics. *Opt. Express*, 12(25):6240–6245, 2004.

[268] M. A. Vorontsov, E. W. Justh, and L. A. Beresnev. Adaptive optics with advanced phase-contrast techniques. I. high-resolution wave-front sensing. *J. Opt. Soc. Am. A*, 18(6):1289–1299, 2001.

[269] T. Huang, W. Lu, S. Zhang, and A. H. Greenaway. Zernike phase sensor for phasing of segmented telescopes. *Appl. Phys. B*, 86:139–145, 2007.

[270] K. Dohlen, M. Langlois, P. Lanzoni, S. Mazzanti, A. Vigan, L. Montoya, E. Hernandez, M. Reyes, I. Surdej, and N. Yaitskova. ZEUS, a cophasing sensor based on the Zernike phase contrast method. In L. M. Stepp, editor, *Proc. SPIE: Ground-Based and Airborne Telescopes*, volume 6267, page 626734, 2006.

[271] C. Paterson. A fundamental limit for wavefront sensing. In C. Dainty, editor, *Adaptive Optics for Industry and Medicine*, Proceedings of the Sixth International Workshop, pages 157–162, National University of Ireland, Galway, 2007. Imperial College Press.

[272] J. J. Rozema, D. van Dyck, and F. J. Van de Velde. Phase contrast aberroscope, 1999. United States Patent #6002484.

[273] K. Y. Li and G. Yoon. Changes in aberrations and retinal image quality due to tear film dynamics. *Opt. Express*, 14(25):12552–12559, 2006.

[274] F. Delori, R. H. Webb, and D. Sliney. Maximum permissible exposures for ocular safety (ANSI 2000), with emphasis on ophthalmic devices. *J. Opt. Soc. Am. A*, 24(5):1250–1265, 2007.

[275] M. Böhnke and B. R. Masters. Confocal microscopy of the cornea. *Prog. Retin. Eye Res.*, 18(5):553–628, 1999.

[276] F. Zernike. Beugungstheorie des Schneidenverfahrens und seiner verbesserten Version der Phasenkontrastmethode. *Physica*, 1:689–704, 1934.

[277] B. R. A. Nijboer. *The Diffraction Theory of Aberrations*. PhD thesis, University of Groningen, Batavia, 1942.

[278] N. W. McLachlan. *Bessel Functions for Engineers*. Engineering Science Series. Oxford University Press, London, 1955.

[279] R. J. Noll. Zernike polynomials and atmospheric turbulence. *J. Opt. Soc. Am.*, 66(3):207–211, 1976.

[280] L. N. Thibos, R. A. Applegate, J. T. Schweigerling, R. Webb, and VSIA Standards Taskforce Members. Standards for reporting the optical aberrations of eyes. In V. Lackshminarayanan, editor, *Vision Science and Its Applications*, volume 35 of *Trends in Optics and Photonics (TOPS)*, pages 232–244. Optical Society of America, 2000.

[281] J. I. W. Morgan, J. J. Hunter, B. Masella, R. Wolfe, D. G. Gray, W. H. Merigan, F. C. Delori, and D. R. Williams. Light-induced retinal changes observed with high-resolution autofluorescence imaging of the retinal pigment epithelium. *Invest. Ophthalmol. Vis. Sci.*, 49(8):3715–3729, 2008.

[282] International Commission on Non-Ionizing Radiation Protection. Revision of guidelines on limits of exposure to laser radiation of wavelengths between 400 nm and 1.4 μm. *Health Phys.*, 79(4):431–440, 2000.

[283] D. J. Lund, P. Edsall, B. E. Stuck, and K. Schulmeister. Variation of laser-induced retinal injury thresholds with retinal irradiated area: 0.1-s duration, 514-nm exposures. *J. Biomed. Opt.*, 12(2):024023, 2007.

[284] D. H. Sliney and B. C. Freasier. Evaluation of optical radiation hazards. *Appl. Opt.*, 12(1):1–24, 1973.

[285] J. W. Ness, H. Zwick, B. E. Stuck, D. J. Lund, B. J. Lund, J. W. Molchany, and D. H. Sliney. Retinal image motion during deliberate fixation: Implications to laser safety for long duration viewing. *Health Phys.*, 78(2):131–142, 2000.

[286] B. J. Lund, D. J. Lund, and P. R. Esdall. Laser-induced retinal damage threshold measurements with wavefront correction. *J. Biomed. Opt.*, 13(6):064011, 2008.